The interplay of roughness and adhesion in viscoelastic sliding contacts

The doctoral scholarship was funded by the European Union - Next Generation EU, Mission 4 Component 2 CUP D93D22001330001

Department of Mechanics, Mathematics and Management

Mechanical and Management Engineering
Ph.D. Program

SSD: ING-IND/13 - Applied Mechanics

Final dissertation

The interplay of roughness and adhesion in viscoelastic sliding contacts

Michele Mastropasqua

Supervisors:

Prof. Giuseppe Carbone

Prof. Nicola Menga

Industrial Co-supervisor:

PhD. Andrea Ronchi

(Pirelli Tyre S.p.A.)

Coordinator of the PhD Program:
Prof. Giuseppe Casalino

Course XXXVIII, 01/11/2022 - 01/11/2025

The doctoral scholarship was funded by the European Union - Next Generation EU, Mission 4 Component 2 CUP D93D22001330001

Department of Mechanics, Mathematics and Management

Mechanical and Management Engineering
Ph.D. Program

SSD: ING-IND/13 - Applied Mechanics

Final dissertation

The interplay of roughness and adhesion in viscoelastic sliding contacts

Michele Mastropasqua

Referees:

Prof. Alessandro Ruggiero

Prof. Flavio Farroni

Supervisors:

Prof. Giuseppe Carbone

Prof. Nicola Menga

Industrial Co-supervisor:

PhD. Andrea Ronchi

Coordinator of the PhD Program:
Prof. Giuseppe Casalino

Course XXXVIII, 01/11/2022 - 01/11/2025

Politecnico di Bari

LIBERATORIA PER L'ARCHIVIAZIONE DELLA TESI DI DOTTORATO

Al Magnifico Rettore
del Politecnico di Bari

Il/la sottoscritto Michele Mastropasqua nato a Tortona (AL) il 26/03/1998

residente a Molfetta (BA) in via Pietro Colletta N. 106 e-mail m.mastropasqua3@phd.poliba.it

iscritto al 3° anno di Corso di Dottorato di Ricerca in Ingegneria Meccanica e Gestionale ciclo XXXVIII

ed essendo stato ammesso a sostenere l'esame finale con la prevista discussione della tesi dal titolo:

"The interplay of roughness and adhesion in viscoelastic sliding contacts"

DICHIARA

1) di essere consapevole che, ai sensi del D.P.R. n. 445 del 28.12.2000, le dichiarazioni mendaci, la falsità negli atti e l'uso di atti falsi sono puniti ai sensi del codice penale e delle Leggi speciali in materia, e che nel caso ricorressero dette ipotesi, decade fin dall'inizio e senza necessità di nessuna formalità dai benefici conseguenti al provvedimento emanato sulla base di tali dichiarazioni;
2) di essere iscritto al Corso di Dottorato di ricerca in Ingegneria Meccanica e Gestionale ciclo XXXVIII, corso attivato ai sensi del "*Regolamento dei Corsi di Dottorato di ricerca del Politecnico di Bari"*, emanato con D.R. n.286 del 01.07.2013;
3) di essere pienamente a conoscenza delle disposizioni contenute nel predetto Regolamento in merito alla procedura di deposito, pubblicazione e autoarchiviazione della tesi di dottorato nell'Archivio Istituzionale ad accesso aperto alla letteratura scientifica;
4) di essere consapevole che attraverso l'autoarchiviazione delle tesi nell'Archivio Istituzionale ad accesso aperto alla letteratura scientifica del Politecnico di Bari (IRIS-POLIBA), l'Ateneo archivierà e renderà consultabile in rete (nel rispetto della Policy di Ateneo di cui al D.R. 642 del 13.11.2015) il testo completo della tesi di dottorato, fatta salva la possibilità di sottoscrizione di apposite licenze per le relative condizioni di utilizzo (di cui al sito http://www.creativecommons.it/Licenze), e fatte salve, altresì, le eventuali esigenze di "embargo", legate a strette considerazioni sulla tutelabilità e sfruttamento industriale/commerciale dei contenuti della tesi, da rappresentarsi mediante compilazione e sottoscrizione del modulo in calce (Richiesta di embargo);
5) che la tesi da depositare in IRIS-POLIBA, in formato digitale (PDF/A) sarà del tutto identica a quelle **consegnate**/inviate/da inviarsi ai componenti della commissione per l'esame finale e a qualsiasi altra copia depositata presso gli Uffici del Politecnico di Bari in forma cartacea o digitale, ovvero a quella da discutere in sede di esame finale, a quella da depositare, a cura dell'Ateneo, presso le Biblioteche Nazionali Centrali di Roma e Firenze e presso tutti gli Uffici competenti per legge al momento del deposito stesso, e che di conseguenza va esclusa qualsiasi responsabilità del Politecnico di Bari per quanto riguarda eventuali errori, imprecisioni o omissioni nei contenuti della tesi;
6) che il contenuto e l'organizzazione della tesi è opera originale realizzata dal sottoscritto e non compromette in alcun modo i diritti di terzi, ivi compresi quelli relativi alla sicurezza dei dati personali; che pertanto il Politecnico di Bari ed i suoi funzionari sono in ogni caso esenti da responsabilità di qualsivoglia natura: civile, amministrativa e penale e saranno dal sottoscritto tenuti indenni da qualsiasi richiesta o rivendicazione da parte di terzi;
7) che il contenuto della tesi non infrange in alcun modo il diritto d'Autore né gli obblighi connessi alla salvaguardia di diritti morali od economici di altri autori o di altri aventi diritto, sia per testi, immagini, foto, tabelle, o altre parti di cui la tesi è composta.

Luogo e data, Bari, 15/12/2025 Firma Michele Mastropasqua

Il/La sottoscritto, con l'autoarchiviazione della propria tesi di dottorato nell'Archivio Istituzionale ad accesso aperto del Politecnico di Bari (POLIBA-IRIS), pur mantenendo su di essa tutti i diritti d'autore, morali ed economici, ai sensi della normativa vigente (Legge 633/1941 e ss.mm.ii.),

CONCEDE

- al Politecnico di Bari il permesso di trasferire l'opera su qualsiasi supporto e di convertirla in qualsiasi formato al fine di una corretta conservazione nel tempo. Il Politecnico di Bari garantisce che non verrà effettuata alcuna modifica al contenuto e alla struttura dell'opera.
- al Politecnico di Bari la possibilità di riprodurre l'opera in più di una copia per fini di sicurezza, back-up e conservazione.

Luogo e data, Bari, 15/12/2025 Firma Michele Mastropasqua

Abstract

Ensuring effective control of adhesion in viscoelastic materials represent a crucial challenge in modern tribology, with significant implications across a broad spectrum of engineering applications, including tire tread compounds for enhanced grip and efficiency, soft robotic grippers with reversible adhesion, structural and pressure-sensitive adhesives, bio-inspired adhesive systems and MEMS devices. Despite experimental results have highlighted how the interaction between interface adhesion and viscoelasticity affects the contact behavior of real interfaces, current analytical and numerical approaches can accurately describe only adhesiveless conditions in presence of relative motion between solids or require ad hoc local interatomic potentials to mimic adhesive effects. Observations of phenomena such as hysteretic losses, adhesion hysteresis and velocity-dependent adhesive strength further underline the limitations of these existing models, which often rely on scale separation or assume purely elastic behavior. Building upon a previously developed extension of Griffith's fracture criterion to hysteretic materials, this thesis further extends the framework to the rough multi-contact case and employs it to investigate the contact and friction behaviour of several multiscale rough profiles in the presence of interface adhesion, across the entire viscoelastic spectrum of the material. Exploiting the boundary element methodology based on the use of the Green's function, the energy closure equations were obtained by imposing, at each contact edge, a balance between the work of internal stresses and that of adhesion under virtual infinitesimal variations of the contact domain. Moving from the assumption of infinitely short-range adhesive forces, the proposed approach extends classical fracture concepts to account for non-conservative energy dissipation arising from viscoelastic stresses. The mathematical and physical structure of this energy formulation significantly departs from equivalent elastic cases, allowing for a consistent treatment of both bulk and interfacial hysteresis effects. The results shows a marked increase in contact area, adhesive strength and friction, particularly at intermediate sliding velocities, driven by the coexistence of adhesion hysteresis induced by small-scale viscoelasticity at the edge of the contacts and bulk hysteresis generated by large-scale viscoelasticity, supporting the findings of previous similar studies for a sinusoidal indenter. By addressing the fundamental interplay between viscoelasticity, roughness and adhesion, this work establishes a unified theoretical foundation that explains key experimental observations and supports the rational design of viscoelastic materials with tailored adhesive and tribological properties.

Contents

List of Figures

Introduction

The use of polymeric materials has gained increasing prominence in recent years, owing to their relevance in a wide range of technological and industrial applications. This widespread adoption is motivated not only by their outstanding mechanical, chemical and functional properties, but also by the possibility of tailoring their behavior through molecular design and surface microstructuring. In this context, understanding the mechanisms of adhesion in polymeric materials represents one of the core challenges of contemporary tribology and contact mechanics, with important implications in numerous application fields. Adhesion in polymer systems arises from a complex interaction among intermolecular forces at the interface, surface morphology and roughness, and the intrinsic viscoelastic response of the material, which imparts a pronounced time- and frequency-dependent mechanical behavior. This interplay of phenomena is crucial, for example, in the design of tire tread compounds, where adhesion critically affects grip, energy efficiency and safety, as discussed in several recent studies [1–3]. Similarly, the ability to control and modulate adhesion in polymeric materials is fundamental for the development of advanced automotive components [4] and soft robotic systems featuring reversible adhesion [5–7]. Significant progress has also been made in the study and development of biological and bio-inspired adhesives, which take inspiration from natural systems such as those of mussels and geckos, with the aim of reproducing a robust yet reversible and controllable adhesion [8–14]. Adhesive phenomena also play an important role in micro- and nano-electromechanical devices (MEMS/NEMS), in which, due to their small size, surface forces become dominant and can lead to undesirable effects, such as stiction, requiring a thorough understanding of adhesion mechanisms for proper system design and control [15–20]. Finally, the study of adhesion in polymers is also of fundamental importance for the development of structural adhesives and pressure-sensitive adhesives, where performance critically depends on the interaction between adhesion, cohesion, and viscoelastic behavior [21, 22].

Although experimental studies have long demonstrated how the coupling between interfacial adhesion and viscoelasticity in soft rubber-like materials governs contact and frictional phenomena [23], theoretical and numerical frameworks capable of describing these effects in a unified and physically consistent manner are still limited. Classical contact models, often derived for purely elastic and non-adhesive conditions, are unable to account for the dissipative nature of viscoelastic stresses and the non-conservative mechanisms underlying adhesion hysteresis, while numerical approaches that explicitly include finite-range cohesive interactions typically

rely on ad hoc interatomic potentials whose parameters may lack a direct physical interpretation. The aim of this thesis is to contribute to advancing the current state of the art by addressing the aforementioned gap. Specifically, the work focuses on extending the theoretical framework, based on an energetic generalization of Griffith's fracture criterion and originally developed for the adhesive contact of viscoelastic materials with a single-wavelength rigid substrate [24–26], to the more general and technologically relevant case of multiscale rough interfaces. These previous studies have already demonstrated how viscoelastic adhesion can strongly influence the overall system response, particularly with respect to contact area and friction, thereby motivating the need for a unified framework capable of capturing these effects across multiple length scales. By formulating a boundary element approach rooted in Green's function methodology, the proposed model enforces local energy closure conditions at the contact edges, balancing the work of internal stresses and adhesion under infinitesimal virtual variations of the contact domain. The model assumes that adhesive forces act over infinitesimally short ranges; at the same time, the energetic formulation offers a consistent description of hysteresis phenomena arising in both the bulk and the interface. The developed framework enables a consistent treatment of viscoelastic adhesive multi-contact systems, providing physical insight into the mechanisms that govern their contact and frictional behavior.

0.1 The outline of the thesis

The dissertation is organized into four chapters, each addressing a specific aspect of the theoretical, numerical and physical background underlying the present research.

1. Chapter 1 introduces the fundamental theoretical concepts of classical contact mechanics. Starting from the pioneering work of Heinrich Hertz, the chapter discusses the elastic indentation problem and the associated boundary conditions. It then explores the role of intermolecular interactions and surface energy in adhesion phenomena, introducing the Griffith criterion within the context of fracture mechanics. Subsequently, the two cornerstone adhesive contact theories, the Johnson-Kendall-Roberts (JKR) and Derjaguin-Muller-Toporov (DMT) models, are presented and compared, with the Tabor parameter serving as a key element to bridge the two regimes.

2. Chapter 2 focuses on the mechanical behavior of viscoelastic materials. It begins with an overview of the physical origins of viscoelasticity in polymers, describing the interplay between elastic and viscous responses and the associated energy dissipation mechanisms. It then introduces the principal rheological models used to describe linear viscoelastic behavior, followed by the presentation of the Boundary Element Method (BEM) formulation for viscoelastic media based on Green's functions, which provides a robust computational framework for the analyses performed later in the thesis.

3. Chapter 3 examines the problem of contact between rough surfaces, emphasizing the importance of multiscale roughness in determining real contact area and load distribution. After introducing the main statistical and spectral quantities used to characterize rough surfaces, classical models such as the Greenwood-Williamson approach and its extensions are discussed, followed by Persson's theory, which offers a multiscale description capable of linking microscopic surface features to macroscopic contact properties.

4. Chapter 4 constitutes the core of the thesis. Building on the theoretical foundations established in the previous chapters, it extends the energy-based framework for adhesive viscoelastic contact to multiscale rough surfaces under sliding conditions. The model captures the complex interaction between viscoelasticity, adhesion and surface roughness, enabling the quantitative prediction of contact area, adhesive strength and frictional response across the entire viscoelastic spectrum.

Chapter 1

Foundations of contact mechanics and the energy method framework

In this first chapter, the theoretical background that forms the foundation of the present work is introduced. The central focus is the classical problem of the indentation of an elastic half-space by a rigid, frictionless punch, i.e. in the absence of shear stresses at the interface. Such problems are characterized by mixed boundary conditions: within the contact area the displacement fields of the rigid indenter and the elastic medium must coincide, whereas outside the contact region the normal pressure must vanish. The first part of the chapter is devoted to the pioneering contribution of Heinrich Hertz (1882), who provided the first analytical solution to this class of problems. In particular, Hertz's theory describes the case of a rigid sphere pressed against an elastic half-space and remains a cornerstone of modern contact mechanics. The discussion then moves to the fundamental concepts of surface energy and intermolecular interactions, with a specific emphasis on van der Waals forces. These forces, though weak at the molecular scale, are responsible for adhesion phenomena that can significantly alter the mechanics of contact, especially in the case of soft elastic materials. Subsequently, the Griffith criterion is introduced in the framework of fracture mechanics, offering a rigorous energetic interpretation of the interplay between elastic strain energy and surface energy during crack propagation. This perspective proves particularly relevant for contact problems, since the creation of new surface at the edge of a contact can be formally regarded as a mode I fracture process. Building on these foundations, two of the most influential adhesive contact theories are presented: the Johnson–Kendall–Roberts (JKR) model and the Derjaguin–Muller–Toporov (DMT) model. These theories, although based on distinct assumptions regarding the spatial distribution of adhesive forces, provide complementary descriptions of contact mechanics in different adhesive regimes. A detailed comparison is then carried out to show how the applicability of each theory depends on the material properties and geometrical parameters of the contacting bodies. In this context, the Tabor parameter is introduced as a key dimensionless quantity that governs the

smooth transition between the JKR and DMT limits. The overview presented in this chapter is primarily based on the comprehensive reference text by Maugis [27], to which the reader is referred for further details and extended discussions on the topics summarized here.

1.1 Hertz theory of elastic contact

The Hertzian contact theory, developed by Heinrich Hertz in 1882 [28], provides a classical framework to analyze the contact between two elastic bodies under a normal load. In the contact area, a normal pressure develops which can be approximated by a hemispherical-like distribution, vanishing at the edge of the contact to ensure continuity of displacements and to prevent non-physical singularities. The main assumptions of Hertzian theory are: the contact radius is small compared to the local radii of curvature, $a/R \ll 1$, the contacting bodies are large relative to the contact area so that boundary effects are negligible, the surfaces are frictionless and no tensile stresses (adhesion) are present.
We first consider the general case of contact between two elastic spheres of radii R_1 and R_2 (see Fig. 1.1).

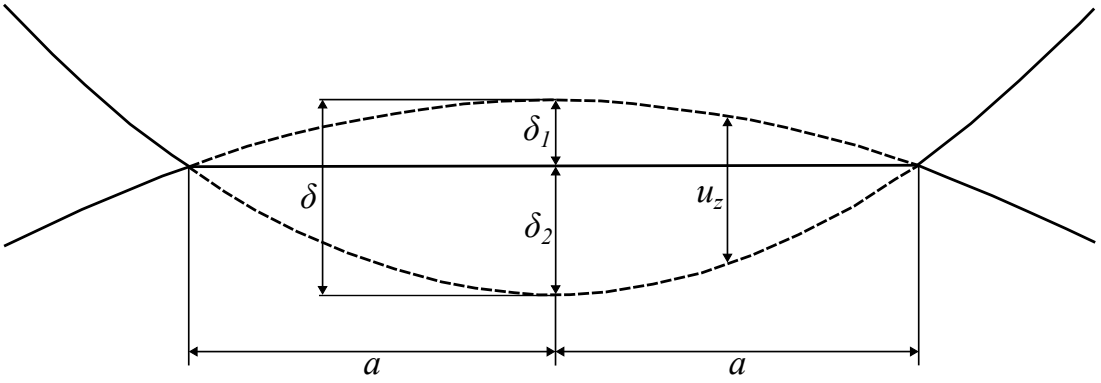

Figure 1.1: Schematic of Hertzian contact between two spheres showing the penetration δ, the vertical displacement u_z and the contact semi-width a, which characterize the local deformation under load

The undeformed shape functions of the spheres can be written as:

$$\begin{aligned} x^2 + y^2 + (z_1 - R_1)^2 &= R_1^2 \\ x^2 + y^2 + (z_2 + R_2)^2 &= R_2^2 \end{aligned} \tag{1.1}$$

For small vertical displacements ($z_1, z_2 \ll R_1, R_2$), the quadratic terms z_1^2 and z_2^2 may be neglected. Expanding the square roots gives the paraboloidal approximations of the undeformed profiles:

$$\begin{aligned} z_1 &\approx \frac{x^2 + y^2}{2R_1} \\ z_2 &\approx -\frac{x^2 + y^2}{2R_2} \end{aligned} \tag{1.2}$$

The initial interfacial separation can therefore be expressed as:

$$h(x,y) = z_1 - z_2 = \frac{x^2 + y^2}{2R} \tag{1.3}$$

with the combined radius of curvature defined as:

$$\frac{1}{R} = \frac{1}{R_1} + \frac{1}{R_2}. \tag{1.4}$$

When the two spheres are pressed together under a load P, they approach each other by $\delta = \delta_1 + \delta_2$, producing local vertical elastic displacements u_{z1} and u_{z2} in the contact region (considered positive when compressive). If we define the radial coordinate r, the compatibility condition within the contact area ($r < a$) is:

$$u_{z1}(r) + u_{z2}(r) = \delta - h(r), \tag{1.5}$$

and outside the contact area the condition of non-interpenetration requires:

$$u_{z1}(r) + u_{z2}(r) > \delta - h(r). \tag{1.6}$$

Hertz solved this problem by assuming a hemispherical pressure distribution acting on a circular region of radius a:

$$p(r) = p_0 \left(1 - \frac{r^2}{a^2}\right)^{1/2} \qquad r \leq a \tag{1.7}$$

which induces a vertical displacement in the elastic bodies:

$$u_{zi}(r) = \frac{1 - \nu_i^2}{E_i} \frac{\pi p_0}{4a}(2a^2 - r^2), \qquad r < a \tag{1.8}$$

with ν_i and E_i the poission ratio and the Young's Modulus of the single sphere, respectively. p_0 is defined as the maximum pressure equal to 1.5 times the mean pressure given by $p_m = P/\pi a^2$. Solving the elasticity problem formally produces a second mathematical solution:

$$p(r) = p_1 \left(1 - \frac{r^2}{a^2}\right)^{-1/2} \qquad r < a \tag{1.9}$$

which induces a corresponding displacement:

$$u_{zi}(r) = \frac{\pi(1 - \nu_i^2)p_1 a}{E_i} \qquad r < a \tag{1.10}$$

The general solution of the problem is therefore a linear combination of these two solutions, by means of the following pressure distribution:

$$p(r) = p_0 \left(1 - \frac{r^2}{a^2}\right)^{1/2} + p_1 \left(1 - \frac{r^2}{a^2}\right)^{-1/2} \tag{1.11}$$

The second mathematical solution, however, represents the classical scenario of an elastic half-space in contact with a flat punch, where the deformed surface exhibits a vertical slope at the edge of the contact region. Consequently, positive values of p_1 are not physically realistic, as they would result in penetration or overlap between the contacting spheres. On the other hand, negative values of p_1 would imply the presence of tensile stresses at the boundary, which are physically permissible only if interfacial adhesion exists. In the absence of adhesion, p_1 must therefore be zero, leaving the Hertzian hemispherical pressure distribution as the only physically valid solution. Consequently the total displacement will be given by:

$$u_z(r) = u_{z1}(r) + u_{z2}(r) = \frac{\pi p_0}{4a}\frac{2a^2 - r^2}{E^*} \tag{1.12}$$

where E^* is the reduced modulus defined as:

$$\frac{1}{E^*} = \frac{1-\nu_1^2}{E_1} + \frac{1-\nu_2^2}{E_2} \tag{1.13}$$

Integrating the pressure distribution gives the total normal load:

$$P = \int_0^a 2\pi r p(r)\, dr = \frac{2}{3}\pi p_0 a^2, \tag{1.14}$$

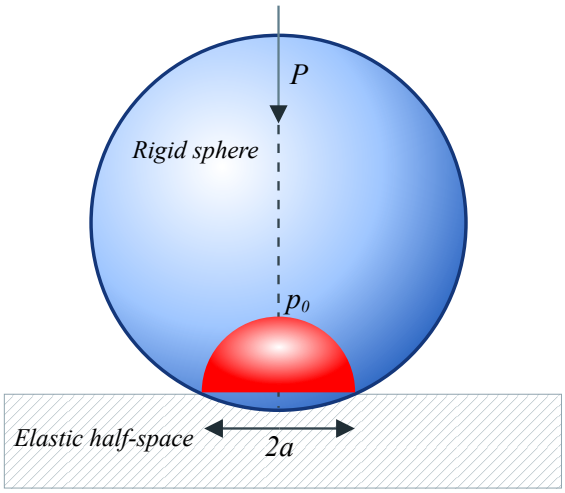

Figure 1.2: Schematic representation of the Hertzian contact between a sphere and an elastic half-space. The contact pressure distribution is approximated by a rotational paraboloid with a planar radius a and a maximum pressure p_0 at the center. At the contact edge, the pressure profile goes to zero (as assumed in Boussinesq's hypothesis) and its slope becomes vertical

The complete Hertz solution provides the fundamental relations between contact radius a, penetration δ, the load P and material properties. For two elastic spheres:

$$\begin{aligned} a^3 &= \frac{3}{4}\frac{PR}{E^*} \\ \delta &= \frac{a^2}{R} \end{aligned} \tag{1.15}$$

As a particular case, when one of the spheres is rigid (e.g., $E_1 \to \infty$) and the other is an elastic half-space, the reduced modulus becomes $E^* = E/(1-\nu^2)$, and the displacement $u_z(r)$ is determined solely by the elastic half-space. All other relations remain formally identical, making the rigid sphere against an elastic half-space a straightforward specialization of the general two-sphere contact problem.

1.2 Basic principles of Van der Waals forces and surface energy

Van der Waals forces are weak intermolecular interactions that arise from temporary fluctuations in the electronic spatial distribution within atoms or molecules. These fluctuations generate instantaneous dipoles, which in turn induce corresponding dipoles in neighboring particles, giving rise to electrostatic attractions. Although significantly weaker than covalent or ionic bonds, van der Waals forces become relevant when a large number of molecules are involved, and they play a fundamental role in adhesion phenomena. This explains, for example, how certain substances adhere without the formation of direct chemical bonds. A well-known case is that of geckos, which can walk on vertical walls and ceilings thanks to the microscopic setae on their feet. In this case, van der Waals interactions between the tips of the setae and the surface generate sufficient adhesive forces to support the animal's weight. This natural principle has inspired the development of artificial micro- and nanostructured adhesives designed to mimic the architecture of gecko feet [10, 29, 30]. Another field where van der Waals forces are essential is atomic force microscopy (AFM), where weak electrostatic interactions between the tip and the sample surface allow extremely precise mapping of topographical features at the atomic and molecular scale. [31–33]

The creation of a new surface in a solid or a liquid involves breaking the cohesive interactions that hold the condensed phase together. This process does not consist solely in the mechanical separation of atoms or molecules, but also requires a slight rearrangement of the particles near the newly formed surface to restore local equilibrium. Consequently, the formation of a surface demands a certain amount of energy, which includes both mechanical work and thermal contributions, and is proportional to the area created. The quantity that describes this phenomenon is the surface energy, defined as the reversible and isothermal work required to create a unit area of new surface.

Several theories have been proposed to explain the cohesive forces in condensed matter and, consequently, the origin of surface energy and surface tension. One of the most widely adopted models is the Lennard-Jones potential, which provides a simplified yet effective description of the interaction between two neutral atoms or molecules. At very short distances, the interaction is dominated by a strong repulsion arising from the Pauli exclusion principle, which prevents the overlap of electronic orbitals with same quantum state. At longer distances, the attractive contribution prevails, associated with van der Waals forces, and more specifically London dispersion forces originating from correlated instantaneous dipoles. The

combination of these two opposing effects results in the characteristic "potential well" shape of the Lennard-Jones interaction, with a minimum at the equilibrium distance where attraction and repulsion balance, yielding a stable configuration.

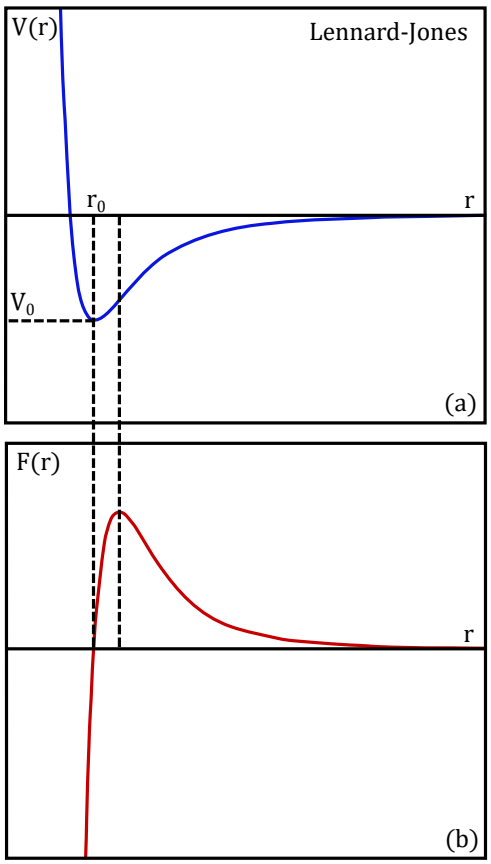

Figure 1.3: Lennard-Jones potential (a) and corresponding force (b) as a function of interparticle distance r. The potential reaches its minimum at the equilibrium distance r_0, where the force is null. For $r < r_0$, the force is repulsive, diverging to infinity as $r \to 0$. For $r > r_0$, the force is attractive, approaching zero at large distances.

Although approximate, this potential offers an intuitive microscopic interpretation of intermolecular interactions and provides a bridge to macroscopic properties such as surface tension and surface energy. From a theoretical standpoint, surface energy can be derived by comparing the interaction energy of a particle within the bulk, where coordination with neighboring particles is maximized, with that at the surface, where part of these interactions is lost. Formally, this amounts to integrating the Lennard-Jones potential over all neighboring particles, distinguishing between bulk contributions and the missing interactions at the surface. The resulting difference provides an estimate of the energetic cost associated with the formation of a new surface. While this approach captures the essence of the phenomenon, it remains a simplified description. In practice, more sophisticated potentials and computational methods such as molecular dynamics or Monte Carlo simulations are often required, especially for complex materials and liquids where

directional interactions or hydrogen bonding play a significant role.
In thermodynamic terms, the surface energy γ of a solid (or liquid) in contact with a gaseous phase is defined as the reversible and isothermal work per unit area required to generate a new surface in equilibrium with its surroundings. The infinitesimal work needed to create an elemental surface area dA is therefore given by $\delta W = \gamma dA$. The total energy of a system containing a surface can then be written as the sum of a bulk contribution U_0 and a surface contribution, such that:

$$U = U_0 + \gamma A \tag{1.16}$$

If we imagine cleaving a solid along an arbitrary plane and separating the two surfaces in vacuum, external work must be supplied to overcome the cohesive forces binding the solid. The work required to create a unit area of surface is, by definition, the surface energy. When two solids, labeled 1 and 2, are in contact over an area A, their energy can be expressed as:

$$U = U_0 + \gamma_{12} A \tag{1.17}$$

where γ_{12} is the interfacial energy. Upon separation, the system's energy becomes:

$$U = U_0 + (\gamma_1 + \gamma_2) A \tag{1.18}$$

Thus, the reversible and isothermal work needed to separate the two solids is given by:

$$\Delta\gamma = \gamma_1 + \gamma_2 - \gamma_{12} \tag{1.19}$$

which is known as Dupré's energy of adhesion. In the special case where the two solids form a single crystal, the interfacial energy γ_{12} vanishes, and the work of separation reduces to $\Delta\gamma = 2\gamma$, corresponding to the theoretical cohesive energy of the solid. The surface energy not only characterizes the energetic cost of creating a new surface, but it can also be used to derive the relationship between the normal stress acting between two surfaces and the inter-molecular distance (gap) separating them. This relationship is often obtained from $m - n$ type potentials, such as the Lennard-Jones potential defined above [34–40]. For a pair of surfaces, the normal stress σ as a function of the gap g can be expressed as:

$$\sigma(g) = \frac{8\Delta\gamma}{3\varepsilon}\left[\left(\frac{\varepsilon}{g}\right)^3 - \left(\frac{\varepsilon}{g}\right)^9\right], \tag{1.20}$$

where ε is the inter-molecular equilibrium distance.

1.3 Griffith criterion for fracture mechanics

From a theoretical standpoint, if two solids in contact were to be separated entirely by breaking all chemical bonds simultaneously, the stress required for separation would be extremely high and proportional to the area itself. However, experimental observations show that the stress actually required to cause breakage is

much lower than the calculated theoretical value. The reason for this discrepancy lies in the fact that fracture mechanisms do not occur through the simultaneous breaking of all bonds, but originate from pre-existing microscopic defects, such as cracks, microvoids or discontinuities, which act as stress concentration points. Once activated, the crack propagates by progressively breaking the bonds, drastically reducing the level of stress required to break the material. A rigorous approach to this problem can be developed in thermodynamic terms [27, 41]. Any thermodynamic system can be defined in terms of macroscopic quantities by means of independent extensive parameters X_i, such as entropy S, volume V and number of particles N. Using these parameters, the internal energy of the system can be defined:

$$U = U(X_i) \tag{1.21}$$

In general, each extensive parameter X_i is associated with an intensive parameter Y_i through the relationship:

$$Y_i = \frac{\partial U}{\partial X_i} \tag{1.22}$$

For instance, the temperature T of the system is obtained as the partial derivative of internal energy with respect to entropy, keeping all other extensive variables (V, N) constant, $T = \partial U/\partial S$.
An isolated system is in equilibrium when virtual variations in its extensive parameters do not produce any variation in internal energy U. Once this condition is reached, the state of the system can be characterised in terms of a state equation of the type $f(X_i) = 0$, which links the independent extensive thermodynamic quantities X_i together. For the rigorous study of equilibrium conditions, thermodynamic potentials are introduced, scalar quantities that are derived from internal energy via Legendre transforms:

$$\Phi = U - Y_j X_j \tag{1.23}$$

This procedure allows certain extensive parameters to be replaced by their corresponding intensive parameters, simplifying the description of the system in terms of the most convenient control variables (e.g. temperature, pressure or applied load). In this manner, the state of equilibrium is identified with the minimum value of the appropriate thermodynamic potential, chosen according to the external constraints to which the system is subjected. Consequently, different thermodynamic potentials can be defined depending on the experimental conditions considered. In particular, Helmholtz free energy F is introduced by setting temperature T and entropy S as control variables:

$$F = U - TS \tag{1.24}$$

whose infinitesimal variation takes the form:

$$dF = -S\,dT - p\,dV + Y_i\,dX_i + \dots \tag{1.25}$$

Similarly, when the effects of pressure p and volume V are also included, Gibbs free energy $\mathcal{G}$ is defined as:

$$\mathcal{G} = U - TS + pV \tag{1.26}$$

with the corresponding differential:

$$d\mathcal{G} = -S\,dT + V\,dp + Y_i\,dX_i + \dots \tag{1.27}$$

This approach, characteristic of fracture mechanics, can also be extended to the study of contact mechanics, since the variation in the contact area between two bodies can be considered, from an energy perspective, as a mode I fracture [42]. So let us consider the case of two solids in adhesive contact over an area A, subject to an external load P or an imposed displacement δ, as in Fig. 1.4.

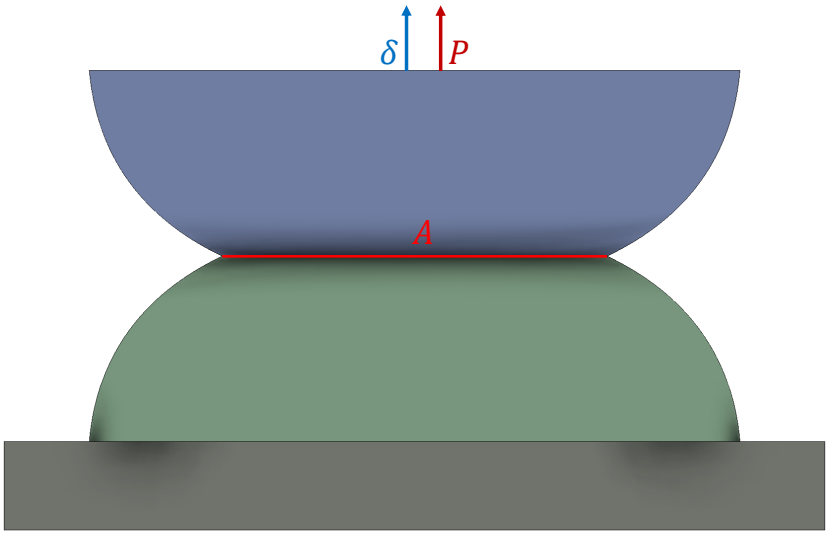

Figure 1.4: Schematic representation of two deformable bodies in adhesive contact, highlighting the interaction region of area A, the applied load P and the displacement δ

In this case, the internal energy of the system will be of the type $U = U(S, \delta, A)$ and can be divided into two contributions, namely the elastic energy of the system, defined as:

$$U_{el} = \frac{1}{2}\int \sigma_{ij}\varepsilon_{ij}dV \tag{1.28}$$

and the surface energy:

$$U_S = -\Delta\gamma A \tag{1.29}$$

The differential of the internal energy of the system therefore takes the form:

$$dU = \left.\frac{\partial U}{\partial S}\right|_{\delta,A} dS + \left.\frac{\partial U}{\partial \delta}\right|_{S,A} d\delta + \left.\frac{\partial U}{\partial A}\right|_{S,\delta} dA \tag{1.30}$$

which, using thermodynamic correspondences, becomes:

$$dU = TdS + Pd\delta + (G - \Delta\gamma)dA \tag{1.31}$$

with $(G - \Delta\gamma)$ being the crack extension force per unit length of crack. In this formulation, the energy release rate G has been introduced, which in this case quantifies the variation in elastic energy of the system as the contact area A varies, keeping the displacement δ constant. Therefore, the thermodynamic state of the system is fully determined by the following equations of state, which relate the intensive parameters to the independent extensive variables:

$$\begin{cases} T = T(\delta, A, S) \\ P = P(\delta, A, S) \\ G = G(\delta, A, S) \end{cases} \tag{1.32}$$

The equilibrium of the system can then be investigated, at constant temperature, both under conditions of fixed applied load P and under conditions of imposed displacement δ. In such cases, the description is more convenient using Gibbs free energy or Helmholtz free energy, respectively. For this specific problem, the expressions of the differentials 1.25 and 1.27 are reduced to:

$$dF = Pd\delta + (G - \Delta\gamma)dA - SdT \tag{1.33}$$

$$d\mathcal{G} = -\delta dP + (G - \Delta\gamma)dA - SdT \tag{1.34}$$

From equations 1.33 and 1.34, we observe that, at constant temperature, equilibrium under conditions of fixed applied load ($dT = 0$, $dP = 0$) corresponds to a minimum of Gibbs free energy $\mathcal{G}$. Similarly, under conditions of imposed displacement ($dT = 0$, $d\delta = 0$), equilibrium is associated with a minimum of Helmholtz free energy F. In both cases, the equilibrium condition leads to the same result:

$$G = \Delta\gamma \tag{1.35}$$

known as Griffith's criterion of equilibrium [43]. It follows that crack propagation can only take place if the system is able to supply the energy necessary to break the atomic bonds and consequently form a new free surface, i.e. when the energy release satisfies the inequality:

$$G \geq \Delta\gamma \tag{1.36}$$

The nature of the equilibrium defined by Griffith's criterion can be stable, unstable or neutral. Mathematically, stability is linked to the sign of the second derivative of the energy potential considered with respect to the crack area. The equilibrium point will be stable when the corresponding potential is minimal. Hence, at constant temperature and fixed displacement, the condition for stability is:

$$\left.\frac{\partial^2 F}{\partial A^2}\right|_{\delta,T} = \left.\frac{\partial G}{\partial A}\right|_{\delta} > 0 \tag{1.37}$$

while at constant temperature and fixed load it reads:

$$\left.\frac{\partial^2 \mathcal{G}}{\partial A^2}\right|_{P,T} = \left.\frac{\partial G}{\partial A}\right|_{P} > 0 \tag{1.38}$$

1.4 JKR adhesive contact theory

The Hertzian contact described in section 1.1 is valid only in the absence of attractive forces between surfaces. However, in case of soft elastic materials, characterised by a low Young's modulus (such as natural rubber), a high surface energy can lead to a contact area significantly larger than that predicted by the classical Hertz theory. To account for adhesive effects, Johnson, Kendall, and Roberts developed in 1971 one of the most established frameworks in the field [44], known as the JKR theory. This model is based on the balance between elastic energy, potential energy and surface energy, and can be regarded as an extension of Griffith's energy criterion introduced in section 1.3. Consider the adhesive contact between a rigid sphere of radius R and a linear elastic half-space. The JKR theory assumes that normal attractive stresses between the two surfaces can be sustained as long as their normal separation tends to zero, an assumption referred to as the infinitely short-range adhesive forces hypothesis. Within this framework, the term p_1 of the general pressure distribution takes negative values:

$$p_1 = \frac{E^*}{\pi}\left(\frac{\delta}{a} - \frac{a}{R}\right) \tag{1.39}$$

leading to the pressure profile expressed by equation 1.11, which has a singularity at the edge of the contact.
As mentioned above, the unknown contact area can be determined by imposing an energy balance on the system. In the case study, the elastic energy expressed by equation 1.28 can be rewritten in the form:

$$U_{el} = \pi \int p(r)u(r)rdr \tag{1.40}$$

Replacing the pressure profile 1.11 in this expression, the elastic energy takes the form:

$$U_{el}(\delta, a) = E^*\delta^2\left(a - \frac{2a^3}{3R\delta} + \frac{a^5}{5R^2\delta^2}\right) \tag{1.41}$$

Similarly the surface adhesion energy can be expressed as:

$$U_S(a) = -\Delta\gamma\pi a^2 \tag{1.42}$$

At this stage, the equilibrium condition of the system is obtained by requiring that the total energy $U(\delta, a) = U_{el}(\delta, a) + U_S(a)$ be stationary with respect to the variation of the contact area a under fixed grips:

$$\left.\frac{\partial U}{\partial a}\right|_{\delta} = 0 \tag{1.43}$$

Maugis et al. [42] also proved that the JKR theory was consistent with linear elastic fracture mechanics, considering the contact edge as a mode I crack opening. In this context, the equilibrium point is defined by the energy criterion $G = \Delta\gamma$ and

the stability of the system is guaranteed by the condition $(\partial G/\partial A) > 0$. From this equilibrium, it is possible to derive the relationships that link the contact radius a with the penetration δ and with the total compression force P. In particular, we obtain:

$$\frac{\delta}{R} = \left(\frac{a}{R}\right)^2 - \left(\frac{a}{R}\right)^{1/2} \sqrt{\frac{2\pi\Delta\gamma}{E^* R}} \tag{1.44}$$

$$\frac{P}{E^* R^2} = \frac{4}{3}\left(\frac{a}{R}\right)^3 - 2\left(\frac{a}{R}\right)^{3/2} \sqrt{\frac{2\pi\Delta\gamma}{E^* R}} \tag{1.45}$$

The previous relationships are represented in Figure 1.5 in dimensionless form.

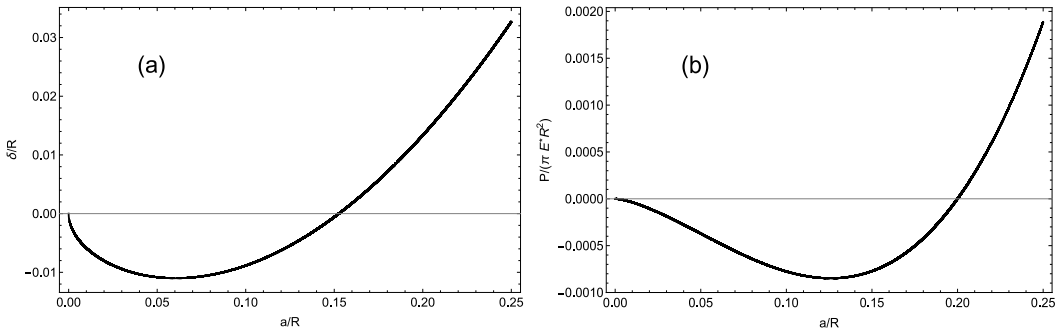

Figure 1.5: JKR results: (a) The dimensionless contact penetration vs. the dimensionless contact radius. (b) The dimensionless applied force vs. the dimensionless contact radius. Results are shown for dimensionless adhesion energy $\Delta\gamma/(\pi E^* R) = 0.00018$

In presence of surface energy, the contact area remains finite even for negative values of the applied load, until a critical force is reached beyond which the surfaces separate abruptly. This critical force, indicated as P_c, represents the stability limit of the system and is commonly identified with the adhesion force (or pull-off force) between the two solids. On the equilibrium curve $P(\delta)$, the loss of stability manifests itself differently depending on the experimental conditions: in the case of controlled load tests, it corresponds to a horizontal tangent and the critical values are:

$$\begin{aligned} P_c &= \frac{3}{2}\pi\Delta\gamma R \\ a_{min} &= \left(\frac{9\pi\Delta\gamma R^2}{8E^*}\right)^{1/3} \\ \delta_{min} &= \left(\frac{3\pi^2\Delta\gamma^2 R}{64E^{*2}}\right)^{1/3} \end{aligned} \tag{1.46}$$

whereas in the case of controlled displacement tests, the instability condition is associated with a vertical tangent of the curve and leads to a smaller contact area,

with the following values:

$$\begin{aligned} P_c &= \frac{5}{6}\pi\Delta\gamma R \\ a_{min} &= \left(\frac{\pi\Delta\gamma R^2}{8E^*}\right)^{1/3} \\ \delta_{min} &= \left(\frac{27\pi^2\Delta\gamma^2 R}{64E^{*2}}\right)^{1/3} \end{aligned} \tag{1.47}$$

It is worth noting that in both cases, the value of the critical force P_c does not depend on the elastic modulus of the materials involved, but only on the radius of curvature R and the surface energy. This behaviour is illustrated in Figure 1.6, which shows the equilibrium curve of the dimensionless force as a function of normalised displacement. Points A and B identify the pull-off conditions for tests conducted under controlled load and controlled displacement, respectively.

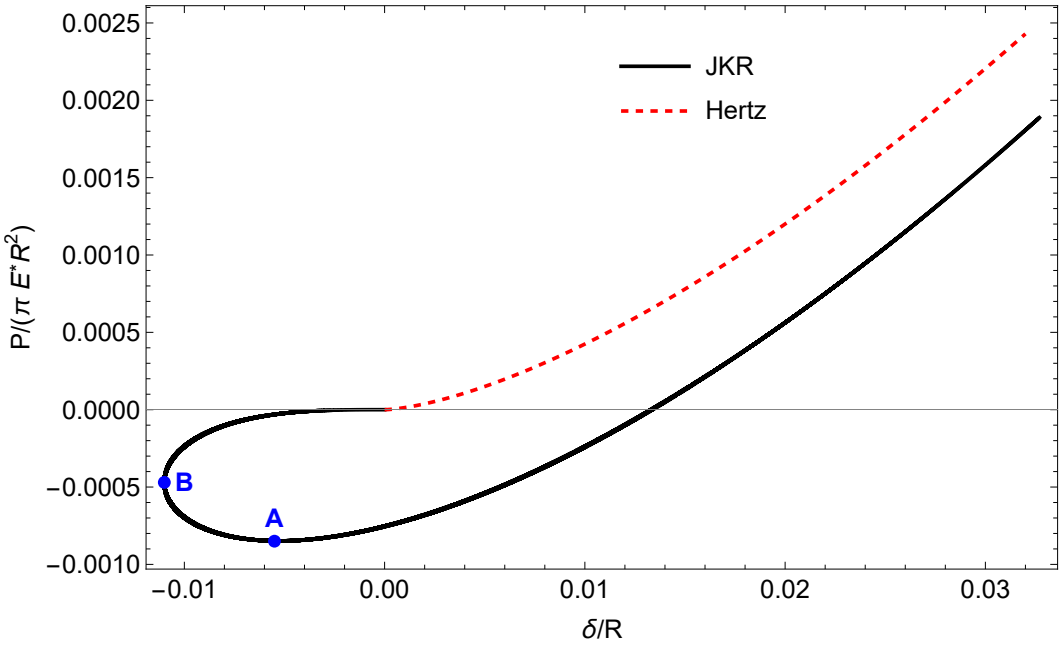

Figure 1.6: Comparison between Hertzian and JKR predictions of the dimensionless contact force as a function of the dimensionless indentation. Results are shown for dimensionless adhesion energy $\Delta\gamma/(\pi E^* R) = 0.00018$. For $\Delta\gamma = 0$, the JKR solution coincides with the Hertzian prediction. Points A and B denote the critical pull-off force P_c under load control and displacement control conditions, respectively

1.5 DMT adhesive contact theory and the JKR-DMT transition

In the 1930s, Bradley (1932) [45] and Derjaguin (1934) [46] investigated the adhesion between a rigid sphere and a half-space by neglecting the elastic deformations of the contacting bodies. His approach was based on surface interactions modeled through Lennard-Jones type potentials and led to a pull-off force equal to $2\pi\Delta\gamma R$. This result appeared to be in contrast with the prediction later obtained by the classical Johnson–Kendall–Roberts (JKR) theory, reported in Equation 1.46. In order to address this apparent discrepancy, Derjaguin, Muller, and Toporov developed in 1975 a new theoretical framework, now known as the DMT model [47,48]. Interestingly, while this theory incorporated the role of elastic deformations of the contacting bodies, the predicted pull-off force remained coincident with the value previously derived by Bradley. The distinctive feature of the DMT theory lies in the treatment of adhesive forces. Unlike the JKR model, in which adhesion is incorporated within the contact region itself, the DMT approach assumes that attractive interactions act exclusively outside the contact area as long-range forces. Within the contact zone, the pressure distribution remains purely elastic and follows the classical Hertzian formulation, unaffected by adhesion. As a consequence, the adhesive forces act only externally without altering the local stress state inside the contact region. This leads the DMT model to predict smaller contact areas than those obtained from the JKR theory for the same material properties and loading conditions. In order to resolve the apparent inconsistency between the JKR and DMT theories, Tabor, in 1976 [49], carried out a systematic comparison of the two models. He demonstrated that the actual behavior of adhesive contacts does not follow one theory exclusively, but rather spans a continuum between the two limiting descriptions. To quantify this transition, he introduced the dimensionless Tabor parameter:

$$\mu_T = \left(\frac{\Delta\gamma^2 R}{E^{*2} Z_0^3}\right)^{1/3} = \frac{l^{2/3} R^{1/3}}{Z_0}, \tag{1.48}$$

where Z_0 denotes the equilibrium atomic distance and $l = \Delta\gamma/E^*$ is the so-called adhesion length. This parameter essentially represents the ratio between the characteristic adhesion energy and the elastic strain energy, thereby providing a criterion to assess whether adhesive interactions can be considered short- or long-ranged. When $\mu_T \ll 1$, the assumptions underlying the DMT model are appropriate, corresponding to hard solids, small radii of curvature and low surface energies. Conversely, for $\mu_T \gg 1$, the JKR description becomes more accurate, as is the case for soft materials, large radii and strong adhesive interactions. The progressive variation of μ_T thus governs a smooth transition between the two theoretical limits, rather than a sharp dichotomy. Tabor's predictions have been extensively validated by later analytical studies and by detailed numerical simulations based on local force balance [50–52]. In particular, Greenwood [52] pointed out that the JKR solution can be regarded as essentially exact when $\mu_T \gg 3$.

Chapter 2

Fundamentals of linear viscoelasticity

Nowadays, polymers constitute a class of materials of growing interest in the scientific and industrial field. Their unique mechanical, thermal and chemical properties, combined with remarkable design versatility, enable their use in a wide range of application areas, including automotive, micro- and nano-engineering, biomedical and aerospace. In the automotive sector, for instance, viscoelastic materials such as rubber compounds are used in tires, where they strongly influence grip and drift conditions as well as dynamic response on the road. Similarly, they are used in damping devices, anti-vibration mounts and polymer bearings, which benefit from their ability to dissipate energy and reduce mechanical vibrations. Although polymers and rubbers are the most commonly used viscoelastic materials at room temperature, viscoelastic behavior can emerge in many materials depending on temperature and stress regime. As a practical example, steel, while typically considered elastic, can exhibit viscoelastic behavior at elevated temperatures, requiring the use of models that account for the viscous component even for conventional structural materials. Viscoelastic materials exhibit mechanical behavior intermediate between that of purely elastic solids and viscous fluids. When subjected to a stress, they initially respond with instantaneous elastic deformation, which follows a time-independent relationship between stress and strain. The mechanical energy stored in this phase is fully returned upon removal of the load, similar to what occurs in ideal elastic materials. Superimposed on this elastic response is a viscous component, the evolution of which is a function of time, associated with internal flow and energy dissipation phenomena. This viscous component is manifested by a gradual increase in strains (creep) in the case of constant stresses, or by a decrease in stresses (relaxation) in the case of constant strains, phenomena that tend to stabilize over time by asymptotically reaching a plateau. This behavior is intimately related to the molecular structure of these types of materials. Polymers can be described as long-chain macromolecules consisting of repeating structural units (monomers), whose chemical nature, configuration and degree of cross-linking significantly determine the macroscopic properties of the material. Depending on the spatial arrangement and mobility of the chains, polymers can

be soft and flexible materials or rigid and resistant solids.
From a physical-chemical point of view, the properties of polymers derive from the interaction between structural and thermodynamic factors. The length and branching of the chains influence the viscosity and glass transition temperature (Tg), a parameter that distinguishes glassy behaviour from rubbery behaviour. The degree of crystallinity, i.e. the ordered fraction of the chains with respect to the amorphous regions, significantly determines the density, optical transparency and mechanical strength of the material. Intermolecular interactions, such as hydrogen bonds and van der Waals forces, help to stabilise the structure, providing cohesion and stiffness. In cross-linked polymers, the presence of covalent bonds between chains limits molecular mobility, increasing thermal stability but reducing overall deformability. Furthermore, the polymer chains constituting the material can slide, stretch and readjust from their initial configuration in response to mechanical stress. Such microscopic reorganization mechanisms induce internal friction between the chains, giving rise to hysteresis and energy dissipation phenomena. In daily life, the versatile nature of polymers is evident in a wide range of applications. The elasticity of silicone, the strength of polyethylene used in bottles, and the dissipative properties of rubber are emblematic examples of the different mechanical responses that can be attributed to the molecular dynamics governing these materials.

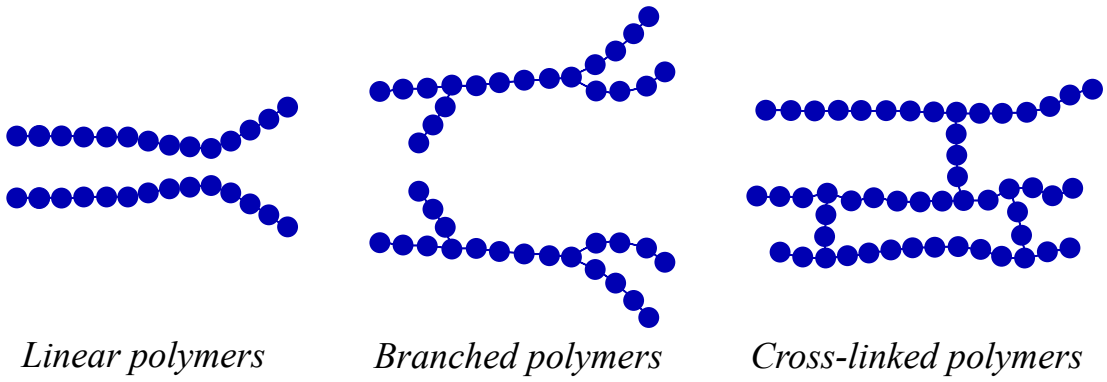

Figure 2.1: Schematic representation of different polymer structures: linear polymer, branched polymer and cross-linked polymer. The molecular topology strongly influences the mechanical, thermal and rheological properties of the material

Accordingly, this chapter will delve into the main mathematical models used to describe linear viscoelastic behavior, with particular reference to rheological modeling. The first section of the chapter will present the main constitutive models used in rheology, which allow viscoelastic behavior to be described in terms of ideal elastic and viscous elements. The second section will introduce the Boundary Element Method (BEM) approach, based on the use of Green's function, which allows solving the viscoelastic problem by providing a direct relationship between the displacement and deformation fields, with significant advantages for numerical implementation. This approach will provide the theoretical basis for the analyses presented in the following chapters.

2.1 Mathematical modeling of linear viscoelastic behavior

In this discussion we examine the viscoelastic behavior of materials in the linear regime. In that regime, the stress $\sigma(t)$ is a linear function of the strain $\varepsilon(t)$, described by means of a linear operator $\mathcal{L}$, i.e. $\sigma(t) = \mathcal{L}[\varepsilon(t)]$. For the linearity of the operator, the usual superposition properties apply, namely:

$$\sigma(t) = \mathcal{L}[\alpha\varepsilon_1(t) + \beta\varepsilon_2(t)] = \alpha\mathcal{L}[\varepsilon_1(t)] + \beta\mathcal{L}[\varepsilon_2(t)] = \alpha\sigma_1(t) + \beta\sigma_2(t) \tag{2.1}$$

where α and β are real constants, and $\sigma_1(t)$ and $\sigma_2(t)$ are the responses corresponding to the inputs $\varepsilon_1(t)$ and $\varepsilon_2(t)$. Moreover, the constitutive equation for these types of materials possesses the properties of causality and time-invariance. A system turns out to be time invariant when its response does not depend on the time value of the function in absolute terms, but only on the content of the input signal. Formally, given a system S, it will result in:

$$x(t) \xrightarrow{S} y(t) \quad \Rightarrow \quad x(t - t_0) \xrightarrow{S} y(t - t_0) \tag{2.2}$$

Consequently, if the input is delayed by a time t_0 the response of the system will be delayed by exactly the same time interval. As for the causality principle, this represents a fundamental cause-and-effect law to which all physical systems are subject, which states how future events cannot affect the past response of a system:

$$\varepsilon_1(t) = \varepsilon_2(t), \quad \forall t \leq t_0 \quad \Longrightarrow \quad \sigma_1(t) = \sigma_2(t), \quad \forall t \leq t_0 \tag{2.3}$$

In purely elastic materials, the constitutive law between stress and strain is instantaneous and described by Hooke's law:

$$\sigma(t) = E\varepsilon(t) \tag{2.4}$$

where E is Young's modulus, constant over time. In viscoelastic materials, however, this relationship is more complex, since the response depends on the time history of the deformation. To model this dependence, the Boltzmann superposition principle is adopted, which extends the concept of linearity of the constitutive equation to include time effects. To motivate its integral formulation, the approximation of the deformation function by step functions is considered. Let $A \subseteq \mathbb{R}$ be a measurable set, we define the characteristic (or indicator) function $\chi_A : \mathbb{R} \to \{0, 1\}$ as:

$$\chi_A(t) = \begin{cases} 1, & \text{if } t \in A, \\ 0, & \text{if } t \notin A. \end{cases} \tag{2.5}$$

Given a finite partition $a = t_0 < t_1 < \cdots < t_n = b$ of a closed, finite interval $I = [a, b] \subset \mathbb{R}$, a step function is defined as a linear combination of characteristic functions:

$$\varphi(t) = \sum_{i=1}^{n} c_i \, \chi_{[t_{i-1}, t_i)}(t) \tag{2.6}$$

where $c_i \in \mathbb{R}$ are constants such that $\varphi(t) = c_i$ for every $t \in [t_{i-1}, t_i)$, and $\varphi(t) = c_n$ for $t = b$. It is known that any measurable function bounded on I can be approximated arbitrarily well by a succession of step functions $\varphi_n(t)$. Using the equation 2.6, the deformation over time can then be approximated as:

$$\varepsilon(t) \approx \sum_{i=1}^{n} \varepsilon_i \, \chi_{[t_{i-1},t_i)}(t) \tag{2.7}$$

Since the indicator function of an interval can be expressed as the difference of two Heaviside functions $H(t)$, the following is true:

$$\chi_{[t_{i-1},t_i)}(t) = H(t - t_{i-1}) - H(t - t_i) \tag{2.8}$$

Therefore, using the equation 2.8 and rephrasing the summation appropriately, the deformation can be rewritten as a weighted sum of Heaviside functions centered at the discontinuity points:

$$\varepsilon(t) \approx \sum_{i=1}^{n} \Delta\varepsilon_i \cdot H(t - t_i) \tag{2.9}$$

where $\Delta\varepsilon_i = \varepsilon(t_i^+) - \varepsilon(t_i^-)$ represents the instantaneous strain increment applied at t_i.
Applying a unit strain step $\varepsilon(t) = H(t)$ at time $t = 0$, the stress response of the viscoelastic material is described by the function $R(t)$, called the relaxation function. Because of the linearity of the system, the total stress is given by the sum of the responses to each increment:

$$\sigma(t) \approx \sum_{i=1}^{n} R(t - t_i) \cdot \Delta\varepsilon_i \tag{2.10}$$

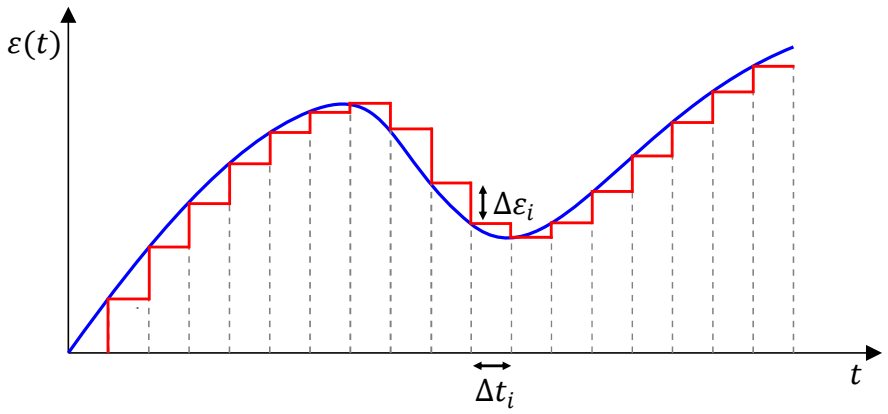

Figure 2.2: Approximation of the strain function by means of a step function

Moving to the continuous limit $\Delta\varepsilon_i \to d\varepsilon(t_1)$ the integral form of Boltzmann's superposition principle is obtained:

$$\sigma(t) = \int_{-\infty}^{t} R(t - t_1) \, \dot{\varepsilon}(t_1) \, d\tau \tag{2.11}$$

This expression represents a time convolution product between the relaxation function $R(t)$ and the derivative of the strain $\dot{\varepsilon}(t)$. Similarly, the strain in response to a unit stress $\sigma(t) = H(t)$ is described by the creep function $J(t)$, and for a generic input the following holds:

$$\varepsilon(t) = \int_{-\infty}^{t} J(t - t_1)\, \dot{\sigma}(t_1)\, d\tau \tag{2.12}$$

These formulations highlight the time dependence of viscoelastic behavior since the response at a given instant depends on the entire past history of stress or strain, weighted according to the value of the relaxation or creep function. In the special case where the elastic modulus E is constant over time, the functions $R(t)$ and $J(t)$ are reduced to constants, and the integral equations above revert to the classical form of Hooke's law 2.4. Assuming sufficient regularity of $R(t)$ and $J(t)$, the equations 2.11 and 2.12 can be rewritten in an equivalent form through integration by parts as follows:

$$\sigma(t) = R(0^+)\varepsilon(t) + \int_{-\infty}^{t} \dot{R}(t - t_1)\, \varepsilon(t_1)\, d\tau \tag{2.13}$$

$$\varepsilon(t) = J(0^+)\sigma(t) + \int_{-\infty}^{t} \dot{J}(t - t_1)\, \sigma(t_1)\, d\tau \tag{2.14}$$

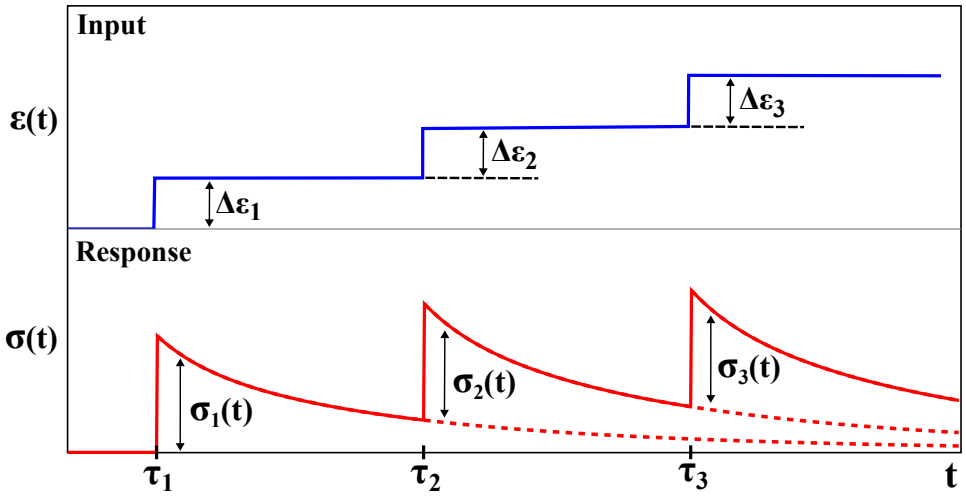

Figure 2.3: A representation of the Boltzmann superposition principle. The tension response of the viscoelastic material is obtained as the sum of the individual responses at each step

The functions $R(t)$ and $J(t)$ can be approximated by means of simplified models formed by purely elastic elements and purely viscous elements, namely by means of springs and dampers, placed in series or in parallel. In the case where stress is to be expressed as a function of strain, it is more convenient to use the Marxwell model, which is a model consisting of a spring and a dumper in series, and which

thus allows the relaxation function to be derived. Consequently, in this system the force applied to the 2 elements turns out to be the same, while the displacement results differently. Mathematically, this model can be described by the equation:

$$\dot{\varepsilon}(t) = \frac{\sigma(t)}{\eta} + \frac{\dot{\sigma}(t)}{E} \tag{2.15}$$

where E is the stiffnes of the spring and η is the damping coefficient of the damper. If we define the ratio $\tau = \eta/E$ as relaxation time of the element, by applying a unit strain step, the solution of Eq. (2.15) leads to:

$$R(t) = E \exp(-t/\tau) H(t) \tag{2.16}$$

By inserting n Marxwell elements in parallel we obtain a generalization of the model (Fig.2.4(a)), which returns a behavior more similar to that of real viscoelastic materials. Mathematically, this is done by rewriting the equation 2.16 by means of a Prony series:

$$R(t) = \left[E_0 + \sum_{i=1}^{n} E_i \exp(-t/\tau_i) \right] H(t) \tag{2.17}$$

where E_0 turns out to be the elastic modulus of the material for $t \to \infty$. In fact, viscoelastic materials over time respond at time $t = 0^+$ as rigid elastic materials with modulus $E_\infty = \sum_{i=0}^{n} E_i$, and then decrease the value of $E(t) = \sigma(t)/\varepsilon(t)$ over time to a minimum value E_0. Conversely, it is easier to describe the deformation as a function of applied stress by resorting to Voigt's model, consisting of a spring and damper set up in parallel, from which the creep function can be derived. Thus in this model the displacement applied to the 2 elements turns out to be the same, while the force is distributed over the 2 branches differently:

$$\sigma(t) = \dot{\varepsilon}(t)\eta + \varepsilon(t)E \tag{2.18}$$

Therefore applying a unit stress step and solving the equation 2.18 we get:

$$J(t) = \frac{1}{E} \left[1 - \exp(-t/\tau) \right] H(t) \tag{2.19}$$

and the generalization of this model (Fig.2.4(b)) leads to a creep function of the form:

$$J(t) = \left[\frac{1}{E_\infty} + \sum_{i=1}^{n} \frac{1}{E_i} \left[1 - \exp(-t/\tau_i) \right] \right] H(t) \tag{2.20}$$

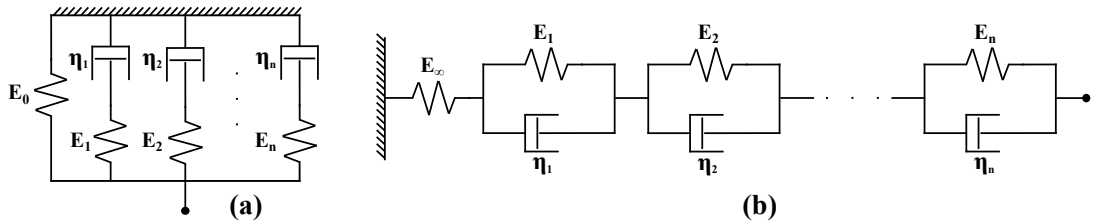

Figure 2.4: Schematic representation of the main generalized viscoelastic models. In (a) is shown the generalized Maxwell model, consisting of multiple Maxwell elements arranged in parallel. In (b) is shown the generalized Voigt model, consisting of multiple Voigt elements arranged in series

Then, in the general multidimensional case, we can rewrite the equations 2.11 and 2.12 in tensor form as:

$$\begin{aligned} \sigma_{ij}(t) &= \int_{-\infty}^{t} R_{ijkl}(t-t_1)\,\dot{\varepsilon}_{kl}(t_1)\,dt_1 \\ \varepsilon_{ij}(t) &= \int_{-\infty}^{t} J_{ijkl}(t-t_1)\,\dot{\sigma}_{kl}(t_1)\,dt_1 \end{aligned} \tag{2.21}$$

with R_{ijkl} and J_{ijkl} being the relaxation tensor and the creep tensor, respectively, whose individual components follow what was said for the relaxation and creep functions.
A viscoelastic material, when subjected to a periodic stress, after an initial transient phase, responds with a constant complex elastic modulus $E(\omega)$. Therefore, the behavior of a linear viscoelastic material can be completely described from its response to a sinusoidal input. In the case of a purely elastic material, the stress and the strain result in phase, i.e., the phase shift between the two signals is zero, since the material's response is instantaneous. In contrast, a purely viscous fluid exhibits a δ phase shift equal to 90° between stress and strain. A viscoelastic solid, whose behavior lies between the two extreme cases above, has a phase shift between 0° and 90°. A qualitative comparison of the frequency responses of the three materials is shown in Figure 2.5.

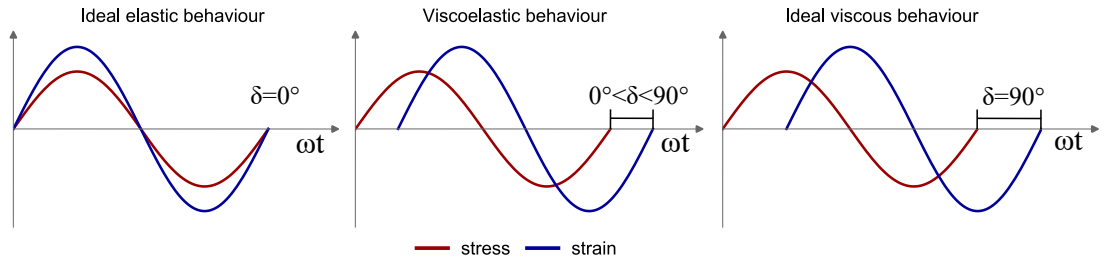

Figure 2.5: Comparison of the sinusoidal input response between a purely elastic material, a viscoelastic material, and a viscous Newtonian fluid

By applying the Fourier transform to the constitutive equations 2.11 and 2.12, the

following expressions are obtained:

$$\begin{aligned} \sigma(\omega) &= i\omega R(\omega)\varepsilon(\omega) \\ \varepsilon(\omega) &= i\omega J(\omega)\sigma(\omega) \end{aligned} \tag{2.22}$$

from which it is possible to define complex modulus as $E(\omega) = i\omega R(\omega)$ and complex compliance as $C(\omega) = i\omega J(\omega)$. The identity is easily derived from these relations:

$$E(\omega)C(\omega) = -\omega^2 J(\omega)R(\omega) = 1 \tag{2.23}$$

which makes it possible to move from knowledge of complex modulus to complex compliance and vice versa. Thus it becomes evident how although the equations 2.17 and 2.20 are derived from different theoretical models, they describe the same physical phenomenon. By once again applying the Fourier transform to the expressions 2.17 and 2.20, we arrive at an analytical formulation for $E(\omega)$ and $C(\omega)$:

$$\begin{aligned} E(\omega) &= E_0 + \sum_{i=1}^{n} E_i \frac{i\omega\tau_i}{1 + i\omega\tau_i} \\ C(\omega) &= \frac{1}{E_\infty} + \sum_{i=1}^{n} \frac{1}{E_i} \frac{1}{1 + i\omega\tau_i} \end{aligned} \tag{2.24}$$

The analysis of these expressions shows that at low frequencies ($\omega \to 0$), the material behaves like a soft solid with an elastic modulus equal to E_0, while as the frequency increases ($\omega \to \infty$), the behavior tends to that of a rigid solid characterized by a modulus $E_\infty > E_0$. This highlights how the apparent stiffness of the material increases with the frequency of excitation: at low frequencies the material has more time to relax and is therefore softer, while at high frequencies the polymer chains fail to reorganize in time, generating stiffer behavior. A fundamental parameter for studying the frequency response of a viscoelastic material is the loss tangent, defined as the ratio of the imaginary part to the real part of the complex modulus:

$$\tan(\delta) = Im\left[E(\omega)\right] / Re\left[E(\omega)\right] \tag{2.25}$$

The trend of the loss tangent and the real and imaginary components of the complex modulus as a function of frequency is shown in Figure 2.6. This behavior allows three main regimes to be identified: rubbery, glassy and viscoelastic transition. In the rubbery regime, at very low frequency, the material behaves as a very soft solid with elastic modulus E_0. In the glassy regime, at very high frequencies, it still behaves elastically but with a higher modulus E_∞. The intermediate region is where the typical behavior of viscoelastic materials occurs: the loss tangent increases, the response is strongly hysteretic, and significant energy dissipation per stress cycle is observed. In such a regime, if the material is subjected to cyclic deformation, some of the mechanical energy is dissipated as heat due to internal hysteresis. This phenomenon underlies the generation of viscoelastic friction observed in sliding or rolling contacts between viscoelastic surfaces, which will be discussed in later chapters.

In the case of a linear viscoelastic material characterized by a single relaxation time τ, a peak dissipation is observed at the maximum of the phase shift, for an excitation frequency $\omega = 1/\tau$. At such a frequency, the material is in an intermediate condition between purely elastic and purely viscous behavior, in which the energy dissipation per stress cycle is maximum. In the more realistic case of a material having multiple relaxation times or a spectrum of relaxation times, the behavior is described by a superposition of several elementary viscoelastic processes. In that case, the $\tan(\delta)$ peak is no longer associated with a single characteristic time, but results from the superposition of multiple dissipative contributions over a range of frequencies. The result is a broader and less sharp peak, whose position and amplitude depend on the distribution of relaxation times.
As previously discussed, polymers, the primary constituents of many viscoelastic materials, consist of long molecular chains that can be either physically entangled or chemically cross-linked to varying degrees. As temperature increases, the mobility of these chains enhances, leading to increased creep deformation and changes in the characteristic relaxation times of the material. This temperature dependence represents a key aspect in the modeling of viscoelastic behavior, since frequency and temperature are not independent variables, but jointly determine the mechanical response of the material. From a mathematical standpoint, this interdependence manifests as a shift of the loss tangent (or the imaginary part of the complex modulus) peak toward higher frequencies with increasing temperature, as illustrated in Figure 2.8.

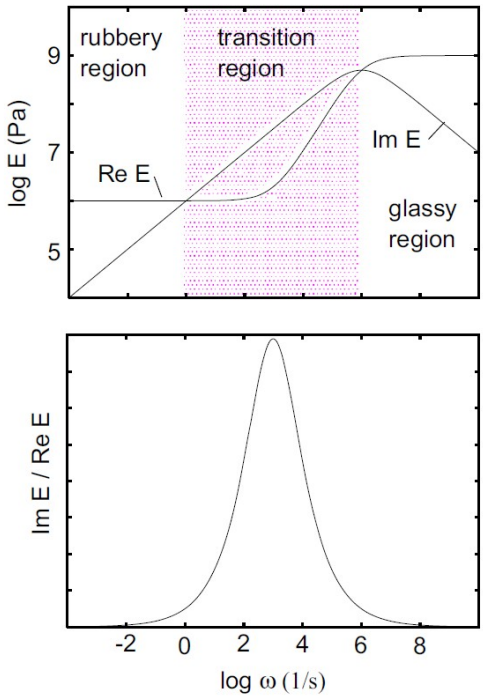

Figure 2.6: (a) Trend of the real ($Re\,[E(\omega)]$) and imaginary ($Im\,[E(\omega)]$) components of the complex modulus as a function of the excitation frequency. (b) Trend of loss tangent $\tan(\delta)$ as a function of excitation frequency

This temperature-frequency equivalence is experimentally investigated through Dynamic Mechanical Analysis (DMA), a technique that measures the viscoelastic response of a material subjected to a sinusoidal deformation. From the measured stress and strain signals, the amplitude ratio and the phase lag δ between them are determined. These quantities allow the evaluation of the storage modulus $E' = Re\,[E(\omega)]$ and loss modulus $E'' = Im\,[E(\omega)]$, representing respectively the elastic energy stored and the viscous energy dissipated during each loading cycle. Their ratio defines the loss tangent defined in the equation 2.25, which provides a measure of the material's damping capability.

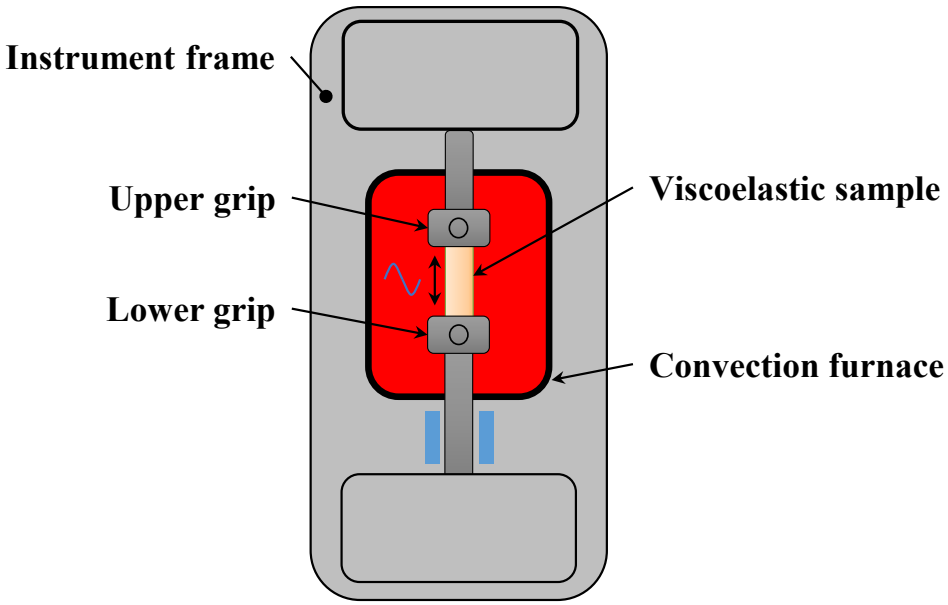

Figure 2.7: Schematic representation of a Dynamic Mechanical Analyzer (DMA). The specimen is held between upper and lower grips and subjected to a sinusoidal stress or strain, typically in tension, compression, bending, or shear. From the phase lag between input and response, the storage modulus (E') and loss modulus (E'') are determined, allowing evaluation of the loss tangent ($\tan\delta = E''/E'$)

Since the frequency range accessible in a single DMA test is limited by instrument constraints, the time-temperature superposition (TTS) principle is applied to extend the characterization over several decades of frequency. This principle relies on the observation that increasing the temperature accelerates the molecular relaxation processes, which is equivalent to observing the same material response at a higher frequency or shorter time scale. Experimental curves of E', E'', or $\tan(\delta)$ obtained at different temperatures are therefore horizontally shifted along the logarithmic frequency axis by a factor a_T, known as the shift factor, until they overlap, forming a continuous master curve referenced to a temperature T_{ref}. The shift factor a_T quantitatively expresses the equivalence between a change in temperature and a corresponding change in time (or frequency) in the viscoelastic

response of the material. Mathematically, the relationship between the relaxation time $\tau(T)$ at a given temperature T and that at the reference temperature T_{ref} can be expressed as:

$$\tau(T) = \frac{\tau(T_{\text{ref}})}{a_T} \tag{2.26}$$

Thus, a_T represents the factor by which the relaxation times (or equivalently, the characteristic frequencies) must be scaled to make the viscoelastic behavior at temperature T coincide with that at T_{ref}. The temperature dependence of a_T can be described empirically. For temperatures above the glass transition T_g, it typically follows the Williams-Landel-Ferry (WLF) equation:

$$\log(a_T) = -\frac{C_1(T - T_{\text{ref}})}{C_2 + (T - T_{\text{ref}})} \tag{2.27}$$

where C_1 and C_2 are empirical constants adjusted to fit the values of the superposition parameter a_T. Below the glass transition temperature T_g, the polymer is in a glassy state, where large-scale chain mobility is essentially frozen. Nevertheless, local segmental motions and secondary relaxation processes can still occur through thermally activated mechanisms. In this temperature regime, the temperature dependence of the shift factor a_T is commonly described by an Arrhenius-type relation:

$$\log(a_T) = \frac{E_a}{R}\left(\frac{1}{T} - \frac{1}{T_{\text{ref}}}\right) \tag{2.28}$$

with E_a the activation energy for molecular motion and R the universal gas constant.

A particularly relevant application of DMA is the thermal ramp test, in which the material is subjected to a sinusoidal deformation of constant amplitude and frequency while the temperature is gradually increased. This procedure allows for the precise identification of the glass transition temperature T_g, corresponding to the transition from the glassy to the rubbery state. The transition manifests itself as a well-defined peak in the loss tangent and represents one of the most important thermomechanical characteristics of polymeric materials.

All the tests described, in particular the DMA and the construction of master curves through the time-temperature superposition principle, are commonly employed for the mechanical characterization of viscoelastic materials. Among the most significant applications is the tire industry, where the viscoelastic response of rubber directly determines key performance parameters such as grip, energy efficiency, and heat dissipation during rolling. The ability to correlate the measured properties as a function of frequency and temperature makes it possible to optimize the material composition and to predict the tread behavior under different operating conditions.

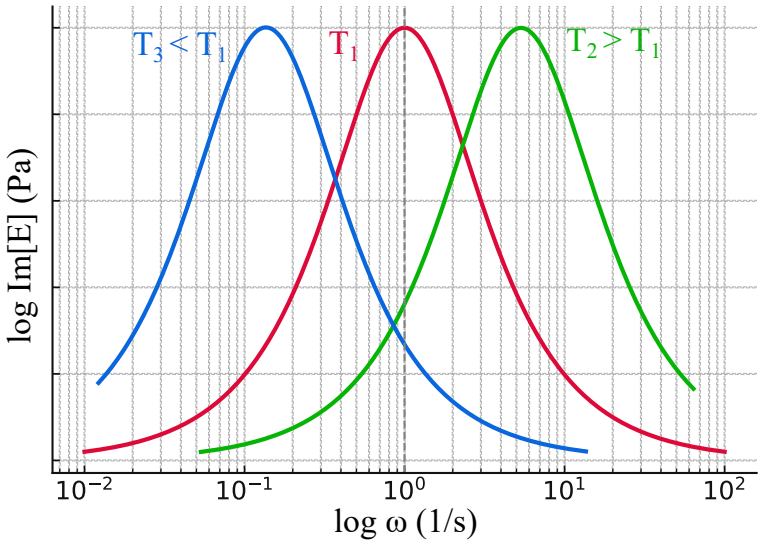

Figure 2.8: Trend of the imaginary part of the complex modulus $E'' = Im\,[E(\omega)]$ as a function of excitation frequency for different temperatures. Increasing temperature results in a shift of the peak toward higher frequencies

2.2 Green's functions methodology in viscoelastic material modeling

2.2.1 The Boundary element method

The solution of partial differential equation (PDE) systems arising in solid mechanics can be approached through various methods. In this work, we adopt the displacement-based formulation, in which the governing equations are reformulated to involve only the displacement vector u as the primary unknown. Although this formulation is widely used due to its direct physical interpretation, the resulting PDE system is often analytically intractable. In such cases, numerical approximation methods become essential. Among these, the Finite Element Method (FEM) and the Boundary Element Method (BEM) are two prominent approaches. The FEM is based on the discretization of the entire domain into finite elements connected at nodes, transforming the PDEs into a system of algebraic equations via a variational (weak) formulation. The unknown field (e.g., displacement) is approximated by interpolating its nodal values within each element. While the FEM is highly versatile and applicable to a wide range of problems, one of its main drawbacks lies in the potentially high computational cost associated with the discretization of the full domain. For a two-dimensional domain discretized with a resolution of N per side, the total number of nodes scales with N^2, leading to increased memory usage and computational time, particularly for large-scale problems. In contrast, the BEM offers a significant reduction in computational complexity by discretizing only the boundary of the domain, thereby reducing the problem size to a number of nodes scaling with $O(N)$ in two dimensions. The

core idea behind BEM is that the solution to a partial differential equation (PDE) can be fully determined by its behavior on the boundary. By approximating the solution on the boundary, one can reconstruct the solution throughout the interior of the domain. This is achieved by reformulating the original PDE as a boundary integral equation, typically involving fundamental solutions, also known as Green's functions, which encapsulate the response of the system to singular sources.

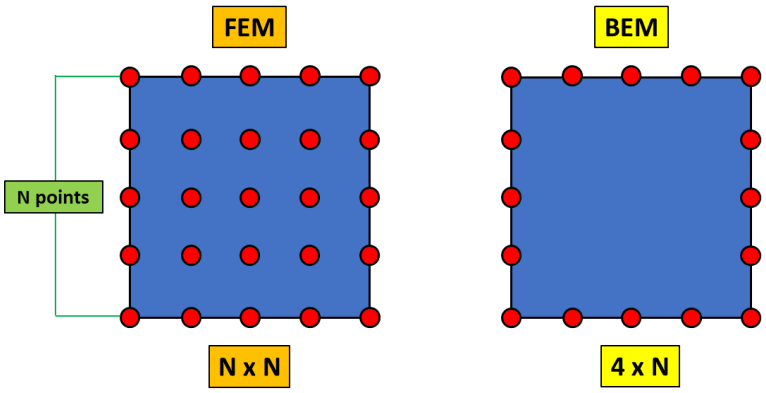

Figure 2.9: Comparison between FEM and BEM mesh discretizations for a square domain. In the Finite Element Method (left), the entire domain is discretized, resulting in N^2 nodes, where N is the number of discretization points per edge. In the Boundary Element Method (right), only the boundary is discretized, yielding $4N$ nodes for a square geometry

The BEM is particularly effective for problems governed by linear differential operators, such as those encountered in linear elasticity or viscoelasticity, where the superposition principle holds. As a simple example, consider a beam subjected to concentrated transverse forces. If a force F_1 is applied at a point ξ_1, it induces a displacement $u_1(x)$ at a generic point x. Similarly, a second force F_2 applied at ξ_2 results in a displacement $u_2(x)$. For a linear system, the combined application of F_1 and F_2 leads to a total displacement at x given by $u(x) = u_1(x) + u_2(x)$.

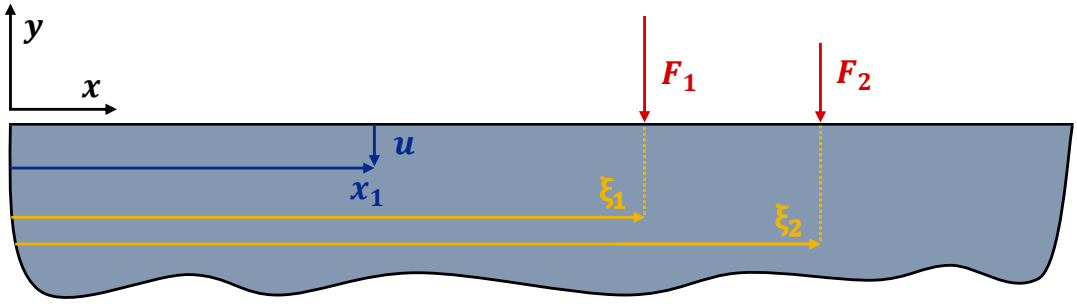

Figure 2.10: Beam subjected to two transverse concentrated loads applied at points ξ_1 and ξ_2, respectively. The resulting displacement u at the observation point x_1 is given by the linear combination of the individual contributions generated by each applied force

This additive property allows for the use of Green's functions $G(x, \xi)$, representing

the displacement at point x due to a unit load applied at ξ. The displacement field generated by multiple point loads can thus be expressed as:

$$u(x) = \sum_{i=1}^{n} G(x, \xi_i) F(\xi_i) \tag{2.29}$$

where n is the number of point loads. This expression can be further generalized to continuous distributions of stress $\sigma(\xi)$ over the boundary of the domain:

$$u(x) = \int G(x, \xi) \sigma(\xi) \, d\xi \tag{2.30}$$

Then if the system is translationally invariant the Green's function depends only on the distance between the coordinates, i.e. $G(x, \xi) = G(x - \xi)$, and the integral reduces to a convolution product:

$$u(x) = \int G(x - \xi) \sigma(\xi) \, d\xi \tag{2.31}$$

In this case the Green's function can be interpreted as the response of the system to a Dirac delta distribution of force applied at point ξ_0. Indeed, if we define $\sigma(\xi) = \delta(\xi_0)$, where δ is the Dirac delta function, then the integral becomes:

$$u(x) = \int G(x - \xi) \delta(\xi_0) \, d\xi = G(\xi_0) \tag{2.32}$$

This powerful concept allows the BEM to compute the response of the system from boundary data alone, provided the Green's function for the problem is known. However, this approach is not universally applicable. The derivation of boundary integral equations relies on the existence of a fundamental solution, which is generally available only for linear, homogeneous, and isotropic media. Consequently, the BEM is limited to problems where linearity and the superposition principle hold. In the presence of material nonlinearity, large deformations, or inhomogeneities, the BEM loses its efficiency or becomes inapplicable, and more general methods such as FEM must be employed. In the present work, since our focus lies on the study of linear viscoelasticity, a regime in which the governing equations remain linear and the superposition principle is valid, the use of the BEM is not only appropriate but also particularly advantageous from both a theoretical and computational standpoint.

2.2.2 Boundary element method applied to general unsteady viscoelastic problems

Building upon the principles discussed in the previous section, the application of the Boundary Element Method can be naturally extended to linear viscoelastic problems under unsteady time-dependent loading conditions. Let us consider the case of a homogeneous, isotropic, linear viscoelastic half-space, subject to time-varying normal stresses applied on its surface. Due to translational invariance and

linearity, the displacement field $u(\mathbf{x}, t)$ in response to a spatially and temporally varying normal stress field $\sigma(\mathbf{x}, t)$ can be written as a space-time convolution with the corresponding viscoelastic Green's function $G(\mathbf{x}, t)$:

$$u\left(\mathbf{x}, t\right) = \int d^2x_1 dt_1 G\left(\mathbf{x} - \mathbf{x}_1, t - t_1\right) \sigma\left(\mathbf{x}_1, t_1\right) \tag{2.33}$$

where $\mathbf{x}$ is the in-plane position vector. Applying a Fourier transform in both space and time, the convolution simplifies into a pointwise multiplication in the frequency-wavenumber domain:

$$u\left(\mathbf{q}, \omega\right) = G\left(\mathbf{q}, \omega\right) \sigma\left(\mathbf{q}, \omega\right) \tag{2.34}$$

where $\mathbf{q}$ denotes the spatial wave vector and ω the angular frequency, while $G(\mathbf{q}, \omega)$ is the response function in the frequency domain. The specific form of $G(\mathbf{q}, \omega)$ depends on the geometry, material rheology and boundary constraints on the system. Dimensional and analytical arguments (see Ref. [53]) show that this function takes the form:

$$G\left(\mathbf{q},\omega\right) = -\frac{2\left(1-\nu^2\right)}{E\left(\omega\right)} \frac{1}{|\mathbf{q}|} S\left(|\mathbf{q}|, \omega\right) \tag{2.35}$$

In Eq. 2.35, $E(\omega)$ is the complex modulus in the frequency domain, ν is Poisson's ratio (assumed frequency-independent) and $S(|\mathbf{q}|, \omega)$ is a correction factor introduced to account for deviations from the ideal half-space solution. Indeed, for a simple half-space $S = 1$, but more complex configurations may yield non-trivial S functions. The correction factor $S\left(\mathbf{q}, \omega\right)$ has been derived for a variety of system configurations, including different geometries and boundary conditions (see Ref. [53–56]). The form of Eq. 2.35 is a direct consequence of the elastic-viscoelastic correspondence principle (Ref. [57]), which asserts that the governing equations of linear viscoelasticity in the frequency domain retain a structure formally analogous to their elastic counterparts, provided the geometry and the region where boundary conditions are applied remain unchanged over time. This allows the viscoelastic Green's function to be obtained from its elastic analogue by replacing the elastic modulus with its frequency-dependent counterpart. In particular, when the correction factor S is independent of ω (as occurs in confined or free layer configurations), the Green's function in the time domain can be factorized into a product of a time-dependent and a space-dependent functions:

$$G(\mathbf{x}, t) = \dot{J}(t)\mathcal{G}(\mathbf{x}) \tag{2.36}$$

where:

$$\mathcal{G}(\mathbf{x}) = -\frac{2\left(1-\nu^2\right)}{\left(2\pi\right)^2} \int dq^2 \frac{S\left(qd\right)}{|q|} e^{i\mathbf{q}\cdot\mathbf{x}} \tag{2.37}$$

and $J(t)$ is the viscoelastic creep function. It is worth noting that, in accordance with the elastic-viscoelastic correspondence principle, $\mathcal{G}(\mathbf{x})$ corresponds to the Green's function of the associated elastic problem, assuming a unit elastic modulus. For instance, in the case of an elastic half-space, this yields $\mathcal{G}(\mathbf{x}) = 2\left(1-\nu^2\right) / |\mathbf{x}|$,

which is consistent with the classical Boussinesq solution. Substituting Eq. 2.36 into Eq. 2.33, the displacement field can be written as:

$$u\left(\mathbf{x},t\right)=\int_{-\infty}^{t}dt_1 J(t-t_1)\int d^2x_1\mathcal{G}(\mathbf{x}-\mathbf{x}_1)\dot{\sigma}\left(\mathbf{x}_1,t_1\right) \tag{2.38}$$

Alternatively, the expression can be reformulated via integration by parts, yielding:

$$u(\mathbf{x},t)=J(0^+)\int d^2x_1\,\mathcal{G}(\mathbf{x}-\mathbf{x}_1)\,\sigma(\mathbf{x}_1,t)+\int_{-\infty}^{t}dt_1\,\dot{J}(t-t_1)\int d^2x_1\,\mathcal{G}(\mathbf{x}-\mathbf{x}_1)\,\sigma(\mathbf{x}_1,t_1) \tag{2.39}$$

2.2.3 Steady-state response in 1D+1D periodic contact conditions

In the subsequent chapters, we shall consider the case of a 1D+1D periodic contact in steady-state sliding conditions, characterized by a fundamental spatial wavelength λ_0. Consequently, it becomes necessary to adapt the equations derived in the preceding section to this particular framework. Let us begin our analysis by considering the purely elastic case, which serves as a reference point for the development of the viscoelastic formulation. As introduced in [55], we define the quantity $v(x)$ as the surface profile measured with respect to the mean line of the deformed viscoelastic body. This displacement field can be related to the interfacial stress distribution $\sigma(x)$ through the equation:

$$v(x)=\int_{-\lambda_0/2}^{\lambda_0/2}dx_1\frac{\mathcal{G}_E(x-x_1)}{E}\sigma(x_1) \tag{2.40}$$

where E is the Young's modulus of the material and $\mathcal{G}_E(x)$ denotes the elastic Green's function corresponding to the specific contact configuration considered:

$$\mathcal{G}_E(x)=\frac{2\left(1-\nu^2\right)}{\pi}\left(\sqrt{\log[2-2\cos(q_0x)]}+\sum_{m=1}^{\infty}A_m(q_0d)\frac{\cos(mq_0x)}{m}\right) \tag{2.41}$$

with $q_0=2\pi/\lambda_0$, d denoting the thickness of the deformable material and $A_m(q_0d)$ representing a term that depends on the boundary conditions of the system. To clarify this concept, it is useful to examine two representative case studies. These configurations are illustrated in Fig. 2.11 and are described as follows. In the first case Fig. 2.11(a), a deformable slab of thickness d confined between a rigid upper plate and a rough lower substrate. In the second Fig. 2.11(b), the same slab is subjected to a uniformly applied pressure on its upper surface.

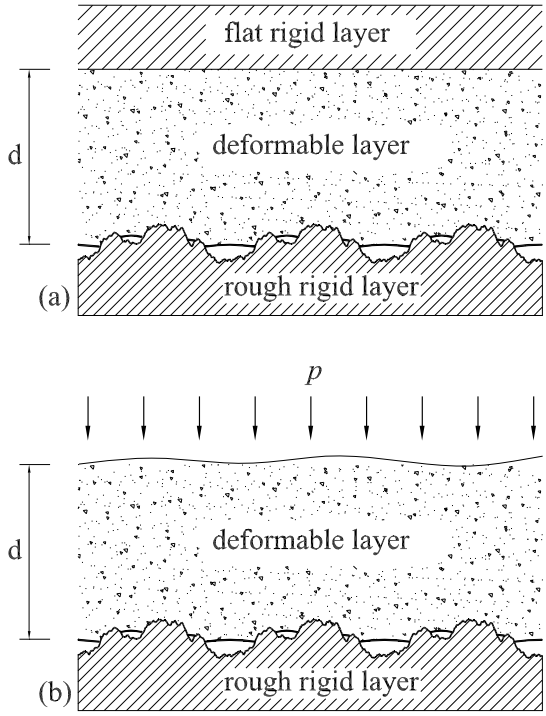

Figure 2.11: A deformable layer of thickness d in contact with a rough substrate. In case (a), the layer is bonded to the upper plate, while in case (b), it is subjected to a uniform pressure p

In these two cases, the coefficient $A_m(q_0 d)$ takes the following forms:

$$A_m(q_0 d) = \frac{2mq_0 d - (3-4\nu)\sinh(2dmq_0)}{5 + 2\left(mq_0 d\right)^2 - 4\nu\left(3-2\nu\right) + (3-4\nu)\cosh\left(2mq_0 d\right)} + 1 \tag{2.42}$$

for the confined layer, and

$$A_m(q_0 d) = \frac{2mq_0 d + \sinh(2dmq_0)}{1 + 2\left(mq_0 d\right)^2 - \cosh\left(2mq_0 d\right)} + 1 \tag{2.43}$$

for the free layer. It is worth noting that the series $\sum_{m=1}^{\infty} A_m(q_0 d)\frac{\cos(mq_0 x)}{m}$ is rapidly converging and tends to zero in the limit of an elastic half-space, i.e., as $d \to \infty$. Furthermore, the mean surface displacement u_{m} can be expressed in terms of the average interfacial stress $\sigma_m = \frac{1}{\lambda_0}\int_{-\lambda_0/2}^{\lambda_0/2}\sigma(x)\,dx$ as:

$$u_{\mathrm{m}} = -\frac{1+\nu}{1-\nu}\frac{1-2\nu}{E}\sigma_m d \tag{2.44}$$

It should be noted that, in the special case of an incompressible material, i.e., when the Poisson ratio $\nu = 0.5$, the mean displacement u_{m} vanishes identically. Then, by applying linearity, translational invariance and the elastic-viscoelastic correspondence principle, the elastic solution is extended to the viscoelastic steady-state regime, allowing the derivation of the corresponding viscoelastic Green's

function:

$$v\left(x,t\right)=\int_{-\infty}^{t}dt_1J(t-t_1)\int_{-\lambda_0/2}^{\lambda_0/2}dx_1\mathcal{G}_E(x-x_1)\dot{\sigma}\left(x_1,t_1\right) \tag{2.45}$$

Assuming steady-state sliding at velocity V, the displacement and stress fields depend on the composed variable $x-Vt$. By shifting to a reference frame moving at velocity V via the substitution $x\rightarrow x+Vt$, the equation (2.45) can be equivalently rewritten as:

$$v\left(x\right)=\int_{-\lambda_0/2}^{\lambda_0/2}dx_1\mathcal{G}_V^{1D}(x-x_1)\sigma\left(x_1\right) \tag{2.46}$$

where $\mathcal{G}_V^{1D}(x)$ is the viscoelastic Green's function for steady-state sliding periodic contacts, parametrically depending on the sliding velocity:

$$\mathcal{G}_V^{1D}(x)=J(0^+)\mathcal{G}_E(x)+\int_{0^+}^{+\infty}dt\mathcal{G}_E(x+Vt)\dot{J}(t) \tag{2.47}$$

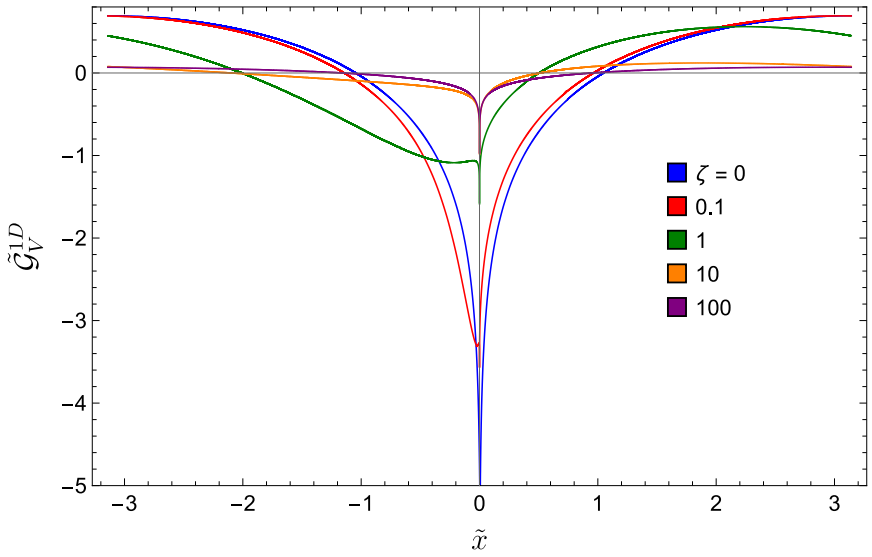

Figure 2.12: The dimensionless periodic Green's function $\tilde{\mathcal{G}}_V^{1D}(x)=\mathcal{G}_V^{1D}(x)\frac{\pi E_0}{2(1-\nu^2)}$ as a function of the dimensionless coordinate $\tilde{x}=q_0x$, assuming steady-state conditions. The dependence on the dimensionless sliding velocity $\zeta=q_0V\tau$ is examined for a viscoelastic material with modulus ratio $E_\infty/E_0=10$

The resulting function characterizes the periodic steady-state displacement response during sliding contact. This is illustrated in Fig. 2.12, which displays the dimensionless Green's function:

$$\tilde{\mathcal{G}}_V^{1D}(x)=\mathcal{G}_V^{1D}(x)\frac{\pi E_0}{2\left(1-\nu^2\right)} \tag{2.48}$$

as a function of the dimensionless coordinate $\tilde{x} = q_0 x$, for different values of $\zeta = kV\tau$, assuming a single-relaxation creep function:

$$J(t) = \left[\frac{1}{E_\infty} + \left(\frac{1}{E_0} - \frac{1}{E_\infty}\right)(1 - e^{-t/\tau})\right] H(t), \tag{2.49}$$

with modulus ratio $E_\infty/E_0 = 10$. By examining the figure, it can be observed that in the low-velocity regime the material has sufficient time to relax, resulting in a viscoelastic response governed by $\mathcal{G}_V^{1D} = \mathcal{G}_E/E_0$. As the sliding velocity increases, the available time for relaxation decreases and the response transitions toward the unrelaxed limit, $\mathcal{G}_V^{1D} = \mathcal{G}_E/E_\infty$. For intermediate values of the dimensionless parameter ζ, the system exhibits asymmetric viscoelastic profiles, which reflect the interplay between the rate of deformation and the intrinsic relaxation dynamics of the material, giving rise to non-symmetric stress and displacement distributions.

Chapter 3

Theoretical models in rough contact mechanics

The contact between bodies in presence of surface roughness is a highly relevant research area, since the accurate prediction of the physical quantities involved remains an open challenge. In elastic conditions and for small deformations, most theoretical models predict a linear growth of the effective contact area with increasing applied load, until reaching a plateau that eventually leads to full -contact. This behaviour reflects the idea that, initially, the number of asperities actually involved in contact increases proportionally to the force exerted, while at higher loads the interface tends to become progressively saturated, reducing the possibility of generating new real contact area. However, these models remain largely idealised and are not always able to accurately describe the complexity of real surfaces, whose roughness is distributed over multiple scales and has a decisive influence on contact properties. There is therefore still ample scope for research to develop more refined theoretical and numerical approaches capable of capturing the multiscale nature of the problem and providing more reliable predictions even in concrete application scenarios. This chapter will analyse the main models used in the study of elastic contact between rough surfaces. The first chapter will introduce the main statistical and spectral quantities used to describe rough surfaces and profiles, providing the conceptual basis necessary for further development. Next, the classical theory of Greenwood and Williamson will be discussed, together with some derived models, which describe rough contact as an superposition of contributions due to individual independent asperities. Finally, Persson's theory will be examined, which, thanks to its multiscale approach, represented a significant advance over previous models, allowing for a more realistic understanding of the complexity of natural and technical surfaces. The study of these models is not only of theoretical interest, but also has important practical implications in numerous application areas, such as the design of mechanical components subject to wear, the reliability of electrical contacts, the adhesion of coatings and, more generally, the optimisation of the tribological performance of materials and interfaces.

3.1 Statistical and spectral characterisation of roughness

When analysing the surfaces of two solids in contact, the nominal contact area A_0, which at a macroscopic level appears to be the region actually involved in the interaction, never corresponds to the real area of contact. This is because each material has a certain degree of roughness: contact occurs only at the summit points of the surface irregularities, while the areas corresponding to the valleys remain excluded. If we consider a section of the surface, i.e. a profile, the latter is also characterised by peaks and valleys. It is important to note that the properties of the profile do not necessarily coincide with those of the two-dimensional surface, which may have different geometric characteristics. In general, a rough surface can be described based on the distribution of heights with respect to a reference plane and the radius of curvature of the asperities. However, the characterisation of such surfaces is not trivial, since the parameters that characterise them depend on the level of detail with which they are measured, i.e. on the chosen sampling interval. Furthermore, in many cases the surface exhibits fractal-like properties, characterized by internal self-similarity in which the shape repeats itself on different scales, so that enlarging a portion of it produces a configuration similar to the original one.

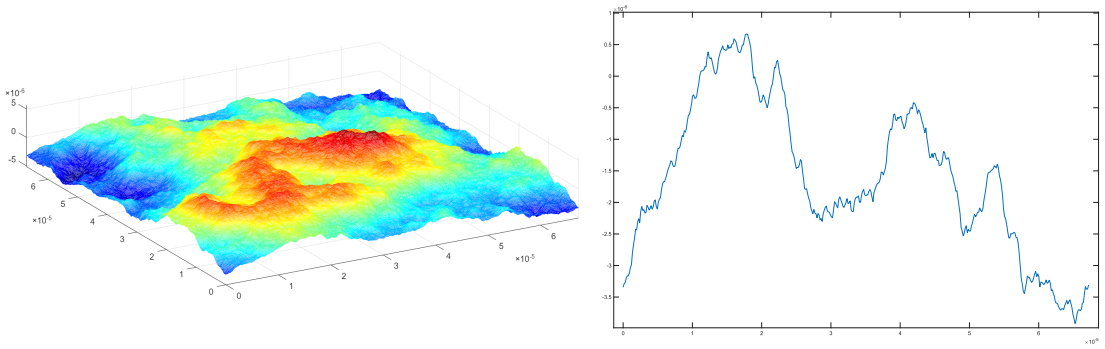

Figure 3.1: Example of a generated self-affine fractal surface and its corresponding cross-sectional profile

To describe quantitatively the surface roughness, it is necessary to introduce some basic statistical quantities. Consider a two-dimensional surface with area A, described by the height function $f(\mathbf{x})$ with $\mathbf{x} = (x, y)$. The mean plane is defined as the mean value of the function $f(\mathbf{x})$ over the area A:

$$\bar{f} = \frac{1}{A} \int_A f(\mathbf{x})\, d^2x \tag{3.1}$$

The deviation from the mean plane is therefore obtained as the difference between the local height and the mean plane:

$$r(\mathbf{x}) = f(\mathbf{x}) - \bar{f} \tag{3.2}$$

To quantitatively characterise the roughness of a surface, a first fundamental measurement is the mean square roughness, which represents the mean square deviation of the height from the mean plane:

$$r_{rms}^2 = \frac{1}{A}\int_A r(\mathbf{x})^2\, d^2x \tag{3.3}$$

Another widely used measure is the arithmetic mean roughness, which describes the average absolute deviation of the height:

$$r_a = \frac{1}{A}\int_A |r(\mathbf{x})|\, d^2x \tag{3.4}$$

Both of these quantities can also be expressed in terms of the probability distribution of heights $\varphi(r)$. In this case, they correspond respectively to the second moment and the absolute mean value of the random variable r:

$$r_{rms}^2 = \int_{-\infty}^{\infty} r^2\, \varphi(r)\, dr = \langle r^2 \rangle \qquad r_a = \int_{-\infty}^{\infty} |r|\, \varphi(r)\, dr = \langle |r| \rangle \tag{3.5}$$

The two forms of writing, spatial and probabilistic, are equivalent in cases where the surface can be considered stationary, i.e. when its statistical properties do not depend on position. More generally, the central moments of the height distribution are defined as:

$$\langle r^p \rangle = \int_{-\infty}^{\infty} r^p\, \varphi(r)\, dr \tag{3.6}$$

For example, the third central moment, known as skewness, measures the asymmetry of the distribution of heights, while the fourth, kurtosis, provides information on the degree of concentration of values around the mean. Similarly, if the analysis is conducted on a one-dimensional profile of length L, the expressions introduced are rewritten by replacing the two-dimensional integral over the area A with the one-dimensional integral along the profile, extended over the interval $[0, L]$. The concepts of expected value and variance introduced above can be extended to the summits of the surface, defining the mean height $\langle z \rangle$ and the variance σ_z^2. In 1966, Greenwood and Williamson [58] experimentally proved that, for a wide range of engineering surfaces, the distributions of both local heights r and peak heights z, in both one-dimensional profiles and two-dimensional surfaces, can be well approximated by Gaussian distributions.
To describe the horizontal spatial distribution of the heights of a rough surface, the autocorrelation function is introduced, which in general form for a two-dimensional surface can be defined as:

$$R(\mathbf{x}_1, \mathbf{x}_2) = \langle r(\mathbf{x}_1) r(\mathbf{x}_2) \rangle \tag{3.7}$$

where $\langle \cdot \rangle$ indicates the expected value over the set of all possible realisations of the surface. If the surface can be considered stationary, the statistical properties are independent of the absolute position and the autocorrelation function depends solely on the relative displacement vector $\boldsymbol{\xi}$:

$$R(\boldsymbol{\xi}) = \langle r(\mathbf{x}) r(\mathbf{x} + \boldsymbol{\xi}) \rangle \tag{3.8}$$

Furthermore, if the process is ergodic, the averages calculated on the set of realisations can be replaced by spatial averages on a single sufficiently extended realisation:

$$R(\boldsymbol{\xi}) = \lim_{A\to\infty} \frac{1}{A} \int_A r(\mathbf{x})\, r(\mathbf{x}+\boldsymbol{\xi})\, d^2x \tag{3.9}$$

Starting from the autocorrelation function, the surface can be analysed in the frequency domain using the power spectral density (PSD), defined as the Fourier transform of the autocorrelation function. The PSD provides a description of the spatial distribution of the surface energy across different roughness scales:

$$C(\mathbf{q}) = \frac{1}{(2\pi)^n} \int \langle r(\mathbf{0})\, r(\mathbf{x})\rangle\, e^{-i\mathbf{q}\cdot\mathbf{x}}\, d^2x \tag{3.10}$$

where n represents the dimensionality of the problem ($n = 1$ for a one-dimensional profile, $n = 2$ for a surface). From knowledge of the PSD, it is possible to define spectral moments of order p as:

$$m_p = \int C(\mathbf{q})|\mathbf{q}|^p\, d^2q \tag{3.11}$$

which provide a compact way of characterising topography, as they condense information relating to height, slope and curvature of roughness into a few parameters. For example, it can be shown that the zero-order spectrum coincides with the mean quadratic roughness of the surface:

$$m_0 = \int C(\mathbf{q})\, d^2q = \langle r^2\rangle = r_{rms}^2 \tag{3.12}$$

If we denote the wavelength of a sinusoidal wave by λ, $\mathbf{q}$ is a wave vector such that:

$$q = |\mathbf{q}| = \frac{2\pi}{\lambda} \tag{3.13}$$

In the case of an isotropic surface, it is possible to perform a radial averaging of the two-dimensional PSD, obtaining a one-dimensional function $C(q)$ dependent only on the modulus q of the wave vector. For self-affine fractal surfaces, the PSD typically exhibits power-law behaviour in a wavevector range between a lower cut-off q_0 and an upper cut-off q_1:

$$C(q) \propto q^{-\beta} \qquad \text{for } q_0 < q < q_1 \tag{3.14}$$

where the exponent β is related to the Hurst exponent H and the domain size n via:

$$\beta = 2H + n \tag{3.15}$$

In a double logarithmic representation, this dependence manifests itself as a straight line with a negative slope. The Hurst exponent H controls the spatial correlation and aspect ratio of the peaks, as low values of H describe sharp and irregular roughness, while higher values correspond to flatter roughness and more regular

surfaces on a small scale, and is connected to the fractal dimension of the surface D_f by the relationship:

$$D_f = n + 1 - H \tag{3.16}$$

The parameters q_0 and q_1 represent, respectively, the lower limit (roll-off wavevector, associated with the maximum characteristic wavelength) and the upper limit (microscopic cut-off, typically close to the atomic scale). When the surface has a finite lateral dimension L, there is an additional natural lower limit:

$$q_L = \frac{2\pi}{L} \tag{3.17}$$

which represents the smallest accessible wavevector. In practice, for surfaces with well-defined roll-off, we can set $q_0 \simeq q_L$. Nayak [59] also demonstrated that, for random isotropic surfaces with Gaussian height distribution, all statistical properties of the topography are entirely contained in the PSD. In this case, switching to polar coordinates, we have $d^2q = S_{n-1}q^{n-1}dq$, where:

$$S_{n-1} = \frac{2\pi^{n/2}}{\Gamma(n/2)} \qquad \Gamma(y) = \int_0^\infty t^{y-1}\, e^{-t} dt \tag{3.18}$$

and therefore equation (3.11) of the spectral moments can be rewritten as:

$$m_p = \frac{2\pi^{n/2}}{\Gamma(n/2)} \int_0^\infty C(q)\, q^{p+n-1} dq \tag{3.19}$$

3.2 Greenwood and Williamson based contact models

One of the most famous and basic models for studying the contact between rough surfaces is the one proposed by Greenwood and Williamson in 1966 [58]. In such a model, the rough surface is represented as being uniformly covered with spherical asperities, all having the same radius of curvature R but randomly distributed in height (an illustrative scheme is shown in Figure 3.2). It is assumed that the contact between each roughness and the deformable flat surface occurs according to Hertz's theory (see section 1.1) and that the deformations of the asperities are independent of each other, so that the real contact area A remains much smaller than the nominal area A_0. Let us therefore consider the contact between a deformable plane and a rigid indenter characterised by roughness of amplitude r_{rms} and reduced modulus E^*. Let z be the height of the peaks measured with respect to their mean plane, and d the separation between the deformable plane and the mean plane of the peaks. The asperities with height $z > d$ are elastically compressed by an amount $\delta = z - d$.

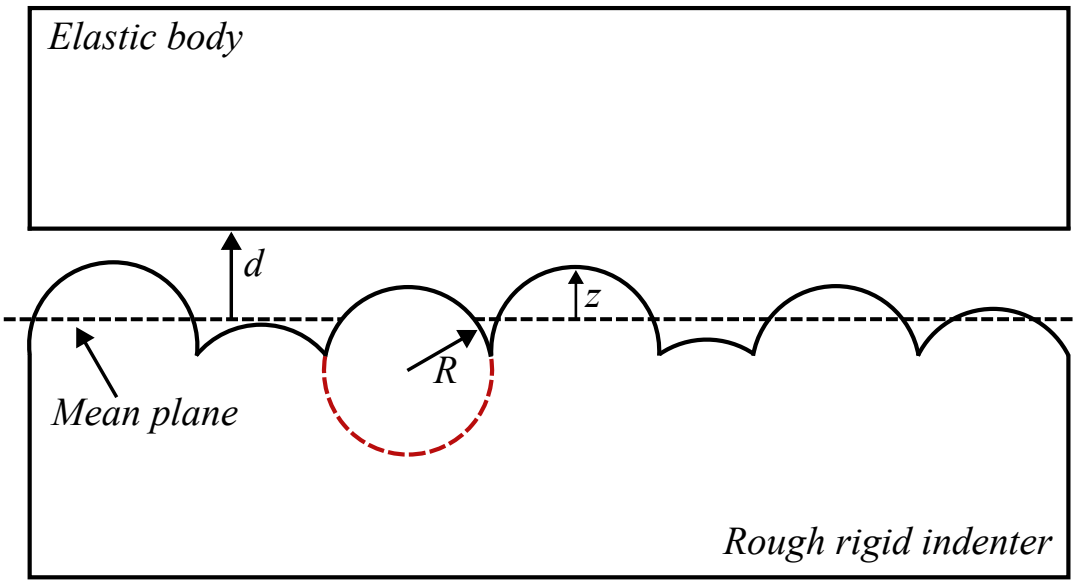

Figure 3.2: Schematic representation of the rough surface as considered in Greenwood and Williamson's contact model, with the roughness of the rigid surface modelled as a set of spherical asperities of equal radius R.

As the load increases, the penetration of the surface increases and hence the number of peaks that come into Hertzian contact with the plane increases. If D_s represents the surface density of peaks per unit area, the number N of asperities in contact when the separation is d is expressed as:

$$\frac{N}{A_0} = D_s \int_d^\infty \varphi_s(z) dz \tag{3.20}$$

Since each contact is described by Hertz's theory, the real contact area A and the total load P are given by:

$$\frac{A}{A_0} = D_s \int_d^\infty A_i \varphi_s(z) dz \tag{3.21}$$

$$\frac{P}{A_0} = D_s \int_d^\infty P_i \varphi_s(z) dz \tag{3.22}$$

where A_i and P_i represent the contact area and the load of the single asperity, respectively. For Hertzian contact between a sphere and a plane, the following relationships apply:

$$A_i = \pi R \delta_i = \pi R (z_i - d) \tag{3.23}$$

$$P_i = \frac{4}{3} E^* \sqrt{R \delta_i^3} = \frac{4}{3} E^* \sqrt{R (z_i - d)^3} \tag{3.24}$$

It is also assumed that the distribution of heights z of the summits follows a Gaussian law with standard deviation σ_s, such that:

$$\varphi_s = \frac{1}{\sigma_s \sqrt{2\pi}} \exp\left(-\frac{z^2}{2\sigma_s^2}\right) \tag{3.25}$$

By introducing the dimensionless variable $\mathcal{X} = z/\sigma_s$ and the dimensionless separation $d^* = d/\sigma_s$, the above equations can be rewritten as:

$$\begin{aligned}
\frac{N}{A_0} &= \frac{D_s}{\sqrt{2\pi}} \int_{d^*}^{\infty} \exp\left(-\frac{\mathcal{X}^2}{2}\right) d\mathcal{X} \\
\frac{A}{A_0} &= \frac{D_s \pi R \sigma_s}{\sqrt{2\pi}} \int_{d^*}^{\infty} (\mathcal{X} - d^*) \exp\left(-\frac{\mathcal{X}^2}{2}\right) d\mathcal{X} \\
\frac{P}{A_0} &= \frac{4 D_s E^* \sqrt{R\sigma_s^3}}{3\sqrt{2\pi}} \int_{d^*}^{\infty} (\mathcal{X} - d^*)^{3/2} \exp\left(-\frac{\mathcal{X}^2}{2}\right) d\mathcal{X}
\end{aligned} \tag{3.26}$$

It has been experimentally verified that the parameters D_s, R and σ_s are not completely independent, but follow an empirical relationship reported by Archard [60], according to which:

$$0.03 < \sigma_s R D_s < 0.05 \tag{3.27}$$

The Greenwood and Williamson model can be extended to the adhesive case using the Fuller and Tabor model [61], which describes roughness as JKR-type adhesive spherical contacts (see section 1.4). In this case, the equations of the JKR theory replace Hertz's laws (3.23) and (3.24), and the calculation procedure during the loading phase remains similar to that of the original model. During unloading, however, the situation is more complex: the higher asperities remain compressed while the lower ones are stretched, forming adhesive necks that break when their deformation exceeds the imposed displacement stability limit (eq. 1.47). This critical condition is expressed by:

$$\delta_c = \left(\frac{27\pi^2 \Delta\gamma^2 R}{64 E^{*2}}\right)^{1/3} \tag{3.28}$$

For this reason, during the unloading phase, the lower limits of the integrations in equations (3.20), (3.21) and (3.22) must be changed to $d - \delta_c$. A further theoretical advancement was proposed by Greenwood in 2006 [62], as a simplification of the more general model by Bush, Gibson and Thomas (BGT) [63]. In the BGT model, the surface is described as a set of ellipsoidal asperities with a Gaussian distribution of heights and variable curvatures determined by the spectral density of roughness and the associated statistical moments. Greenwood simplifies the problem by treating Hertzian elliptical contacts as equivalent spherical contacts, assuming that the equivalent radius of curvature is related to the Gaussian curvature of the vertices according to:

$$\frac{1}{R} = \mathcal{K}_g = \sqrt{\mathcal{K}_1 \mathcal{K}_2} \tag{3.29}$$

where $\mathcal{K}_1$ and $\mathcal{K}_2$ are the main curvatures.
Introducing the variable $\chi = (\mathcal{K}_1 - \mathcal{K}_2)/2$, the real contact area and load are written as:

$$\frac{A}{A_0} = \int_d^{\infty} \int_0^{\infty} A_i \psi_s(z, \mathcal{K}_g)\, dz\, d\mathcal{K}_g \tag{3.30}$$

$$\frac{P}{A_0} = \int_d^{\infty} \int_0^{\infty} A_i \sigma_m \psi_s(z, \mathcal{K}_g)\, dz\, d\mathcal{K}_g \tag{3.31}$$

where σ_m is the mean contact pressure and $\psi_s(z, \mathcal{K}_g)$ is the joint density per unit area of the summits having height z and Gaussian curvature $\mathcal{K}_g$. This density is obtained as:

$$\psi_s(z, \mathcal{K}_g) = \int_{-\infty}^{\infty} \frac{2\mathcal{K}_g}{(\mathcal{K}_g^2 + \chi^2)^{1/2}} \Upsilon(z, \mathcal{K}_1, \mathcal{K}_2)\, d\chi \tag{3.32}$$

$\Upsilon(z, \mathcal{K}_1, \mathcal{K}_2)$ is the the joint probability distribution per unit area of summits heights and summits curvatures. Defining the quantities $\alpha = m_0 m_4 / m_2^2$, $\mathcal{C} = \alpha/(2\alpha - 3)$ and using the definition of spectral moments of the PSD in equation 3.19, for an isotropic surface we obtain:

$$\begin{aligned}\Upsilon(z, \mathcal{K}_1, \mathcal{K}_2) =& \frac{\sqrt{27}}{(4\pi)^2} \frac{1}{m_2 m_4 \sqrt{m_0 m_4}} \mathcal{C}_1^{1/2} \exp\left[-\mathcal{C}_1 \left(\frac{z}{\sqrt{m_0}} + \frac{3}{2\sqrt{\alpha}} \frac{\mathcal{K}_1 + \mathcal{K}_2}{2\sqrt{m_4}}\right)^2\right] \\ & \times |\mathcal{K}_1 - \mathcal{K}_2| \mathcal{K}_1 \mathcal{K}_2 \exp\left\{-\frac{3}{16 m_4}\left[3\left(\mathcal{K}_1 + \mathcal{K}_2\right)^2 - 8\mathcal{K}_1\mathcal{K}_2\right]\right\}\end{aligned} \tag{3.33}$$

This approach provides more accurate expressions of real area and load than the original Greenwood and Williamson model, as it takes into account not only the height distribution of roughness, but also the actual variability of their curvatures. This allows for a more realistic description of the mechanics of contact between surfaces with complex roughness spectra, thus bringing theoretical predictions closer to experimental results.

3.3 Persson theory of rough surface contact

In 2001, Persson [64] developed one of the most established models to date for the study of elastic contact between rough surfaces in the absence of adhesion, with particular reference to self-affine fractal surfaces, but also extendable to arbitrary random surface roughness. Unlike multi-asperity models (GW, BGT), Persson's theory does not describe contact as the sum of discrete contributions from independent asperities, but rather as a statistical evolution of the pressure distribution as the observation scale varies. The theory assumes that, in the case of full contact, the power spectral density (PSD) of the deformed elastic surface coincides with that of the rigid rough surface. Under this condition, the solution is exact. For partial contact, the description is modified by imposing that the probability distribution of local pressures vanishes at zero pressure ($\sigma = 0$). Consider an elastic half-space in contact with a rigid rough indenter of lateral dimension L. The surface is observed at a certain magnification defined by the scale factor $\zeta = q/q_L = L/\lambda$, and let $p(\sigma, \zeta)$ be the probability of having a local pressure σ at the interface at magnification ζ. Assuming full contact and a Gaussian surface, Persson shows that the function $p(\sigma, \zeta)$ satisfies a diffusion-type equation:

$$\frac{\partial p(\sigma, \zeta)}{\partial \zeta} = f(\zeta) \frac{\partial^2 p(\sigma, \zeta)}{\partial \sigma^2} \tag{3.34}$$

Defining the mean pressure acting on the solid in contact as $\sigma_m = P/A_0$, in equation 3.34 the term $f(\zeta)$ is:

$$f(\zeta) = \frac{dG(\zeta)}{d\zeta}\sigma_m^2 \tag{3.35}$$

where $G(\zeta)$ is the cumulative variance of pressure fluctuations at magnification level ζ:

$$G(\zeta) = \frac{\pi E^{*2}}{4\sigma_m^2}\int_{q_L}^{\zeta q_L} q^3 C(q) dq \tag{3.36}$$

This term increases with magnification and regulates the broadening of the pressure distribution. Substituting the definition of $G(\zeta)$ in equation 3.35, it follows that:

$$f(\zeta) = \frac{\pi}{4}E^{*2} q_L q^3 C(q) \tag{3.37}$$

In order to solve the equation 3.34 we need some additional condition. The initial condition of the system comes from the observation that, on a macroscopic scale, the elastic half-space appears to be in contact everywhere with the rigid surface and the stress state is uniform with a value equal to the mean pressure σ_m. In this situation, the probability distribution $p(\sigma, \zeta)$ takes the form of a Dirac delta function centred at σ_m:

$$p(\sigma, 1) = \delta(\sigma - \sigma_m) \tag{3.38}$$

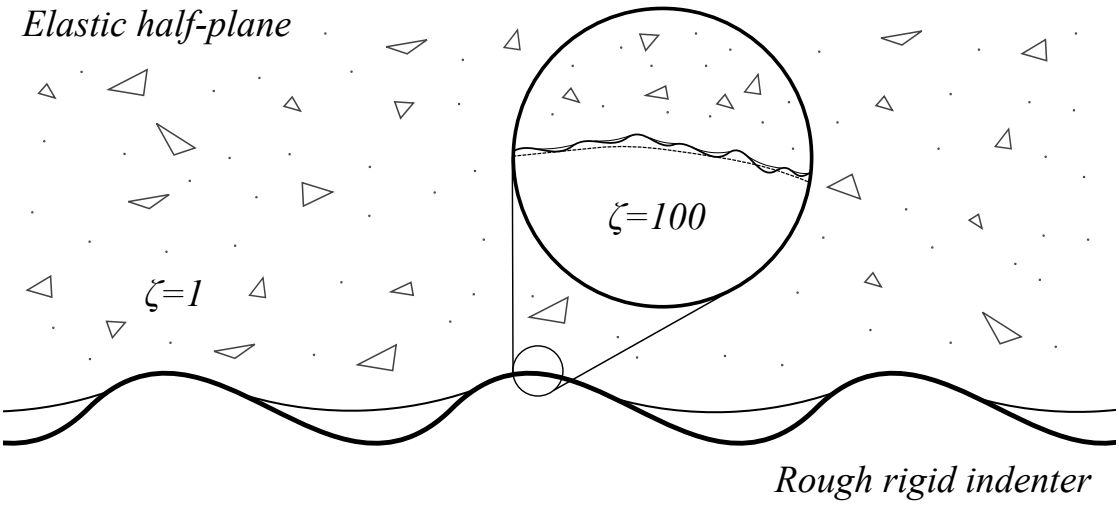

Figure 3.3: Surface roughness evolution as magnification increases. At $\zeta = 1$, the surface appears almost smooth, while with increasing magnification, roughness gradually emerges at increasingly smaller scales. In Persson's model, roughness is described as an intrinsically multi-scale property, in which each new level of magnification reveals additional details that contribute significantly to the real contact and pressure distribution on the surface

Considering condition 3.38, the solution to the diffusion equation 3.34 is Gaussian, centred at σ_m, with variance $2G(\zeta)$:

$$p(\sigma,\zeta) = \frac{1}{\sqrt{4\pi\sigma_m^2 G(\zeta)}} \exp\left[-\frac{(\sigma-\sigma_m)^2}{4\sigma_m^2 G(\zeta)}\right] \tag{3.39}$$

The boundary conditions derive from the observation that, in the absence of adhesion, there can be no contacts subjected to traction, and therefore $p(\sigma,\zeta)$ must be zero for both negative pressures and infinitely large pressures:

$$p(-\infty,\zeta) = 0 \tag{3.40}$$

$$p(\infty,\zeta) = 0 \tag{3.41}$$

In the case of partial contact, boundary condition 3.40 is replaced by requiring that the probability be zero at zero pressure:

$$p(0,\zeta) = 0 \tag{3.42}$$

If we consider the contact area $A(\zeta)$ observed at magnification ζ, it can be proved that in the case of partial contact, the following relationship applies:

$$\frac{A(\zeta)}{A_0} = \int_0^\infty p(\sigma,\zeta)\, d\sigma = erf\left(\frac{\pi}{2\sqrt{G(\zeta)}}\right) \tag{3.43}$$

The previous term allows us to determine the real area as a function of magnification for a given applied load P. It is interesting to note that this relationship suggests that, unlike multi-asperity models, which lose linearity even for extremely small values of real contact area, Persson's theory predicts an almost perfectly linear proportionality up to fractions of the real area of the order of ten to fifteen per cent compared to the nominal area, as shown in [65]. In the particular case of an isotropic surface, it follows that:

$$m_2(\zeta) = \pi \int_{q_L}^{\zeta q_L} q^3 C(q)\, dq \tag{3.44}$$

and substituting this expression into the definition of $G(\zeta)$, equation 3.43 can be rewritten as:

$$\frac{A(\zeta)}{A_0} = erf\left(\frac{\sigma_m}{E^*\sqrt{m_2(\zeta)}}\right) \tag{3.45}$$

3.4 Elastic interactions in multi-asperity contact models and contact coalescence mechanisms

In the previous sections, the most widely used models to address the multi-asperity contact problem have been analyzed. However, these models exhibit some important limitations. A first step towards overcoming the restrictions of the Greenwood

and Williamson model was proposed in [66], where the model was corrected by considering asperity curvatures not as constant, but as dependent on asperity heights. This modification leads to results that closely follow those obtained from the more complex and computationally expensive BGT model. By defining the dimensionless curvatures $\mathcal{K}_1^* = \mathcal{K}_1/\sqrt{m_4}$ and $\mathcal{K}_2^* = \mathcal{K}_2/\sqrt{m_4}$, and the dimensionless summit heights $\xi = \xi_1/\sqrt{m_0}$, the model can be expressed as:

$$\frac{A_c(t)}{A_0} = \frac{\sqrt{\alpha}}{6\sqrt{3}} \int_t^{+\infty} d\xi \frac{\xi - t}{\sqrt{-\bar{\mathcal{K}}_A^*(\xi)}} p_{sum}(\xi) \tag{3.46}$$

$$\frac{F(t)}{A_0 E^* \sqrt{m_2}} = \frac{2\,\alpha^{3/4}}{9\pi\sqrt{3}} \int_t^{+\infty} d\xi \frac{(\xi - t)^{3/2}}{\sqrt{-\bar{\mathcal{K}}_A^*(\xi)}} p_{sum}(\xi) \tag{3.47}$$

where $\bar{\mathcal{K}}_A^*(\xi)$ is given by:

$$\begin{aligned} \bar{\mathcal{K}}_A^*(\xi) = &- \frac{\xi}{\sqrt{\alpha}} + \frac{1}{p_{sum}(\xi)} \frac{3\sqrt{3}}{\sqrt{2\pi}} \exp\left[\frac{\xi^2}{2}\right] \left\{ -\frac{2}{3\sqrt{6\pi}} \frac{1}{\mathcal{C}_1 \sqrt{\mathcal{C}_1}(1+\mathcal{C}_1)} \right. \\ &\times \exp\left(-\frac{3\mathcal{C}_1 \xi^2}{2\alpha}\right) - \frac{\xi}{3\mathcal{C}_1\sqrt{\alpha}} \left[1 + \operatorname{erf}\left(\sqrt{\frac{3\mathcal{C}_1}{2\alpha}}\,\xi\right)\right] \\ &\left. + \frac{\xi\sqrt{\mathcal{C}_1}}{3\sqrt{\alpha\,(1+\mathcal{C}_1)^3}} \left[1 + \operatorname{erf}\left(\sqrt{\frac{\mathcal{C}_1}{2(\alpha-1)}}\,\xi\right)\right] \exp\left(-\frac{\xi^2}{2(\alpha-1)}\right) \right\} \end{aligned} \tag{3.48}$$

and the summit height probability density function is:

$$\begin{aligned} p_{sum}(\xi) = &\frac{3\xi}{2\pi\sqrt{\mathcal{C}_1\alpha}} \exp\left(-\mathcal{C}_1\xi^2\right) + \frac{3\sqrt{3}}{2\alpha\sqrt{2\pi}} (\xi^2 - 1) \exp\left(-\frac{\xi^2}{2}\right) \\ &\times \left\{ 1 + \operatorname{erf}\left[\left(\sqrt{\frac{3\mathcal{C}_1}{2\alpha}}\,\xi\right)\right] \right\} + \sqrt{\frac{\alpha}{2\pi(\alpha-1)}} \\ &\exp\left(-\frac{\alpha}{2(\alpha-1)\xi^2}\right) \left[1 + \operatorname{erf}\left(\sqrt{\frac{\mathcal{C}_1}{2(\alpha-1)}}\,\xi\right)\right] \end{aligned} \tag{3.49}$$

This model predicts an asymptotically linear relationship between real contact area and applied load at small loads, as described by the BGT theory, thereby demonstrating that such behavior arises from including the dependence of curvature distribution on asperity height.

Despite this improvement, some critical issues remain. In the Greenwood and Williamson model, asperities are treated as independent, thus neglecting the interaction between the elastic fields generated by neighboring contacts and the possible coalescence of contact spots into larger contact regions. Conversely, Persson's theory is exact in the full-contact regime, while partial contact is addressed by modifying the boundary conditions of the contact pressure probability distribution. As a result, this theory is expected to lose accuracy when the system

departs significantly from full contact, i.e., for small contact areas and loads. This limitation was indeed highlighted by Carbone et al. [67], who showed that, for one-dimensional roughness, the model underestimates the real contact area by a factor of approximately 1/2 compared to numerical BEM simulations. Both aforementioned models predict a linear relationship between real contact area and applied load at relatively small loads; however, as demonstrated in [65], asperity-based models exhibit this linearity only for vanishing applied loads. To overcome these limitations, a more advanced approach based on multiasperity contact theory was developed in [68]. This model explicitly accounts for mechanical interactions and coalescence mechanisms between asperities, and it was used to study the contact between a rough surface and an elastic half-space. The model builds upon the Greenwood and Williamson formulation, treating the rough surface as a collection of Hertzian paraboloids located near the summits. Non-circular asperities are approximated as circular ones, with an equivalent radius equal to the geometric mean of the principal curvature radii, while lateral interactions between asperities are accounted for following the method proposed in [69]. According to this method, the normal displacement u_i of the elastic half-space at the i-th asperity is expressed as:

$$u_i = \frac{a_i^2}{R_i} + \frac{1}{\pi} \sum_{j=1, j\neq 1}^{n_{tot}} \left(\frac{2a_j^2 - r_{ij}^2}{R_j} \, arcsin \frac{a_j}{r_{ij}} + \frac{a_j}{R_j} \sqrt{r_{ij}^2 - a_j^2} \right) \tag{3.50}$$

where a_i and a_j are the contact radii of the circular Hertzian spots, n_{tot} is the total number of asperities in contact, R_i and R_j are the geometric mean of the principal curvature radii, and r_{ij} is the distance between asperities i and j, defined as:

$$r_{ij} = \sqrt{(x_i - x_j)^2 + (y_i - y_j)^2} \tag{3.51}$$

Defining $z_i = h_i + \delta$ as the coordinate of the i-th summit, with h_i being the asperity height, the numerical scheme described in [69] solves the problem by introducing a corrective factor Δa_i to the contact radius a_i, which is proportional to the asperity indentation $\eta_i = z_i - u_i$. Furthermore, the model accounts for the coalescence of neighboring contacts. When two contact areas overlap, they are replaced by an equivalent single contact whose contact radius and curvature radius are defined as:

$$a_{eqv} = \sqrt{a_i^2 + a_j^2} \tag{3.52}$$

$$R_{eqv} = \sqrt{R_i^2 + R_j^2} \tag{3.53}$$

The position (x_{eqv}, y_{eqv}) of the centroid of the equivalent contact is computed as:

$$x_{eqv} = \left(\frac{a_i^4}{R_i} x_i + \frac{a_j^4}{R_j} x_j \right) \Bigg/ \left(\frac{a_i^4}{R_i} + \frac{a_j^4}{R_j} \right) \tag{3.54}$$

$$y_{eqv} = \left(\frac{a_i^4}{R_i} y_i + \frac{a_j^4}{R_j} y_j \right) \Bigg/ \left(\frac{a_i^4}{R_i} + \frac{a_j^4}{R_j} \right) \tag{3.55}$$

Following these equations, the solution is obtained through the numerical procedure described in [68]. It is worth noting that in the cited paper a comparison was made between load–real contact area curves with and without considering coalescence effects. The analysis clearly showed that the rapid loss of linearity observed in multi-asperity models, as also reported in [65], disappears when coalescence is allowed, thus maintaining linearity up to real contact fractions of approximately 20%, in good agreement with more accurate numerical results.

Chapter 4

Adhesion and friction in viscoelastic rough contacts

4.1 Introduction

Understanding the mechanisms governing friction and contact behavior in polymers has become a topic of fundamental interest over the past years due to the fast increasing number of real-world applications relying on these materials, such as seals, electromechanical grippers [29,70,71], bio-medical devices [72,73], peeling systems [13,74], battery electrodes [75,76], etc. Despite huge theoretical and numerical effort to extend classical contact mechanics results to polymeric interfaces, several fundamental features of the contact response remain unexplained.
In particular, since polymers are usually relatively soft, a fundamental role of interfacial adhesion is expected on the overall contact behavior and especially on friction, as indeed confirmed by several experimental evidences [23,77–84]. However, since polymers usually exhibit a certain degree of viscoelasticity, the system is no longer conservative and theories and calculations derived for the adhesive elastic case even for simple geometries (e.g., Hertzian or wavy) [44,85–87] cannot be straightforwardly extended to cover this case. A possible solution has been sought introducing interfacial gap-dependent potentials able to model finite-ranged repulsive-adhesive interactions [88]. Investigations mostly focus on approach-retraction normal contacts against viscoelastic substrates. It is the case, for instance, fast retracting smooth spheres investigated either numerically, using specific cohesive models to control the gap-dependent force continuity and avoid numerical instability [89], or theoretically in the Maugis-Dugdale adhesion framework and critical crack opening displacements criterion [90]. Still grounding on finite-range adhesion, roughness has been introduced for the same class of normal unsteady contacts. Indeed, studying the case of spheres with axisymmetric (Guduru-like) corrugations in adhesive contact with a viscoelastic solid Nicola and co-authors [91] highlighted a significant interaction between adhesion and viscoelasticity affecting local pull-offs and adhesive instability in the load-area response. In the same framework, Afferrante et al. [37] investigated rough line contacts, showing an increase in pull-off force with increasing preload values.

However, finite-ranged adhesion models still require to set (rather arbitrarily) the maximum cohesive stress, which controls the occurrence of the detachment mechanism through 'quasi-uniform bond breaking' and may significantly affect the overall viscoelastic adhesive pull-off.
Applications such as, for example, tires and seals involve a significantly different contact class; indeed, in this case, relative in-plane motion between the polymeric contacting bodies occurs, which is usually referred to as sliding contact conditions. In this case, disregarding adhesion, it is well known how roughness affects hysteretic friction arising from cyclic deformations of the viscoelastic polymeric material. Indeed, building on the pioneering study on rolling contacts by Hunter [92], in the last two decades this class of contacts has been widely investigated, firstly for single wavelength cases [93], then for multiscale isotropic [64,94,95] and anisotropic [53,96,97] rough contacts always assuming adhesiveless conditions, also considering the effect of finite-sized [56, 98] and coated bodies [99, 100] and interfacial Coulomb friction [101–103]. Only recently, a formalism to include the effect of infinitely short-range adhesion on the viscoelastic contact response has recently been developed, generalizing the local energy balance at the contact edges to take into account for the non-conservative effects of viscoelasticity [24, 25]. The same framework has later been extended to unsteady contact conditions with a precise time history, such as the aforementioned normal approach-retraction cycles of adhesive spheres [26]. A possible strength of this formalism is that adhesion is only characterized by the work of adhesion $\Delta\gamma$; therefore, the maximum cohesive stress is unbounded and crack propagation is the governing phenomenon of detachment.
Currently, only wavy adhesive sliding contacts (single wavelength) have been investigated [24, 25], showing that the interaction between adhesion and viscoelasticity may lead to superior adhesive response and higher viscoelastic friction in great agreement with existing experimental results [77, 78]. However, as a matter of fact, previous studies on elastic solids highlighted that roughness spanning on many length-scales affects adhesive contact mechanics, with both multi-asperity [61] and Persson's theory [104, 105], as well as numerical calculations [106, 107], predicting a likely reduction of the effective adhesion with increasing roughness aspect ratio, especially for large fractal dimension and shot-range adhesive interactions. Overall, the resulting picture is that the role of roughness in viscoelastic adhesive sliding contacts might not be limited to a trivial extension of the elastic-like case, as indeed confirmed by remarkable experimental results showing increased contact area [108] and friction [23]. Nevertheless, this is yet to be addressed in detail.
To close this gap, in this study we focus on self-affine rough indenter sliding past a linear viscoelastic material in the presence of interfacial (infinitely short-ranged) adhesion and, extending the formalism of Refs. [24, 25] to multi-contact conditions, we investigate the resulting adhesive and frictional response of the system. Results highlight significant effect of adhesion, which could also be exploited in tailoring the frictional response of high-performance applications, such as racing tires for automotive industry where interfacial adhesion cannot be neglected and grip response is crucial for vehicle performance, safety and driving efficiency [1].

4.2 Formulation

In this study, we consider the contact of a rigid rough profile sliding past a homogeneous linear viscoelastic half-plane at constant velocity V, as shown in Figure 4.1. At the interface, we assume infinitely short-range adhesive interactions and frictionless conditions.

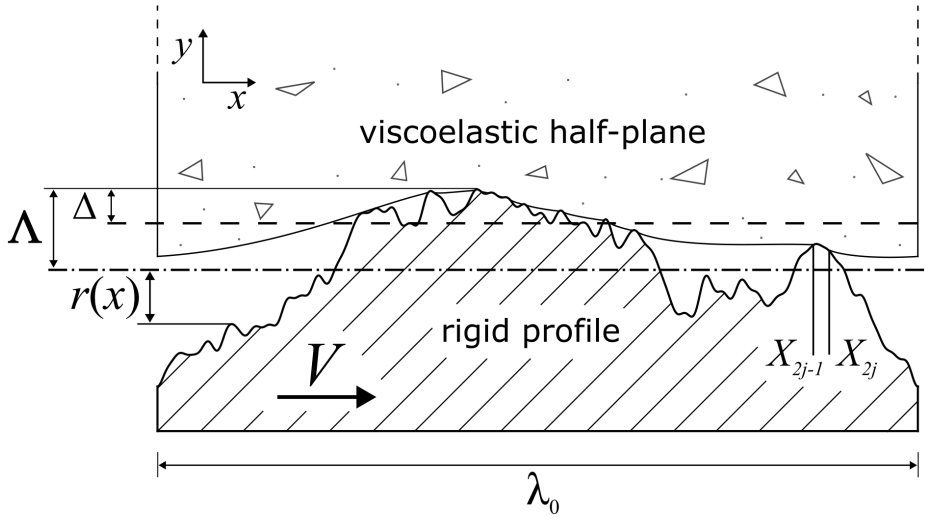

Figure 4.1: The schematic of the contact. r is the rough profile shape, Λ is the rough profile maximum height, Δ is the contact penetration, λ_0 is the fundamental wavelength of the rigid profile, X_{2j-1} and X_{2j} are the trailing edge and leading edge coordinates of the j-th contact, respectively. The dashed and dot-dashed lines represent the mean plane of the deformed viscoelastic solid and rigid profile, respectively

Owing to translational invariance in steady-state sliding [54, 93] the interfacial displacement $u(x)$ normal to the surface of the viscoelastic solid (see section 2.2.3) is given by:

$$u(x) = \int dx_1 \, \mathcal{G}_V(x - x_1) \, \sigma(x_1) \tag{4.1}$$

where $\sigma(x)$ is the normal stress occurring at the interface (positive if tensile). Moreover, in Eq. (4.1), the viscoelastic Green's function $\mathcal{G}_V(x)$ is defined as:

$$\mathcal{G}_V(x) = J(0^+) \, G(x) + \int_{0^+}^{+\infty} G(x + Vt) \, \dot{J}(t) \, dt \tag{4.2}$$

where $G(x)$ is an elastic-like shape function and $J(t)$ is the creep function of the viscoelastic material. For the case of a homogeneous half-plane, the former function is given by:

$$G(x) = \frac{2(1 - \nu^2)}{\pi} \log \left[2 \left| \sin \left(\frac{q_0 \, x}{2} \right) \right| \right] \tag{4.3}$$

with $q_0 = 2\pi/\lambda_0$ being the wave-vector related to the fundamental wavelength λ_0 of the indenter. Moreover, since we focus on a linear viscoelastic material with

one relaxation time τ, following the approach introduced in section 2.1, the creep function $J(t)$ takes the form:

$$J(t) = H(t) \left[\frac{1}{E_0} - \frac{1}{E_1} \exp(-t/\tau) \right] \tag{4.4}$$

where $H(t)$ is the Heavyside step function and:

$$\frac{1}{E_1} = \frac{1}{E_0} - \frac{1}{E_\infty} \tag{4.5}$$

with E_0 and E_∞ being the zero-frequency and the very high frequency elastic moduli of the material, respectively. Importantly, the same procedure can be extended to the generic case of a material with N_τ relaxation times [26, 57, 109], with creep function given by:

$$J(t) = H(t) \left[E_0^{-1} - \sum_i^{N_\tau} E_i^{-1} \exp(-t/\tau_i) \right] \tag{4.6}$$

Furthermore, dealing with a rough contact interface, the overall contact domain Ω (of size given $A = |\Omega|$) is split into a total number N_c of separate contact regions Ω_j, so that $\Omega = \cup_{j=1}^{N_c} \Omega_j$. Consequently, with reference to Fig. 4.1, the total number of contact edges is $2N_c$, and the coordinates of the leading and trailing edges of the generic j-th contact region are X_{2j} and X_{2j-1}, respectively.
Within each contact region, since the indenter and the deformed viscoelastic material mate to each other, we have:

$$u(x) = r(x) - \Lambda + \Delta \tag{4.7}$$

with $r(x)$ being the local profile height and $\Lambda = \max[r(x)]$. Hence, using Eq. 4.1, we have:

$$\sum_{j=1}^{N_c} \int_{X_{(2j-1)}}^{X_{2j}} dx_1 \, \mathcal{G}_V(x - x_1) \, \sigma(x_1) = r(x) - \Lambda + \Delta \tag{4.8}$$

allowing to calculate the unknown contact stress distribution $\sigma(x)$ as a function of sliding velocity V, contact penetration Δ and contact edges coordinates X_i, with $i = 1, ..., 2N_c$. This is achieved by relying on the numerical procedure addressed in Ref. [55], using a non-uniform discretization of the contact domain Ω. Such a methodology has been widely validated in previous studies [109, 110], by comparison with experimental viscoelastic results.
However, while V and Δ are control parameters, a closing condition is required to determine the contact edges coordinates X_i. Indeed, since we assume infinitely short-ranged adhesive interactions at the interface and we deal with a viscoelastic material, the condition to enforce is a local energy balance at each contact edge, which is a generalisation of Griffith's fracture criterion, presented in section 1.3, to hysteretic materials. In agreement with Refs. [24, 25], assuming an infinitesimal quasi-static perturbation δX at the generic i-th contact edge, we have:

$$\delta L_i = \Delta \gamma \delta X \tag{4.9}$$

where δL_i is the work done by the internal stresses and $\Delta\gamma$ is the surface energy per unit area (i.e., the Duprè work of adhesion). Notably, without any loss of generality, in writing Eq. (4.9) we implicitly assumed that the perturbation δX leads to an increase of the overall contact area; therefore, focusing on the generic contact spot Ω_j, the perturbation leads to a new domain $\Omega_j + \delta\Omega_j$ which, in terms of edges coordinates, can be achieved varying either the leading edge $X_{2j} \rightarrow (X_{2j} + \delta X)$ or the trailing edge $X_{(2j-1)} \rightarrow (X_{(2j-1)} - \delta X)$.
Given that a viscoelastic material exhibits hysteretic behavior, the term δL_i can be expressed as the sum of conservative (namely, the change in the elastic potential energy stored in the solid) δU_i and non-conservative δL_{P_i} terms:

$$\delta L_i = \delta U_i + \delta L_{P_i} \tag{4.10}$$

Consequently, the closing condition given by Eq. (4.10) can be rewritten at the generic i-th contact edge as:

$$\left.\frac{\partial U_i}{\partial X}\right|_{\Delta, X_{k\neq i}} + \left.\frac{\delta L_{P_i}}{\delta X}\right|_{\Delta, X_{k\neq i}} = \Delta\gamma \tag{4.11}$$

Equilibrium occurs when Eq.(4.11) is satisfied at all the $2N_c$ contact edges at the same time.
A detailed theoretical framework to derive the terms in Eqs. (4.10-4.11) is provided in Refs. [24, 25]. Here, we focus on their expressions allowing for an efficient numerical calculation of the closure condition, i.e. Eq. (4.11); indeed, we define u^- and σ^- as the normal displacement and stress fields, respectively, right before the generic i-th contact edge undergoes the perturbation; similarly, u^+ and σ^+ are the same fields right after the perturbation. The change in the displacement field is $\Delta u = u^+ - u^-$ and, following [25], we have:

$$\delta L_i = \frac{1}{2}\int dx \sigma^+(x)\Delta u(x) = \frac{1}{2}\int dx \left[u^+(x) - u^-(x)\right]\left[\sigma^+(x) + \sigma^-(x)\right] \tag{4.12}$$

Similarly, since the elastic potential energy is defined as $U = \frac{1}{2}\int dx \sigma(x)u(x)$, we have:

$$\delta U_i = \frac{1}{2}\int dx \left[u^+(x)\sigma^+(x) - u^-(x)\sigma^-(x)\right] \tag{4.13}$$

and the non-conservative term can be found combining Eqs. (4.10,4.12,4.13) as:

$$\delta L_{P_i} = \delta L_i - \delta U_i = \frac{1}{2}\int dx \left[u^+(x)\sigma^-(x) - u^-(x)\sigma^+(x)\right] \tag{4.14}$$

Once the equilibrium configuration is found, the contact stress distribution is derived inverting Eq. (4.8) and the remote mean contact pressure can be calculated as:

$$p_\infty = \frac{1}{\lambda_0}\int_\Omega p(x)\, dx \tag{4.15}$$

with $p(x) = -\sigma(x)$ being the contact pressure distribution. Under the assumption of frictionless sliding, the contact stress vector is, by definition, always normal to

the interface, so that only repulsive or adhesive normal interactions are present, with no shear stresses in the tangential direction. In the purely elastic case, this condition implies the absence of any lateral force opposing the relative motion. However, when viscoelastic effects are taken into account, the situation is fundamentally different. The viscous rheology of the material causes energy dissipation during deformation, which in turn leads to an asymmetric distribution of normal stresses across each asperity. Because the local surface normal is not vertical (due to surface roughness), such an asymmetric pressure distribution generates a non-vanishing lateral component of the contact force that opposes the sliding motion.

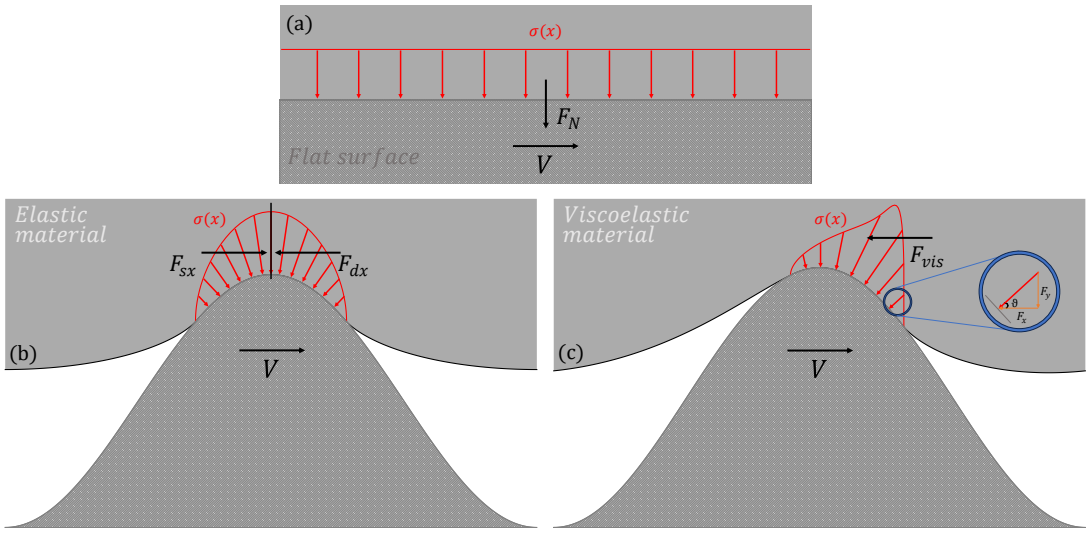

Figure 4.2: Schematic illustration of the contact mechanics under frictionless sliding conditions. (a) Flat surface: in the absence of asperities, no frictional force arises. (b) Sinusoidal surface in contact with an elastic substrate: although surface roughness is present, the pressure distribution remains symmetric and no friction is generated. (c) Sinusoidal surface in contact with a viscoelastic substrate: the viscous rheology of the material leads to internal energy dissipation and an asymmetric pressure distribution, which in turn produces a non-vanishing lateral force component, i.e. viscoelastic friction

This phenomenon, commonly referred to as viscoelastic friction, has been widely investigated in the literature [56, 64, 100, 102, 105]. In this framework, the corresponding viscoelastic friction coefficient is given by:

$$\mu = \frac{1}{\lambda_0 \, p_\infty} \int_\Omega p(x) \, u'(x) \, dx \tag{4.16}$$

Regarding the possible role of frictional shear stresses at the interface, it is worth noting that, in linear (visco)elasticity, no significant influence on the viscoelastic friction is expected for rubberlike (i.e., incompressible) materials. Indeed, for incompressible half-plane problems, the normal and tangential fields are decoupled [102], implying that shear stresses are unlikely to affect either the asymmetry of the pressure distribution or, consequently, the viscoelastic friction.

To better contextualise this formulation within the broader framework of rough contact mechanics models and to highlight the contributions introduced in this work with respect to existing approaches, it is useful to compare the proposed model with the theories discussed in chapter 3. In fact, as already pointed out previously, classical approaches capture different aspects of rough contact, but have limitations when it is necessary to deal simultaneously with multiscale roughness, viscoelasticity, and adhesion. For this reason, table 4.1 summarises the main assumptions and limitations of the models examined in chapter 3, comparing them directly with the methodology proposed here.

Model	Main assumptions	Main limitations
Greenwood & Williamson (1966)	Surface represented as statistically distributed spherical asperities; independent Hertzian contacts; Gaussian height distribution of summits	Neglects elastic interactions between asperities; no contact coalescence; mono-scale description; accurate only for small loads and small real contact fractions
Fuller & Tabor (1975)	GW model including short-range adhesion using JKR theory; intended for soft materials with large Tabor parameter ($\mu \gg 1$)	Severely simplified topography; no multiscale effects; adhesion treated only in the JKR regime
Bush, Gibson & Thomas (1975)	Asperities modelled as elliptical Hertzian contacts; Gaussian height distribution of summits; curvature distribution derived from PSD and spectral moments; isotropic Gaussian rough surfaces	Ignores all elastic interactions; purely non-adhesive model; still an asperity-based approach despite improved curvature statistics
Greenwood (2006)	Simplified BGT-type model; equivalent spherical contacts based on Gaussian curvature of summits	No elastic interactions; single-scale representation; still approximates true multiscale roughness; purely non-adhesive model;
Carbone et al. (2009)	GW model corrected by introducing curvature-height dependence	Still no coalescence of micro-contacts; asperities are treated as independent; surface statistics simplified; limited to non-adhesive elastic contact
Afferrante et al. (2012)	Elastic Hertzian asperities with both elastic interactions and contact coalescence; non-circular asperities are approximated as circular ones	Still approximates true multiscale roughness; no adhesive forces included; simplified treatment of asperity coalescence by replacing overlapping contact spots with a single equivalent asperity
Persson (2001)	Continuum multiscale theory where contact stresses evolve through a diffusion-like equation in magnification space; formulation based on the surface PSD and valid for self-affine Gaussian rough surfaces	The theory lose accuracy when the system departs significantly from full contact, i.e., for small contact areas and loads; adhesion and viscoelasticity require additional extensions; no explicit representation of discrete micro-contacts or their coalescence
Proposed model (2025)	Rigid self-affine rough indenter sliding on a homogeneous linear viscoelastic half-plane; steady-state formulation using a viscoelastic Green's function; infinitely short-range adhesion characterized by the Dupré work of adhesion; local energy balance at each contact edge (viscoelastic generalization of Griffith criterion); no interfacial shear stresses (friction arising solely from viscoelastic dissipation)	Material assumed linear viscoelastic with a single relaxation time; 1D + 1D formulation; computational cost associated with the multi-edge energy balance procedure

Table 4.1: Comparison between the model proposed in this thesis and the main theoretical models for rough contact

4.3 Non-dimensionalization procedure

To simplify the discussion, the problem can be reformulated in terms of the following dimensionless quantities:

$$\begin{aligned} \tilde{x} &= q_0\, x & \tilde{A} &= q_0\, A \\ \tilde{p} &= \frac{2(1-\nu^2)}{E_0\, q_0\, \Lambda}\, p & \tilde{\gamma} &= \frac{(1-\nu^2)\, q_0}{\pi\, E_0}\, \Delta\gamma \\ \zeta &= q_0\, V\, \tau & \tilde{u} &= \frac{u}{\Lambda} \\ \tilde{\Lambda} &= q_0\, \Lambda & \tilde{\Delta} &= \frac{\Delta}{\Lambda} \\ \tilde{U} &= \frac{2(1-\nu^2)}{E_0\, \Lambda^2}\, U & \tilde{L}_P &= \frac{2(1-\nu^2)}{E_0\, \Lambda^2}\, L_P \end{aligned} \tag{4.17}$$

By introducing these quantities, equation 4.8 can be rewritten in dimensionless form as:

$$\sum_{j=1}^{N_c} \int_{\tilde{X}_{(2j-1)}}^{\tilde{X}_{2j}} d\tilde{x}_1\, \tilde{\mathcal{G}}_V(\tilde{x}-\tilde{x}_1)\, \tilde{\sigma}(\tilde{x}_1) = \tilde{r}(\tilde{x}) - 1 + \tilde{\Delta} \tag{4.18}$$

where the dimensionless Green's function is defined as:

$$\tilde{\mathcal{G}}_V(\tilde{x}) = \frac{1}{\pi\beta}\, log \left| 2\, sin\left(\frac{\tilde{x}}{2}\right)\right| + \frac{\beta-1}{\pi\beta} \int_{0^+}^{+\infty} dt\, log \left| 2\, sin\left(\frac{\tilde{x}+\zeta\, t}{2}\right)\right| \exp(-t) \tag{4.19}$$

where β denotes the ratio between the high- and low-frequency elastic moduli of the viscoelastic material. The closure equation 4.11 can then be expressed in dimensionless form as:

$$\left.\frac{\partial \tilde{U}_i}{\partial \tilde{X}}\right|_{\tilde{\Delta}, \tilde{X}_{k\neq i}} + \left.\frac{\delta \tilde{L}_{P_i}}{\delta \tilde{X}}\right|_{\tilde{\Delta}, \tilde{X}_{k\neq i}} = \frac{2\pi\tilde{\gamma}}{\tilde{\Lambda}^2} \tag{4.20}$$

4.4 Numerical implementation

In order to numerically solve equation 4.18, it is necessary to discretise the contact domain. To this aim, the numerical procedure proposed in [55, 67] is adopted, based on a non-uniform adaptive mesh. The discretisation strategy involves the construction, for each contact region, of an adaptive grid capable of concentrating a larger number of points near the edges, where the distribution of interfacial stresses, due to adhesion, presents a square root singularity. Let Ω_j be the j-th contact region, bounded by the coordinates $\tilde{X}_{2j-1}$ and $\tilde{X}_{2j}$. Let us define the centre of contact as $\mu_j = (\tilde{X}_{2j} + \tilde{X}_{2j-1})/2$ and its half-width as $\alpha_j = (\tilde{X}_{2j} - \tilde{X}_{2j-1})/2$. By introducing the local variable $\eta = \tilde{x} - \mu_j$, the domain Ω_j is mapped to the interval $[-\alpha_j, \alpha_j]$, centred at zero. A uniform mesh $\mathcal{U}$ consisting of $N+1$ points

ζ_l is generated on this interval:

$$\zeta_l = -\alpha_j + 2\alpha_j \frac{l}{N} \qquad l = 0, \ldots, N \tag{4.21}$$

Starting from the uniform grid $\mathcal{U}$, an adaptive non-uniform mesh $\mathcal{P}$ is obtained by mapping:

$$z_l = \mathcal{M}(\zeta_l) \qquad l = 0, \ldots, N \tag{4.22}$$

where the transformation function $\mathcal{M}(\zeta)$ is defined so as to densify the points near the edges of the contact, respecting the conditions $\mathcal{M}(-\alpha_j) = -\alpha_j$ and $\mathcal{M}(\alpha_j) = \alpha_j$. The solution to the integral equation is then sought on a mesh of centres $\mathcal{C}$, whose points ξ_l are the midpoints of the subintervals of the grid $\mathcal{P}$:

$$\xi_l = \frac{z_l + z_{l-1}}{2} \qquad l = 1, \ldots, N \tag{4.23}$$

As a result, the mesh $\mathcal{C}$ does not include the contact edges ($-\alpha_j$ and α_j). We also define the mesh of element lengths $\mathcal{H}$, associated with the grid $\mathcal{P}$, consisting of N elements:

$$h_l = z_l - z_{l-1} \qquad l = 1, \ldots, N \tag{4.24}$$

To obtain sufficiently accurate discretisation, particularly near the contact edges, the mapping function $\mathcal{M}(\zeta)$ must be defined so that the density of points:

$$\rho(\zeta) = \frac{1}{\mathcal{M}'(\zeta)} \tag{4.25}$$

diverges near the contact edges. The normalisation condition for mapping requires:

$$\int_{-\alpha_j}^{\alpha_j} \mathcal{M}'(\zeta)\, d\zeta = \mathcal{M}(\alpha_j) - \mathcal{M}(-\alpha_j) = 2\alpha_j \tag{4.26}$$

Since the normal stress σ_{yy} has a singularity of type $\sqrt{r}$ near the edges, the point density can be assumed to have the following form:

$$\rho(s) = C\, \frac{1}{[\cos(s) - \cos(\alpha_j)]^n} \qquad n \geq \frac{1}{2} \tag{4.27}$$

where the normalisation constant C is obtained from:

$$C = \frac{1}{2\alpha_j} \int_{-\alpha_j}^{\alpha_j} [\cos(\xi) - \cos(\alpha_j)]^n d\xi \tag{4.28}$$

The mapping $\mathcal{M}(\zeta)$ is therefore:

$$\mathcal{M}(\zeta) = \frac{1}{C} \int_0^{\zeta} [\cos(\xi) - \cos(\alpha_j)]^n d\xi \tag{4.29}$$

Once the discretisation has been established, the integral equation 4.18 can be converted into a linear system of equations using a numerical quadrature rule:

$$\sum_{q=1}^{N} \int_{\xi_q - h_q/2}^{\xi_q + h_q/2} d\eta\, \tilde{\mathcal{G}}_V(\xi_l - \eta)\, \tilde{\sigma}_q = \tilde{r}(\xi_l) - 1 + \tilde{\Delta} \tag{4.30}$$

The resulting numerical problem is therefore a linear system of N equations in N unknowns:

$$\sum_{q=1}^{N} B_{lq}\,\tilde{\sigma}_q = \tilde{r}(\xi_l) - 1 + \tilde{\Delta} \qquad l = 1, \ldots, N \tag{4.31}$$

with:

$$B_{lq} = \int_{\xi_q - h_q/2}^{\xi_q + h_q/2} d\eta\, \tilde{\mathcal{G}}_V(\xi_l - \eta) \tag{4.32}$$

Given an assigned penetration value and the initial configuration of the contact regions, it is possible to solve equation 4.31 and determine all the characteristic quantities of the solution. The position of the contact edges is then updated iteratively using an appropriate numerical algorithm until the solution with the desired level of accuracy is achieved. The main numerical methods used will be described in the next section.
It should be noted that the problem is particularly complex, since the number of contacts may vary during the minimisation procedure. In particular, a contact may detach or two adjacent contacts may coalesce into a single larger region. In such circumstances, the minimisation procedure must be restarted in a space of a different dimension. Therefore, it is not only a matter of solving a minimisation problem in $2N_c$ variables $\tilde{X}_i$, but also of determining the number N_c of contact regions corresponding to the equilibrium configuration, which is unknown a priori. In addition, at each step of the algorithm, it is necessary to impose the condition that, in the non-contact regions, the viscoelastic layer never intersects the peaks of the substrate. If this condition is not satisfied, it is necessary to introduce a new contact or expand an existing contact region, restarting the minimisation procedure accordingly. In this way, at each iteration, the minimisation phase is followed by a verification and a possible update of the contact configuration. The algorithm is stopped when the procedure converges correctly, i.e. when no further contact coalescence or detachment occurs and the subsequent verification confirms the absence of intersections in the non-contact regions. Moreover, it should be noted that there is no single solution to the contact problem in the presence of adhesion: for the same penetration, there may be several equilibrium configurations, the realisation of which depends on the load history of the system and the evolutionary path followed during the contact and detachment process.

4.5 Numerical solving algorithms

This chapter is devoted to a description of some of the main numerical methods for solving systems of non-linear equations in multiple dimensions, used in this thesis in the development of algorithms to determine the equilibrium configuration of the system under study. The methods employed include: Newton-Raphson multidimensional, Broyden, nonlinear Conjugate Gradient and the bisection method. In the multidimensional context, defined a non-linear vector-valued function $\mathbf{f} : \mathbb{R}^n \longrightarrow \mathbb{R}^m$, a nonlinear system consists of a set of equations of the

type $\mathbf{f}(\mathbf{X}) = 0$, with $\mathbf{X} = \{X_1, X_2, ..., X_n\}^T$ being the unknown vector. Contrary to linear systems, for which direct and numerically stable methods exist (such as Gauss elimination or Cramer's method), the resolution of non-linear systems often requires the use of iterative methods, which are capable of progressively approximating the solution through a process based on subsequent updates. In this context, the use of numerical methods is of fundamental importance, since it allows approximate solutions, but with controllable precision, to be obtained for systems of equations for which exact solution by analytical methods is impractical - either because such solutions do not exist in closed form, or because the equations involved are too complex to solve symbolically. Almost all of the methods considered are based on approximating the n-dimensional function by means of local linear models (e.g. via Taylor development), and iterating from an initial estimate of the solution, allowing for an iterative process of finding the solution. In particular, methods such as Newton-Raphson exploit the Jacobian matrix of the function $\mathbf{f}(\mathbf{X})$, while other methods attempt to avoid its explicit calculation (such as Broyden) or use optimised descent directions (such as the Conjugate Gradient).

4.5.1 Newton-Raphson multidimensional method

The Newton-Raphson method is one of the best known and simplest numerical methods for solving non-linear systems. Given an initial point $\mathbf{X}_0$, it generates a subsequence of values $\{\mathbf{X}_k\}_{k\geq 0}$ which, under appropriate assumptions, converges to a solution $\mathbf{X}^*$ such that $\mathbf{f}(\mathbf{X}^*) = 0$. In fact, Newton's method for solving non-linear systems is based on the linearization of a vectorial function $\mathbf{f}(\mathbf{X}) = [f_1(\mathbf{X}), ..., f_m(\mathbf{X})]^T$ by means of the Taylor series expansion of the function in the neighbourhood of the point $\mathbf{X}_k$. If we define the Jacobian Matrix of a function $\mathbf{f}$ as:

$$J_{\mathbf{f}}(\mathbf{X}) = \begin{bmatrix} \frac{\partial f_1}{\partial X_1} & \cdots & \frac{\partial f_1}{\partial X_n} \\ \vdots & \ddots & \vdots \\ \frac{\partial f_m}{\partial X_1} & \cdots & \frac{\partial f_m}{\partial X_n} \end{bmatrix} \tag{4.33}$$

we can then write the Taylor series expansion of a vector-valued function in multiple variables around a point as:

$$\mathbf{f}(\mathbf{X}) = \mathbf{f}(\mathbf{X}_k) + J_{\mathbf{f}}(\mathbf{X}_k)(\mathbf{X} - \mathbf{X}_k) + ... \tag{4.34}$$

of which we neglect terms of higher than first order, introducing a truncation error at second order. Now requiring our solution to be $\mathbf{f}(\mathbf{X}) = 0$ and inverting the equation 4.34 we can obtain the i-th iteration as:

$$\mathbf{X}_{i+1} = \mathbf{X}_k - J_{\mathbf{f}}(\mathbf{X}_k)^{-1}\mathbf{f}(\mathbf{X}_k) \tag{4.35}$$

with $s_k = -J_{\mathbf{f}}(\mathbf{X}_k)^{-1}\mathbf{f}(\mathbf{X}_k)$ which is called the updating step of the algorithm. The advantage of Newton's method is that it has a quadratic rate of convergence, but it assumes an initial estimate $\mathbf{X}_0$ sufficiently close to the solution of the system

and requires the computation of $J_{\mathbf{f}}(\mathbf{X}_k)$ at each iteration, which can be a computationally onerous task for systems with a large number of variables.
In contact mechanics, this method can be used to address both the elastic contact case and the related viscoelastic case in the presence or absence of adhesion. Regarding the elastic case, in this discussion we refer to the adhesiveless case, thus searching for the equilibrium configuration corresponding to the minimum elastic energy $\tilde{U}_{el}$. However, the same approach can be extended to the adhesive case, for which we consider the minimum of the total energy $\tilde{U}_{tot} = \tilde{U}_{el} + \tilde{U}_{adh}$. In our case the independent varibles for the system will be the contacts region coordinates $\tilde{\mathbf{X}} = \{\tilde{X}_1, \tilde{X}_2, ..., \tilde{X}_{2N_c}\}^T$, with N_c being the number of contacts for our system. The target function in this case is represented by the gradient $\nabla\tilde{U}_{el}(\tilde{\mathbf{X}}) = 0$; hence the Newton-Raphson method can be formulated as:

$$\tilde{\mathbf{X}}_{i+1} = \tilde{\mathbf{X}}_k - J_{\nabla\tilde{U}_{el}}(\tilde{\mathbf{X}}_k)^{-1}\nabla\tilde{U}_{el}(\tilde{\mathbf{X}}_k) \tag{4.36}$$

with

$$J_{\nabla\tilde{U}_{el}}(\tilde{\mathbf{X}}) = \begin{bmatrix} \dfrac{\partial^2\tilde{U}_{el}}{\partial\tilde{X}_1^2} & \cdots & \dfrac{\partial^2\tilde{U}_{el}}{\partial\tilde{X}_1\partial\tilde{X}_{2N_c}} \\ \vdots & \ddots & \vdots \\ \dfrac{\partial^2\tilde{U}_{el}}{\partial\tilde{X}_{2N_c}\partial\tilde{X}_1} & \cdots & \dfrac{\partial^2\tilde{U}_{el}}{\partial\tilde{X}_{2N_c}^2} \end{bmatrix} \tag{4.37}$$

which in this case is none other than the Hessian matrix $H_{\tilde{U}_{el}}(\tilde{\mathbf{X}})$ having dimension $2N_c \times 2N_c$ and being Symmetric for the Schwarz's Theorem:

$$\frac{\partial^2\tilde{U}_{el}}{\partial\tilde{X}_i\,\partial\tilde{X}_j} = \frac{\partial^2\tilde{U}_{el}}{\partial\tilde{X}_j\,\partial\tilde{X}_i} \tag{4.38}$$

In the adhesive viscoelastic case, however, the goal is to find the configuration for which is valid for each contact apex the equation:

$$\delta\tilde{U}_i = \frac{2\pi\tilde{\gamma}}{\tilde{\Lambda}^2}\,\delta\tilde{X} - \delta\tilde{L}_{Pi} \tag{4.39}$$

with $i = 1, ..., 2N_c$. Accordingly, one can apply this method to the set of equations $g_i(\tilde{\mathbf{X}}) = \delta\tilde{U}_i - (2\pi\tilde{\gamma}/\tilde{\Lambda}^2)\,\delta\tilde{X} + \delta\tilde{L}_{Pi} = 0$, which applied to each contact edge gives us a vector-valued function on which the method as described above can be applied. In the same way, this algorithm can be applied to the viscoelastic adhesiveless case, for which $g_i(\tilde{\mathbf{X}}) = \delta\tilde{U}_i + \delta\tilde{L}_{Pi} = 0$, thus considering the equations $g_i(\tilde{\mathbf{X}}) = \delta\tilde{U}_i + \delta\tilde{L}_{Pi} = 0$.

4.5.2 Broyden method

The secants method is an alternative to the Newton-Raphson method for solving non-linear equations, which is distinguished by the fact that it does not require the explicit derivative of the function, but approximates it via finite differences.

This makes it particularly useful in cases where calculating the derivative is too burdensome or impractical. Its convergence is superlinear: faster than the bisection method, but generally less efficient than the Newton-Raphson method. A generalisation of the secant method to the multidimensional case is the Broyden method, which belongs to the broader class of Quasi-Newton methods. These methods use an approximation of the Jacobian matrix, denoted B_i, thus avoiding its direct calculation at each iteration. Broyden's method, in particular, is a variant of the Newton-Raphson method in which the Jacobian is replaced by an iteratively updated matrix, based on an estimate made from the values obtained from the previous iteration, thus significantly reducing computational costs. To apply the method, it is necessary to provide an initial value $\mathbf{X}_0$, and an initial matrix $B_0 \approx J(\mathbf{X}_0)$, an approximation of the Jacobian. The main iteration of the method is given by:

$$\mathbf{X}_{i+1} = \mathbf{X}_i - B_i^{-1}\mathbf{f}(\mathbf{X}_i) \tag{4.40}$$

where B_i is the approximation of the Jacobian at the i-th iteration. To update B_i, we define the updating step $s_i = -B_i^{-1}\mathbf{f}(\mathbf{X}_i)$ and the variation of the function $y_i = \mathbf{f}(\mathbf{X}_{i+1}) - \mathbf{f}(\mathbf{X}_i)$. The update of the approximate matrix is then:

$$B_{i+1} = B_i + \frac{(y_i - B_i s_i)s_i^T}{s_i^T s_i} \tag{4.41}$$

It is often preferred to update the inverse B_i^{-1} directly, e.g. by means of the Sherman-Morrison formula, so as to avoid inverting the matrix at each iteration:

$$B_{i+1}^{-1} = B_i^{-1} + \frac{s_i - B_i^{-1}y_i}{s_i^T B_i^{-1} y_i} s_i^T B_i^{-1} \tag{4.42}$$

To ensure the numerical stability of the algorithm, particularly near the function's inflection points where the derivatives may tend to zero (and thus their inverses diverge), it may be useful to introduce a sub-relaxation factor $\alpha < 1$. This allows better control over the size of the updating step, especially in cases where the matrix inversion is unstable. For more details on the development of this method, the reader is referred to Ref. [111].

4.5.3 Non-linear conjugate gradient

The non-linear conjugate gradient method is a numerical optimisation technique used to find local minima of non-linear functions, and is an extension of the classical conjugate gradient method, originally developed to solve sparse linear systems. It is employed in the minimisation of a scalar function defined on a vector space, i.e. a function of the type $\mathbf{f} : \mathbb{R}^n \longrightarrow \mathbb{R}$, and relies on the use of the gradient of the function to guide the descent towards a minimum. The method is particularly useful in large scale problems, where the use of the Hessian (as in Newton's method) would be computationally too onerous. Unlike the simple gradient method, which always moves in the direction opposite the gradient, this method

constructs so-called 'conjugate' directions at each step, combining the current gradient information with that of previous iterations. These conjugate directions allow for more efficient progress in the solution space, reducing the possibility of oscillations and improving the speed of convergence. During the optimisation, the function is evaluated along each conjugate direction through a procedure called line search, which is used to determine the optimal step α_k to be taken in that direction to reduce the value of the objective function as much as possible, by performing a one-dimensional minimisation of the function along the line defined by $\mathbf{X}_k$ and d_k. This process can take place with different strategies, such as backtracking, which progressively reduces α until a sufficient decrease in energy is observed according to an Armijo-type condition, or with more sophisticated methods that impose additional conditions (such as Wolfe's conditions) to guarantee convergence and robustness. To apply the non-linear conjugate gradient method, we start by

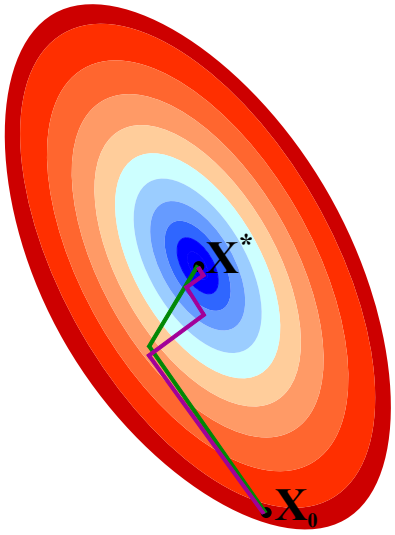

Figure 4.3: A comparison of the convergence of the gradient method (in purple) and the conjugate gradient method (in green) for minimizing a scalar function in the variable $\mathbf{X}$

choosing an initial point $\mathbf{X}_0$, which represents an initial estimate of the solution. We then compute the gradient of the function at the initial point, $g_0 = \nabla \mathbf{f}(\mathbf{X}_0)$, and set the initial descent direction as $d_0 = -g_0$. From here, for each iteration $k = 0, 1, 2, \ldots$, a linear search is performed to determine a step value α_k that minimises the function along the current direction, i.e. the minimum of the function $\mathbf{f}(\mathbf{X}_k + \alpha d_k)$ is sought. Once the optimal step is determined, the position is updated according to the formula $\mathbf{X}_{k+1} = \mathbf{X}_k + \alpha_k d_k$. Next, the gradient at the new point is recalculated, obtaining $g_{k+1} = \nabla \mathbf{f}(\mathbf{X}_{k+1})$, and a coefficient β_k is calculated to update the direction of descent so that it is conjugate to the previous one. A possible calculation of β_k is given by the Fletcher-Reeves formula:

$$\beta_k^{FR} = \frac{g_{k+1}^T g_{k+1}}{g_k^T g_k} \tag{4.43}$$

or that of Polak-Ribière:

$$\beta_k^{PR} = \frac{g_{k+1}^T(g_{k+1} - g_k)}{g_k^T g_k} \tag{4.44}$$

although other variants also exist. With this coefficient, the new direction is defined as $d_{k+1} = -g_{k+1} + \beta_k d_k$, combining the current gradient with the previous direction. The process is repeated until the norm of the gradient $\|\nabla f(x_k)\|$ is sufficiently small, indicating that a point of minimum has been reached (or come very close).
In the elastic case, this method can be applied to find the configuration that minimises the system's energy, i.e. its equilibrium configuration. In the adhesiveless case, the equilibrium configuration corresponds to the minimization of the elastic energy, $\min\left[\tilde{U}_{el}\right]$, whereas in the adhesive case, it results from the minimization of the total energy, $\min\left[\tilde{U}_{tot}\right]$. The line search method in this case will be implemented by imposing that at each moving step along the line, the relation $\tilde{U}(step_{k+1}) < \tilde{U}(step_k)$ holds, i.e. verifying that the energy is decreasing in the chosen direction, until finding the minimum along the line. For the viscoelastic adhesive case, the conjugate gradient method can be adapted by writing the equation 4.39 at each contact edge and requiring that the sum of the squares of the quantities thus calculated is null:

$$\sum_{i=1}^{2N_c} \left(\delta\tilde{U}_i - \frac{2\pi\tilde{\gamma}}{\tilde{\Lambda}^2}\,\delta\tilde{X} + \delta\tilde{L}_{Pi} \right)^2 = 0 \tag{4.45}$$

with the quantity $\tilde{\gamma}$ which will be zero in the adhesiveless case.

4.5.4 Bisection method

In numerical analysis, the bisection method (or dichotomic algorithm) represents one of the simplest and most reliable strategies for determining the zeros of a real function. The fundamental principle on which it is based is the Bolzano theorem, according to which, if a continuous function $f(x)$ assumes opposite signs at the extremes of an interval $[a, b]$, i.e. if $f(a) \cdot f(b) < 0$, then there exists at least one point $c \in (a, b)$ such that $f(c) = 0$.
The method consists of iteratively calculating the midpoint of the interval, $c = (a + b)/2$, and determining in which of the two halves the equation changes sign. If $f(a) \cdot f(c) < 0$, then the root is in the interval $[a, c]$, and we set $b = c$; otherwise, if $f(c) \cdot f(b) < 0$, the root is in $[c, b]$, and we set $a = c$ (Fig.4.4). The procedure is repeated until the absolute value of $f(c)$ falls below a fixed threshold δ, indicative of the desired accuracy. This approach, while being of linear order in terms of speed of convergence, guarantees robustness and certainty of existence of the solution under appropriate conditions. This method is particularly useful in the context of adhesiveless mechanical contact problems, in both the elastic and viscoelastic cases, where the pressures at the contact edges vanish in both cases. In such contexts, bisection allows precise control of the pressures at the contact edges,

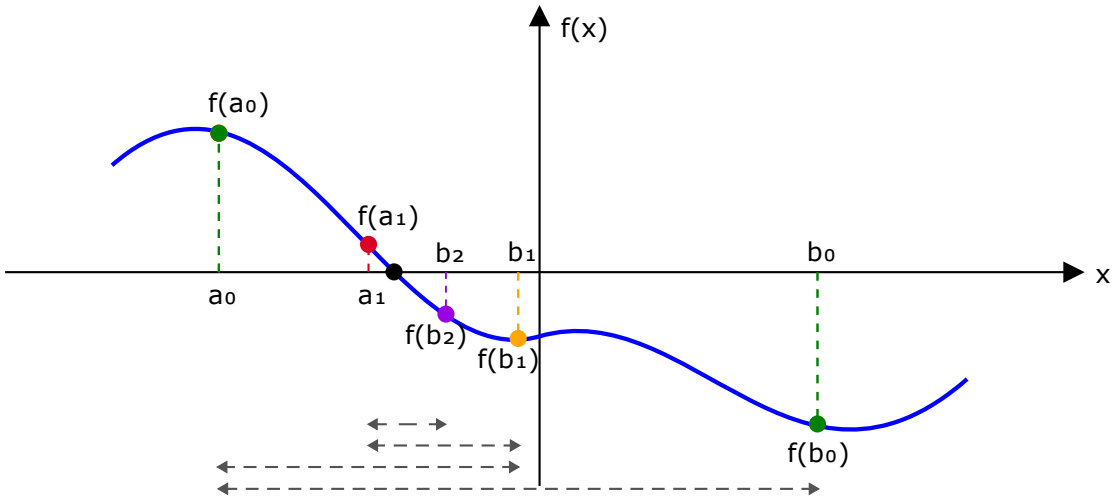

Figure 4.4: Scheme of the bisection method applied to a function $f(x)$: starting from $[a_0, b_0]$, the interval iteratively narrows towards zero of the function

guaranteeing highly accurate results. In this discussion we will focus on analysing the left edge case of a contact, describing in detail its operation and peculiar characteristics; the right apex case, being specular, will follow similar dynamics and can be easily understood from the considerations already made. In the numerical implementation phase, the method is initialised by evaluating, for each contact edge $\tilde{X}_i$, the error associated with the initial contact approximation, determined by the solution obtained at the previous penetration. If this error, represented by the pressure at the edge, is greater than the tolerated threshold, action is taken on the edge: if the pressure is negative, the edge is shifted by $\delta\tilde{X}$ to the right; if it is positive, the edge is shifted by $\delta\tilde{X}$ to the left (Fig.4.5). If in the course of these changes the sign of the error reverses, this indicates that the null pressure point has been exceeded, and we proceed to halve $\delta\tilde{X}$ until a concordance of sign is re-established. The process stops at that edge when the error is sufficiently small. This iterative scheme continues until the value of the displacement on the individual contacts between two successive iterations is less than an established threshold.

4.5.5 Finite difference method

In order to obtain an accurate and efficient solution of the system under consideration, it is essential to evaluate the derivatives of the functions involved with sufficient accuracy, as these represent essential quantities for the description of the local behaviour of the variables and, consequently, for the correct formulation of the mathematical model and its numerical resolution. From an implementation point of view, the derivatives are not computed analytically, but approximated numerically by means of the finite difference method, a technique based on the fundamental definition of derivative and the concept of Taylor series expansion. The basic idea is to replace the continuous derivative with a discrete expression

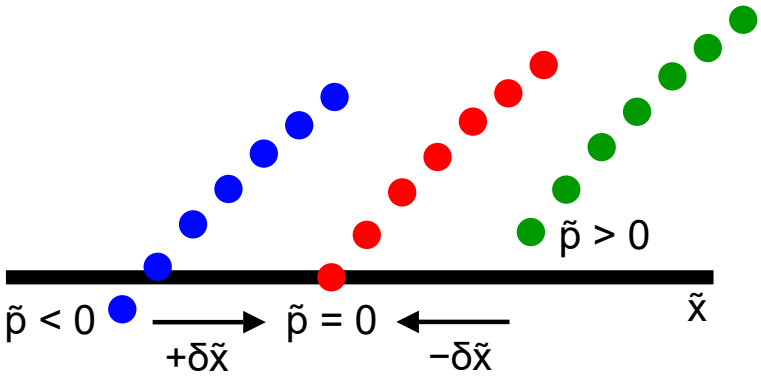

Figure 4.5: Display of pressure profiles relative to the left edge of a contact for the possible cases obtained during the application of the bisection method. During the iterative procedure, the profiles with $\tilde{p} > 0$ and $\tilde{p} < 0$ preceding convergence to the limiting case $\tilde{p} = 0$ are observed. For the right edge case, the corresponding image is obtained by a specular reflection with respect to the vertical axis

that evaluates the function in a neighbourhood of the point of interest. The theoretical principle can be expressed in its simplest form as:

$$\frac{\partial u(x)}{\partial x} = \lim_{\Delta x \to 0} \frac{u(x+\Delta x) - u(x)}{\Delta x} \approx \frac{u(x+\Delta x) - u(x)}{\Delta x} \tag{4.46}$$

where the term on the right-hand side represents an approximation of the derivative, valid in the case where Δx is sufficiently small but still finite. To analyse the quality of this approximation, we use the Taylor series development of the function $u(x + \Delta x)$ around x, which gives:

$$u(x+\Delta x) = u(x) + \Delta x \frac{\partial u}{\partial x} + \frac{\Delta x^2}{2}\frac{\partial^2 u}{\partial x^2} + \frac{\Delta x^3}{6}\frac{\partial^3 u}{\partial x^3} + \dots \tag{4.47}$$

Taking $u(x)$ to the first member and dividing by Δx, we obtain:

$$\frac{u(x+\Delta x) - u(x)}{\Delta x} = \frac{\partial u}{\partial x} + \frac{\Delta x}{2}\frac{\partial^2 u}{\partial x^2} + \frac{\Delta x^2}{6}\frac{\partial^3 u}{\partial x^3} + \dots = \frac{\partial u}{\partial x} + \mathcal{O}(\Delta x) \tag{4.48}$$

Discretization schemes are commonly classified according to their order of accuracy p, which indicates how quickly the error tends to zero as Δx decreases, and is expressed with the notation $\mathcal{O}(\Delta x^p)$. The one described above is a forward scheme, which provides an approximation of the first derivative with a truncation error of the order of $\mathcal{O}(\Delta x)$. In addition to the latter, there are other discretization schemes, such as the backward scheme, which uses values of the function at earlier points than the point of interest, and has the same order of accuracy as the forward scheme. It is also possible to construct higher-order schemes, such as the centred scheme, that reduce the approximation error by exploiting a larger number of points around the considered position, which leads to an increase in the number of evaluations required for the function and, consequently, a higher computational cost.

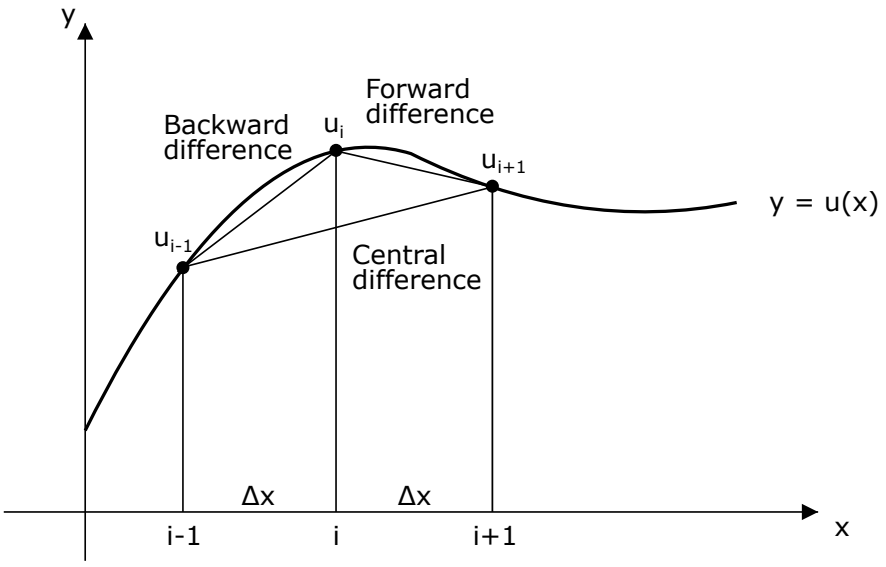

Figure 4.6: Comparison of the main finite difference schemes for the first derivative: backward, forward and central

In the framework of the problem under consideration, the first derivative of the system's energy with respect to a $\tilde{X}_i$ coordinate of the contact edge can be approximated by several finite difference schemes. A first-order forward scheme is expressed by:

$$\frac{\partial \tilde{U}}{\partial \tilde{X}_i} \approx \frac{1}{\Delta \tilde{X}} \left[\tilde{U}(\tilde{X}_1, \ldots, \tilde{X}_i + \Delta \tilde{X}, \ldots) - \tilde{U}(\tilde{X}_1, \ldots, \tilde{X}_i, \ldots) \right] + \mathcal{O}(\Delta \tilde{X}) \tag{4.49}$$

while a second-order centered scheme takes the form:

$$\frac{\partial \tilde{U}}{\partial \tilde{X}_i} \approx \frac{1}{2\Delta \tilde{X}} \left[\tilde{U}(\tilde{X}_1, \ldots, \tilde{X}_i + \Delta \tilde{X}, \ldots) - \tilde{U}(\tilde{X}_1, \ldots, \tilde{X}_i - \Delta \tilde{X}, \ldots) \right] + \mathcal{O}(\Delta \tilde{X}^2) \tag{4.50}$$

Similar considerations also apply to the second derivative, for which it is possible to derive finite difference schemes by means of appropriate theoretical developments, obtaining numerical approximations with different degrees of accuracy depending on the number of points and the order of the development used.

4.6 Results

In this section, we present the main results for a viscoelastic rough sliding contact in the presence of interfacial adhesion. Calculations are performed on a linear viscoelastic material with $E_0 = 10$ MPa, $\beta = 10$ and Poisson's ratio $\nu = 0.5$ (incompressible material). The interfacial work of adhesion is $\gamma = 0.01$ J/m^2 in agreement with most of existing measurements on polymers [112] and natural rubbers [105], which corresponds to a dimensionless value of $\tilde{\gamma} = 2.387 \times 10^{-7}$.
The rigid rough profile has a fundamental wavelength $\lambda_0 = 6.28$ mm and a self-affine roughness with no roll-off (see Appendix A in [100] for the numerical technique for profile generation). Since surfaces asperities may become unstable for

the Hurst roughness exponent $H < 0.7$ [113], we set $H = 0.8$ (corresponding to a 1D fractal dimension $D_{f,1D} = 2 - H = 1.2$) and a root mean square roughness $r_{\text{rms}} = \sqrt{\langle r^2 \rangle} = 10\,\mu$m, in agreement with most of existing experimental and numerical cases [109, 113, 114]. The profile Power Spectral Density (PSD):

$$C(q) = \frac{1}{2\pi} \int \langle r(0) r(x) \rangle e^{-iqx} dx \tag{4.51}$$

is given by:

$$\begin{aligned} C(q) &= C_0 \left(\frac{|q|}{q_0} \right)^{-(2H+1)} && q \in [q_0, q_1] \\ C(q) &= 0 && q > q_1 \end{aligned} \tag{4.52}$$

with $N_q = 50$ roughness scales and, consequently, $q_1 = N_q q_0$ and:

$$C_0 = \frac{r_{rms}^2}{q_0} \left(1 - \frac{1}{N_q^{2H}} \right)^{-1} \approx 10^{-13} \tag{4.53}$$

The average square slope is:

$$m_2 = \langle [r'(x)]^2 \rangle = \int q^2 C(q) dq \approx 0.0012 \tag{4.54}$$

Moreover, in order to make the results statistically meaningful, all output quantities are averaged over calculations with 20 different profile realizations.
The validity of the assumption of infinitely short-range adhesive interactions can be assessed using the Tabor parameter μ_T introduced in Section 1.5. For fractal surfaces with Hurst exponent $H > 0.5$, it is well known that the elastic energy is mainly associated with the largest wavelengths of the roughness [104, 107]. The same wavelengths also control the root-mean-square height r_{rms} [115]. Based on these considerations, the radius of curvature R can be estimated by considering an equivalent sinusoidal profile with amplitude r_{rms} and wavelength λ_0. This leads to:

$$R \approx \frac{\lambda_0^2}{4\pi^2 r_{\text{rms}}} \tag{4.55}$$

In our case, this expression yields $R \approx 0.1\,$m.
Assuming an equilibrium distance $Z_0 \approx 1\,$nm (typical for rubber-like materials), we obtain a Tabor coefficient $\mu_T \approx 460 \gg 3$. Therefore, short-range adhesion can safely be assumed in this regime. More generally, since Z_0 is in the nanometer range and the aspect ratio of asperities is typically much smaller than 1, short-range adhesion always occurs in rubberlike materials. Their relatively low stiffness leads to large values of the adhesion length l, confirming the dominance of this regime.
Finally, regarding the numerical procedure, after performing a suitable sensitivity analysis, the Broyden method was adopted for the solution of the adhesive rough case, with the derivatives evaluated using a first-order finite-difference scheme.

4.6.1 Adhesive behavior

Previous studies on adhesive viscoelastic contacts in steady-state sliding focused only on simpler sinusoidal geometry (i.e., one wavelength) [24, 25]. However, even in purely elastic contacts, the overall adhesive response of the interface is significantly affected by roughness, which usually increases the elastic strain energy stored in the solid (especially at large scales) and may almost mask adhesion [61, 104–107]. The expected scenario in viscoelastic solids is much more complex, as the governing condition given by Eq. (4.11) also includes a non-conservative term.

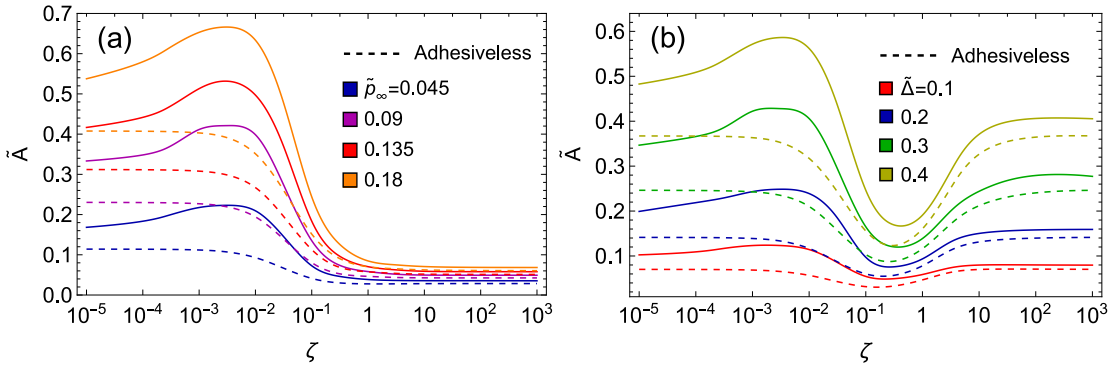

Figure 4.7: The dimensionless contact area $\tilde{A}$ as function of the dimensionless sliding velocity ζ, for different values of (a) the dimensionless remote pressure $\tilde{p}_\infty$ and (b) the dimensionless penetration $\tilde{\Delta}$

For these reasons, we investigate rough viscoelastic adhesion by reporting in Figure 4.7 the contact area $\tilde{A}$ as a function of the dimensionless sliding velocity $\tilde{\zeta}$, at either given contact mean pressure p_∞ (Fig. 4.7a) and penetration Δ (Fig. 4.7b). For comparison, we also include the adhesiveless results (dashed lines). Focusing on the first case, i.e. load controlled conditions, Fig. 4.7a shows a significant difference between adhesiveless and adhesive conditions. More importantly, this difference depends on the dimensionless sliding velocity ζ; indeed, as a general qualitative rule, increasing ζ, the frequency of excitation of the material increases, and the resulting viscoelastic response is stiffer. This can be clearly observed by comparing adhesive and adhesiveless contact area predictions at very low ($\zeta < 10^{-5}$) and very high ($\zeta > 10^3$) dimensionless sliding velocity. In these regions, no dissipation occurs and the viscoelastic material behaves almost elastically, with moduli approximately equal to E_0 (rubbery) and E_∞ (glassy), respectively. Consequently, regardless of the specific value of p_∞, interfacial adhesion entails a larger contact area increase compared to the adhesiveless conditions in the former case (i.e., very low ζ). However, while in adhesiveless contacts a monotonic transition is observed between the two regions, in the presence of adhesion the contact area trend is non-monotonic with ζ, resembling the behavior reported in [24, 25] for a single wavelength profile.
Qualitative arguments can be used to roughly explain this interesting difference. In adhesiveless conditions, only one dimensional scale governs the viscoelastic contact

behavior, which is (say, proportional to) the size of the contact spots; increasing ζ results in a higher excitation frequency, so that stiffening occurs for each of the contact spot. The precise local effect depends on the specific size of the contact spot entailing a broader range of ζ for the complete transition from rubbery to glassy elastic-like regimes compared to wavy contacts. Conversely, in the presence of adhesion, viscoelastic effects can be qualitatively divided in large-scale, roughly governed by the contact spots size as in the adhesiveless case, and small-scale, related a dimension associated with the adhesive necks (e.g., the local radius of curvature or the height) at the contact trailing edges. A slight increase of the sliding velocity to $\zeta \approx 10^{-3} - 10^{-2}$ (i.e., right above the rubbery region) leads to a different behavior of the two viscoelastic scales governing the adhesive contact; indeed, on one hand, the bulk of the material still behaves in the soft elastic regime and, on the other hand, viscoelastic losses occur close to each contact edge where the material is cyclically deformed close to the critical frequency $\omega_c \approx 1/\tau$, where the viscoelastic dissipation is maximum. As a consequence, focusing on the trailing edge, according to Eqs. (4.9,4.10), besides the change of the elastic energy δU an additional non-conservative term δL_P appears. Under these conditions, Eq. 4.9 can be locally rewritten as:

$$\frac{\delta U}{\delta X} = \Delta\gamma - \frac{\delta L_P}{\delta X} = \Delta\gamma_{eff} \tag{4.56}$$

eventually resulting in enhanced adhesive effects ($\Delta\gamma_{eff} > \Delta\gamma$) and increased contact area (see Fig. 4.7a). This behavior is in qualitative agreement with experimental results reported by Krick et al. on rough adhesive viscoelastic contacts, showing a contact area increase from static (i.e., $\zeta \to 0$) to slow sliding conditions [108]. Finally, a further increase of the dimensionless sliding velocity ζ leads to stiff elastic response at both scales, therefore contact area reduction occurs.
Similar conclusions can be drawn in the displacement controlled case, as shown in Figure 4.7b. In adhesiveless conditions, since the indenter penetration is fixed, once elastic-like conditions are achieved, the contact area is uniquely prescribed, regardless of the elastic modulus. This happens for both $\zeta \to 0$ and $\zeta \to \infty$. At intermediate velocity, as reported in several studies [25, 54, 93], the trailing edge shrinkage due to hysteretic viscoelastic behavior leads to a reduction of $\tilde{A}$. In this case, also, interfacial adhesion is a game changer; in fact, in the same range of $\zeta \approx 10^{-3} - 10^{-2}$, the enhanced adhesive effects localized at the trailing edges of the contact spots enlarge the overall contact size. However, once large-scale viscoelastic effects become dominant, i.e. for $\zeta \approx 10^{-1}$, the qualitative adhesiveless trend is recovered. Notably, in adhesive conditions, the very low and very high velocity response is not the same, as the contact area is no longer uniquely defined. Specifically, for $\zeta \to 0$ adhesion is much more effective, as the elastic-like response is softer.

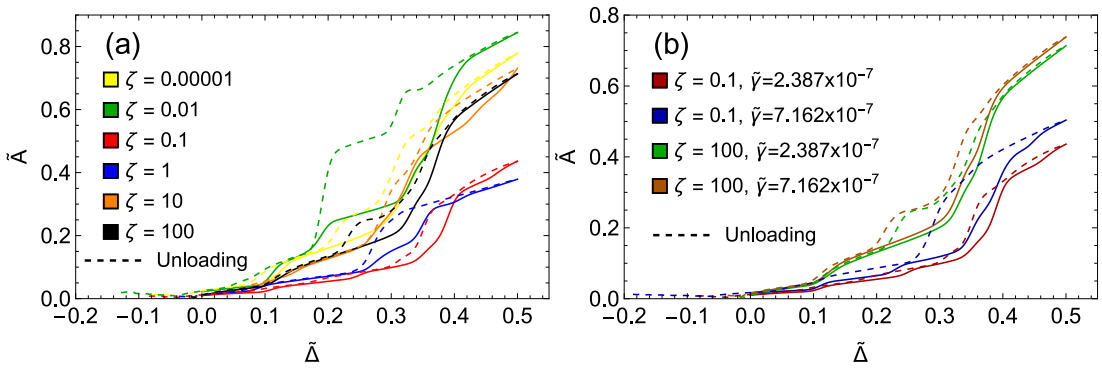

Figure 4.8: Quasi-static approach-retraction cycles. (a) Effect of sliding velocity on hysteresis cycles. (b) Effect of adhesion on hysteresis cycles. Results are presented for a single roughness realization

Furthermore, provided that the specific loading history can be neglected (i.e., quasi-static conditions), periodic sliding contacts involving single wavelength (i.e., wavy) profiles are characterized by unique equilibrium solution. On the contrary, in the presence of roughness, even in quasi-static approach-retraction cycles, the solution at equilibrium is path-dependent. Indeed, given the same value of $\tilde{\Delta}$, contact spots that are not yet in contact during loading, can be still in contact during unloading, due to the formation of adhesive necks. This mechanism may eventually lead to adhesive hysteresis, which is investigated in Figure 4.8 showing the dimensionless contact area $\tilde{A}$ as a function of the dimensionless contact penetration $\tilde{\Delta}$ in quasi-static approach-retraction cycles, for different values of the dimensionless sliding velocity ζ and adhesion energy $\tilde{\gamma}$. Regardless of the values of ζ and $\tilde{\gamma}$, we clearly observe that the loading path in the $\tilde{A}-\tilde{\Delta}$ diagram is different from the unloading one, with the latter occurring at globally higher contact area values. Importantly, in Fig. 4.8a the largest hysteresis correspond to $\zeta \approx 10^{-2}$; since calculations are performed in displacement controlled conditions, this is consistent with the results of Fig. 4.7b and, more specifically, with the value of ζ where the highest effective adhesion occurs due to small-scale viscoelastic effects (close to the contacts trailing edges) eventually leading to the maximum value of the contact area $\tilde{A}$. Indeed, 4.8b shows that the hysteresis increases with the adhesion value, in agreement with previous finding for elastic rough contacts [116]. Quasi-static unloading analysis also allows to calculate the contact toughness T, i.e. the external work required to achieve complete (quasi-static) detachment of the rigid profile from the viscoelastic material during sliding. In dimensionless quantities, this is given by:

$$\tilde{T} = \frac{2(1-\nu^2)T}{\Lambda^2 E_0} = 2\pi \int_{\tilde{\Delta}_0}^{\tilde{\Delta}_{\text{out}}} \tilde{p}_\infty(\tilde{\Delta}) d\tilde{\Delta} \tag{4.57}$$

where $\tilde{\Delta}_{\text{out}}$ is the dimensionless penetration at complete detachment (pull-off) and $\tilde{\Delta}_0$ is the dimensionless penetration corresponding to $\tilde{p}_\infty = 0$. Notably, both of them depend on the dimensionless sliding velocity ζ.

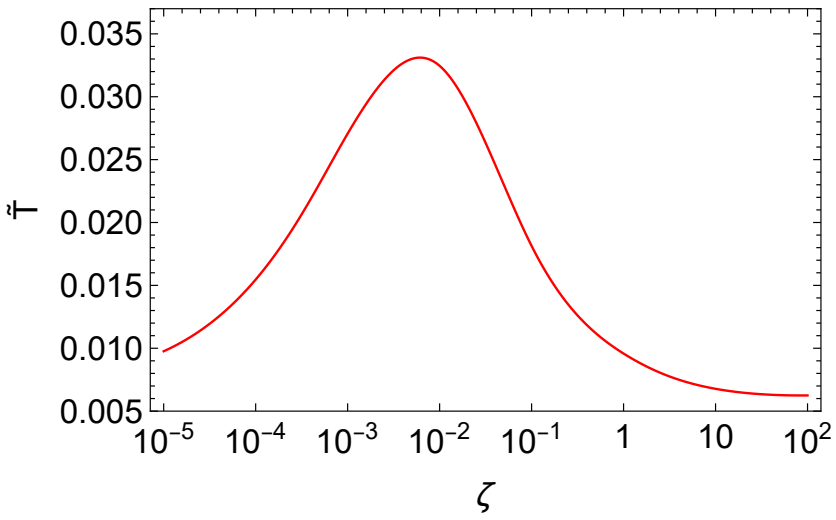

Figure 4.9: The dimensionless contact toughness $\tilde{T}$ in quasi-static unloading as a function of the dimensionless sliding velocity ζ

In agreement with previous experimental and numerical results [25,78], Figure 4.9 shows that the maximum toughness is reported in the range of velocities where the small-scale viscoelasticity enhances the effective adhesion, i.e. for $\zeta \approx 10^{-3} - 10^{-2}$. In contrast, at very large sliding velocity, we have $T \to 0$, as in the glassy region the stiff elastic-like response almost completely masks adhesion.

4.6.2 Friction

When a rough profile slides past a viscoelastic half-plane, this undergoes cyclic deformations which induce energy dissipation [64, 105]. This has been shown to lead to asymmetric contact pressure distribution across each asperity in contact and, in turn, to the so-called viscoelastic friction force opposing the relative motion [56, 93, 100, 102]. The corresponding viscoelastic friction coefficient μ is given by Eq. (4.16). In this section, we focus on the interplay between adhesion, viscoelasticity, and roughness on the overall contact frictional response. Indeed, while in the adhesiveless case only the bulk of the material contributes to the viscoelastic energy dissipation due to the cyclic compression induced by the sliding indenter, in adhesive conditions also the tensile stresses at the edge of each contact spot affect the overall energy dissipation and, ultimately, the resulting friction.
More in detail, to highlight the role of multi-scale roughness, we compare our results with the case of a single wavelength (sinusoid) indenter. Previous studies show that adhesion is governed by the ratio between the adhesive and elastic potential energy [25, 55, 86], i.e. by the dimensionless parameter $\tilde{\Gamma} = \tilde{\gamma}/\tilde{\Lambda}^2$. Furthermore, since the friction coefficient in wavy (full-)contacts is $\mu \propto \sqrt{m_2}$ [56, 64], a scientifically meaningful comparison should be sought only at given $\tilde{\Gamma}$ and m_2.

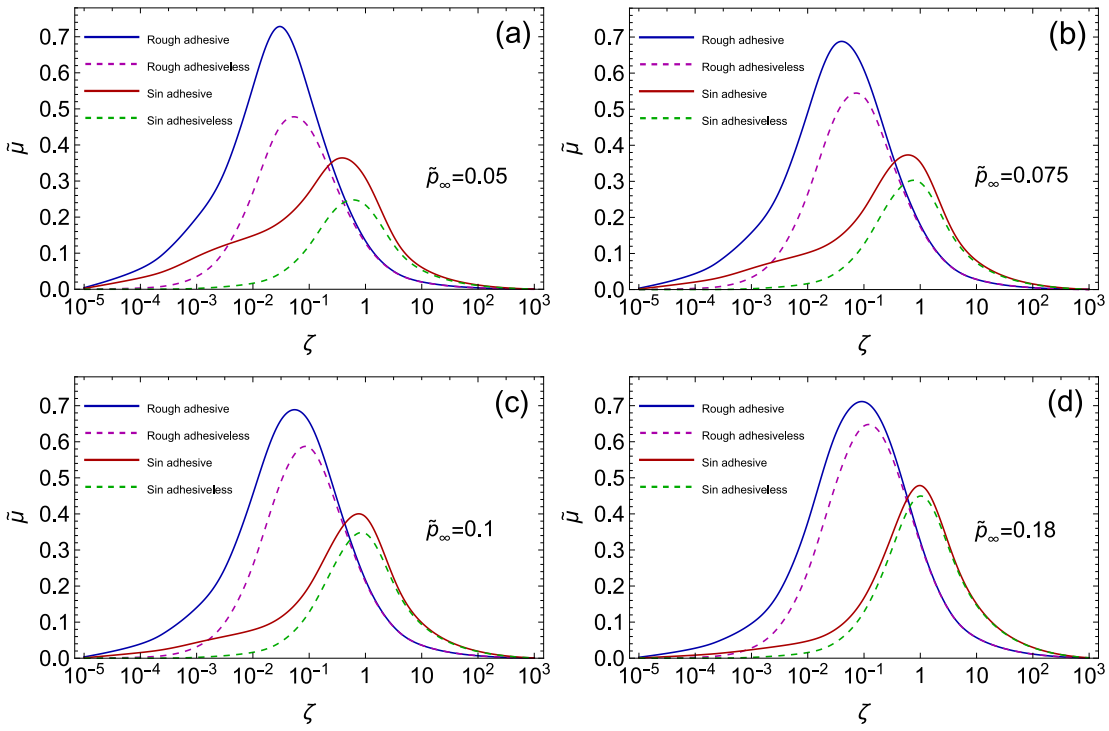

Figure 4.10: The reduced friction coefficient $\tilde{\mu}$ as function of the dimensionless sliding velocity ζ, for different values of the dimensionless remote pressure $\tilde{p}_\infty$. Adhesive (solid) and adhesiveless (dashed) results are shown both for rough and wavy contacts conditions

Recalling that for a sinusoidal profile of wavelength λ_0 and amplitude Λ we have:

$$m_2 = 2\left(\frac{\pi\Lambda}{\lambda_0}\right)^2 \tag{4.58}$$

one can easily find that, under the same dimensional parameters, an appropriate comparison entails $\lambda_0 \approx 1$ mm and $\Lambda \approx 8\,\mu$m for the sinusoid. Since changing the Hurst roughness exponent H only leads to a slight shift of the μ vs. ζ curves [117], aiming at generalizing the frictional results on the basis on the aforementioned arguments, we define the reduced friction coefficient as:

$$\tilde{\mu} = \frac{\mu}{\sqrt{m_2}} \tag{4.59}$$

Figure 4.10 shows the reduced friction coefficient $\tilde{\mu}$ as a function of the dimensionless sliding velocity ζ for different values of dimensionless remote pressure $\tilde{p}_\infty$. A comparison is presented between adhesive and adhesiveless conditions, as well as for rough and sinusoidal contacts.

Firstly, we focus on the rough case; in fact, results suggest that, in the presence of adhesion, small-scale effects localized close to the contact edges enhance viscoelastic dissipation compared to adhesiveless conditions, resulting in significantly higher values of $\tilde{\mu}$, regardless of the applied pressure. As previously discussed, small-scale adhesive-governed effects occur mainly in the range of relatively low

sliding velocity $\zeta \lessapprox 10^{-2}$, where the bulk of the material behaves almost elastically (vanishing friction in the adhesiveless case); in these conditions, the leading and trailing edges present a different local loading history, namely non-contact to contact (unloaded to loaded) in the former case and the opposite in the latter one. This entails a different non-conservative viscoelastic response (see Eq. (4.11)) and, in turn, a different adhesive behavior (see [24,25] for further details) which results in the so-called viscoelastic-induced adhesive hysteresis. As the leading and tailing edges behave differently, a net force is developed (i.e., the adhesive friction), which increases the value of $\tilde{\mu}$. However, as observed in Figure 4.7, at intermediate values of $\zeta \approx 10^{-2} - 10^{-1}$ adhesion also entails a significant increase of the contact area and, in turn, of the material involved in cyclic deformations. Since the bulk response is viscoelastic in this range of ζ, large-scale energy dissipation increases, and the peak friction is significantly higher in adhesive conditions compared to adhesiveless ones. This confirms that scale separation in viscoelastic adhesion can only provide qualitative hints, and accurate predictions require taking into account the interactions between small- and large-scale effects [24, 25]. At relatively high values of $\zeta \gtrapprox 10^{-1}$, the material close to the contact edges behaves elastically (with modulus E_∞); viscoelastic dissipation occurs mainly in the bulk of the material (large-scale), thus adhesive and adhesiveless friction predictions overlap. Of course, increasing the normal pressure leads to higher values of the contact area; hence, large-scale (bulk) effects become dominant regardless of ζ, and the role of small-scale viscoelastic-induced adhesive hysteresis reduces with $\tilde{p}_\infty$ increasing.
The comparison between sinusoidal and rough sliding contacts highlights, in the latter case, a shift towards lower values of dimensionless sliding velocity ζ corresponding to the peak friction. This can be qualitatively discussed recalling that $\omega_c \approx 1/\tau$ is the critical excitation frequency associated with the highest viscoelastic dissipation; therefore, dimensional arguments show that, given a generic wavelength λ of the normal displacements, the bulk of the material is cyclically deformed at a frequency ω_c for a dimensionless sliding velocity $\zeta \approx \lambda/\lambda_0$. In the case of sinusoidal indenters, only one wavelength λ_0 is present, and the peak friction (maximum viscoelastic dissipation) occurs at $\zeta \approx 1$, in agreement with [56]. Conversely, rough profiles are multiscale, with the generic wavelength $\lambda < \lambda_0$ inducing high viscoelastic dissipation at $\zeta \approx \lambda/\lambda_0 < 1$. As a consequence, since viscoelastic friction depends on global viscoelastic energy dissipation, rough sliding contacts present the friction peak at $\zeta < 1$, with ζ decreasing as the number of scales N_q increases. Furthermore, we also observe that in the sinusoidal case the friction coefficient curve presents a more marked knee point associated with viscoelastic-induced adhesive hysteresis compared to the rough case.
Nonetheless, the most interesting feature emerging from the comparison against single-wavelength contact conditions is that the overall scenario is qualitatively similar, and the effect of roughness is far from hindering the interaction between viscoelasticity and adhesion. Indeed, rough viscoelastic contacts present a non-negligible increase in friction due to adhesion, in qualitative agreement with the long-standing experimental results by Grosch [23] and, more recently, by Maksuta et al. [118]. Since real surfaces always present a certain roughness, this result

might be fundamental for several applications, such as polymeric grippers and seals. Among others, for example, tire-road friction could be strongly affected by adhesion, especially in race application where the road surface is relatively clean and tire rubber is 'soft' (i.e., the adhesion parameter Γ is larger than for car tires). In the latter case, according to roughness and rubber data provided in Refs. [115,119], we have $\lambda_0 \approx 5$ mm, $r_{\mathrm{rms}} \approx 0.2$ mm, and $E_0 \approx 10$ MPa, therefore, the mean tire-road contact pressure $p_\infty \approx 1$ bar corresponds to a dimensionless value of $\tilde{p}_\infty \approx 0.6$, as for Figure 4.10a,b.

Conclusions

In this thesis, we investigate the adhesive contact mechanics in the presence of relative sliding motion between a rough rigid indenter and a viscoelastic solid. A central part of this work has been the extension to the multiscale roughness scenario of the energy balance formulation, which was originally proposed in [24, 25] as a generalization of Griffith's criterion for viscoelastic adhesion in the single-scale roughness case. In this framework, the equilibrium condition of the system is expressed by requiring that the solution simultaneously satisfies the closure conditions at the apex of all contact spots. To this end, a dedicated numerical procedure was employed to handle adhesive multiscale contacts, in which the contact configuration may dynamically evolve during the iterative solution process; in addition, a study of multidimensional numerical solution methods was carried out, aimed at optimizing the efficiency and robustness of the procedure.
The results show a fundamental interaction between roughness, viscoelasticity and adhesion. Specifically, in addition to bulk large-scale viscoelastic effects, adhesive necks at the edge of each contact spot trigger additional viscoelastic dissipation. Since the dimensional scales are different, these phenomena occur at different sliding velocities, which partially overlap. As a result, at low-intermediate velocity, very effective adhesion is enhanced by non-conservative small-scale viscoelastic effects, and the contact area strongly increases compared to adhesiveless conditions. Moreover, since the leading and trailing edges experience different loading histories during sliding, their viscoelastic response is different, and viscoelastic-induced adhesive hysteresis may occur across each contact spot, which eventually results in an additional (but non-additive) contribution to friction compared to the adhesiveless case. Though additional roughness scales may hinder adhesive effects in elastic contacts, here we show that the same is likely not to happen in viscoelastic sliding contacts, which present a rough tribological behavior (contact area and friction) qualitatively similar to the sinusoidal single-wavelength case, as indeed highlighted in some remarkable existing experiments.
Overall, the findings of this thesis underscore the pivotal importance of the complex interaction between adhesion, surface roughness and viscoelasticity. Roughness should not be regarded merely as a secondary effect, since under specific conditions it can become a fundamental mechanism in determining the system response in the presence of adhesion. The present work clarifies these mechanisms, thereby deepening the comprehension of adhesive sliding contact in viscoelastic materials.
The modelling framework developed in this thesis opens several possibilities for fu-

ture research. A first, natural extension concerns the generalisation of the present 1D+1D formulation to fully three-dimensional rough surfaces. Our research group has already developed a BEM-based numerical model capable of handling 3D rough elastic contacts in the presence of adhesion [120]. Building upon this foundation, future work will focus on integrating the viscoelastic constitutive behaviour analysed in this thesis into the existing 3D code, thereby enabling simulations of realistic multiscale viscoelastic rough interfaces. A second research direction involves extending the material description to rheologies characterised by multiple relaxation times. Such generalised viscoelastic models, e.g. of the Prony-series type, would allow the framework to capture a broader range of time-dependent mechanical responses relevant for polymeric or biological substrates. Finally, the methodology can be further enhanced by incorporating potential material inhomogeneity, such as depth-dependent variations of viscoelastic properties through the substrate thickness. Accounting for spatially varying rheological parameters would enable the accurate analysis of graded materials and engineered surface layers. Another promising direction concerns the generalisation of the adhesive description. In this thesis, adhesion has been treated in the limit of infinitely short-range interactions, which is appropriate for JKR-like conditions and enables a formulation based purely on the work of adhesion $\Delta\gamma$. However, in some engineering systems the cohesive zone has a finite spatial extent, and adhesion is better represented through finite-range traction–separation laws (e.g., Maugis–Dugdale or Lennard–Jones based interactions). Extending the present energy-balance framework to include finite-range adhesive potentials makes it possible to capture additional physical effects, such as the transition between DMT- and JKR-like regimes, thereby enabling a unified description of adhesive contact across different values of the Tabor parameter and improving the predictive accuracy of viscoelastic rough contact simulations.

References

[1] R. S. Sharp, P. Gruber, E. Fina, Circuit racing, track texture, temperature and rubber friction, Vehicle System Dynamics 54 (2016) 510–525.

[2] T. V. Tolpekina, B. N. J. Persson, Adhesion and friction for three tire tread compounds, Lubricants 7 (2019) 20.

[3] N. Miyashita, B. N. J. Persson, Role of strain softening and viscoelastic memory for the rolling friction of two tire tread compounds, The Journal of Chemical Physics 161 (Aug. 2024).

[4] J. G. Quini, G. Marinucci, Polyurethane structural adhesives applied in automotive composite joints, Materials Research 15 (2012) 434–439.

[5] A. Luo, S. S. Pande, K. T. Turner, Versatile adhesion-based gripping via an unstructured variable stiffness membrane, Soft Robotics 9 (2022) 1177–1185.

[6] C. Son, S. Jeong, S. Lee, P. M. Ferreira, S. Kim, Tunable adhesion of shape memory polymer dry adhesive soft robotic gripper via stiffness control, Robotics 12 (2023) 59.

[7] H. Min, D. Bae, S. Jang, S. Lee, M. Park, C. B. Dayan, J. Choi, K. Bak, Y. Yang, S. Chun, M. Sitti, Stiffness-tunable velvet worm–inspired soft adhesive robot, Science Advances 10 (Nov. 2024).

[8] J. Y. Chung, M. K. Chaudhury, Roles of discontinuities in bio-inspired adhesive pads, Journal of The Royal Society Interface 2 (2005) 55–61.

[9] W. Tang, S.-r. Ge, H. Zhu, X.-c. Cao, N. Li, The influence of normal load and sliding speed on frictional properties of skin, Journal of Bionic Engineering 5 (2008) 33–38.

[10] M. Zhou, N. Pesika, H. Zeng, Y. Tian, J. Israelachvili, Recent advances in gecko adhesion and friction mechanisms and development of gecko-inspired dry adhesive surfaces, Friction 1 (2013) 114–129.

[11] N. Menga, L. Afferrante, N. Pugno, G. Carbone, The multiple v-shaped double peeling of elastic thin films from elastic soft substrates, Journal of the Mechanics and Physics of Solids 113 (2018) 56–64.

[12] N. Menga, D. Dini, G. Carbone, Tuning the periodic v-peeling behavior of elastic tapes applied to thin compliant substrates, International Journal of Mechanical Sciences 170 (2020) 105331.

[13] M. Ceglie, N. Menga, G. Carbone, The role of interfacial friction on the peeling of thin viscoelastic tapes, Journal of the Mechanics and Physics of Solids 159 (2022) 104706.

[14] C. Pang, J. Kim, Y. Wu, M. Y. Wang, H. Yu, M. Sitti, Bioinspired microstructured adhesives with facile and fast switchability for part manipulation in dry and wet conditions, Advanced Functional Materials 33 (May 2023).

[15] J.-N. Ding, Y.-G. Meng, S.-Z. Wen, Mechanical stability and sticking in a model microelectromechanical systems (mems) under casimir forces–part i: Corrections to the casimir force, International Journal of Nonlinear Sciences and Numerical Simulation 1 (Jan. 2000).

[16] B. Bhushan, Nanotribology and nanomechanics of mems/nems and biomems/bionems materials and devices, Microelectronic Engineering 84 (2007) 387–412.

[17] S. H. Kim, D. B. Asay, M. T. Dugger, Nanotribology and mems, Nano Today 2 (2007) 22–29.

[18] B. Taran, S. Amoozegar, R. Bayaz, F. Barazandeh, The theoretical investigation of the effect of adhesive layers used in microassembly on the dynamic response of a microaccelerometer, DTIP 2011 - Symposium on Design, Test, Integration and Packaging of MEMS/MOEMS (01 2011).

[19] X. Zeng, Y. Peng, M. Yu, H. Lang, X. Cao, K. Zou, Dynamic sliding enhancement on the friction and adhesion of graphene, graphene oxide, and fluorinated graphene, ACS Applied Materials and Interfaces 10 (2018) 8214–8224.

[20] S. Buchwalder, M. Hersberger, H. Rebl, S. Seemann, W. Kram, A. Hogg, L. G. W. Tvedt, I. Clausen, J. Burger, An evaluation of parylene thin films to prevent encrustation for a urinary bladder pressure mems sensor system, Polymers 15 (2023) 3559.

[21] E. Sancaktar, H. F. Brinson, The Viscoelastic Shear Behavior of a Structural Adhesive, Springer US, 1980, p. 279–299.

[22] J. L. Bitner, J. L. Rushford, W. S. Rose, D. L. Hunston, C. K. Riew, Viscoelastic fracture of structural adhesives, The Journal of Adhesion 13 (1981) 3–28.

[23] K. Grosch, The relation between the friction and visco-elastic properties of rubber, Proceedings of the Royal Society of London. Series A. Mathematical and Physical Sciences 274 (1963) 21–39.

[24] G. Carbone, C. Mandriota, N. Menga, Theory of viscoelastic adhesion and friction, Extreme Mechanics Letters 56 (2022) 101877.

[25] C. Mandriota, N. Menga, G. Carbone, Adhesive contact mechanics of viscoelastic materials, International Journal of Solids and Structures 290 (2024) 112685.

[26] C. Mandriota, N. Menga, G. Carbone, Enhancement of adhesion strength in viscoelastic unsteady contacts, Journal of the Mechanics and Physics of Solids 192 (2024) 105826.

[27] D. Maugis, Contact, adhesion and rupture of elastic solids, Vol. 130, Springer Science and Business Media, 2000.

[28] H. Hertz, On the contact of elastic solids, Journal für die reine und angewandte Mathematik 92 (1882) 156–171.

[29] P. Glick, S. A. Suresh, D. Ruffatto, M. Cutkosky, M. T. Tolley, A. Parness, A soft robotic gripper with gecko-inspired adhesive, IEEE Robotics and Automation Letters 3 (2018) 903–910.

[30] Y. Mengüç, S. Y. Yang, S. Kim, J. A. Rogers, M. Sitti, Gecko-inspired controllable adhesive structures applied to micromanipulation, Advanced Functional Materials 22 (2012) 1246–1254.

[31] C. Horie, H. Miyazaki, Atomic-force-microscopy images of graphite due to van der waals interactions, Physical Review B 42 (1990) 11757–11761.

[32] J. L. Hutter, J. Bechhoefer, Measurement and manipulation of van der waals forces in atomic-force microscopy, Journal of Vacuum Science and Technology B: Microelectronics and Nanometer Structures Processing, Measurement, and Phenomena 12 (1994) 2251–2253.

[33] K. M. Burson, M. Yamamoto, W. G. Cullen, Modeling noncontact atomic force microscopy resolution on corrugated surfaces, Beilstein Journal of Nanotechnology 3 (2012) 230–237.

[34] L. Afferrante, G. Violano, On the effective surface energy in viscoelastic hertzian contacts, Journal of the Mechanics and Physics of Solids 158 (2022) 104669.

[35] G. Violano, L. Afferrante, Size effects in adhesive contacts of viscoelastic media, European Journal of Mechanics - A/Solids 96 (2022) 104665.

[36] J. Luo, J. Liu, H. Xia, X. Ao, Z. Fu, J. Ni, H. Huang, Finite element analysis of adhesive contact behaviors in elastoplastic and viscoelastic media, Tribology Letters 72 (Dec. 2023).

[37] L. Afferrante, G. Violano, G. Carbone, Exploring the dynamics of viscoelastic adhesion in rough line contacts, Scientific Reports 13 (Sep. 2023).

[38] A. Maghami, Q. Wang, M. Tricarico, M. Ciavarella, Q. Li, A. Papangelo, Bulk and fracture process zone contribution to the rate-dependent adhesion amplification in viscoelastic broad-band materials, Journal of the Mechanics and Physics of Solids 193 (2024) 105844.

[39] A. Papangelo, R. Nazari, M. Ciavarella, Friction for a sliding adhesive viscoelastic cylinder: Effect of maugis parameter, European Journal of Mechanics - A/Solids 107 (2024) 105348.

[40] L. Jiang, M. Wu, Q. Yu, Y. Shan, Y. Zhang, Investigations on the adhesive contact behaviors between a viscoelastic stamp and a transferred element in microtransfer printing, Coatings 11 (2021) 1201.

[41] H. B. Callen, Thermodynamics: An Introduction to the Physical Theories of Equilibrium Thermostatics and Irreversible Thermodynamics, John Wiley and Sons, New York, 1960.

[42] R. C. D. Maugis, M. Barquins, Adhesion and fracture of elastic contacts, Métaux, Corrosion, Industrie (1976) 1–11.

[43] A. A. Griffith, Vi. the phenomena of rupture and flow in solids., Philosophical Transactions of the Royal Society of London. Series A, Containing Papers of a Mathematical or Physical Character 221 (1921) 163–198.

[44] K. Johnson, K. Kendall, R. AD, Surface energy and the contact of elastic solids, Proceedings of the Royal Society of London. A. Mathematical and Physical Sciences 324 (1971) 301–313.

[45] R. Bradley, Lxxix.the cohesive force between solid surfaces and the surface energy of solids, The London, Edinburgh, and Dublin Philosophical Magazine and Journal of Science 13 (1932) 853–862.

[46] B. Derjaguin, Untersuchungen uber die reibung und adhasion, iv: Theorie des anhaftens kleiner teilchen, Kolloid-Zeitschrift 69 (1934) 155–164.

[47] B. Derjaguin, V. Muller, Y. Toporov, Effect of contact deformations on the adhesion of particles, Journal of Colloid and Interface Science 53 (1975) 314–326.

[48] V. Muller, B. Derjaguin, Y. Toporov, On two methods of calculation of the force of sticking of an elastic sphere to a rigid plane, Colloids and Surfaces 7 (1983) 251–259.

[49] D. Tabor, Surface forces and surface interactions, Journal of Colloid and Interface Science 58 (1977) 2–13.

[50] V. Muller, V. Yushchenko, B. Derjaguin, On the influence of molecular forces on the deformation of an elastic sphere and its sticking to a rigid plane, Journal of Colloid and Interface Science 77 (1980) 91–101.

[51] D. Maugis, Adhesion of spheres: The jkr-dmt transition using a dugdale model, Journal of Colloid and Interface Science 150 (1992) 243–269.

[52] J. A. Greenwood, Adhesion of elastic spheres, Proceedings of the Royal Society of London. Series A: Mathematical, Physical and Engineering Sciences 453 (1997) 1277–1297.

[53] G. Carbone, B. Lorenz, B. N. J. Persson, A. Wohlers, Contact mechanics and rubber friction for randomly rough surfaces with anisotropic statistical properties, The European Physical Journal E 29 (2009) 275–284.

[54] G. Carbone, C. Putignano, A novel methodology to predict sliding and rolling friction of viscoelastic materials: Theory and experiments, Journal of the Mechanics and Physics of Solids 61 (2013) 1822–1834.

[55] G. Carbone, L. Mangialardi, Analysis of the adhesive contact of confined layers by using a green's function approach, Journal of the Mechanics and Physics of Solids 56 (2008) 684–706.

[56] N. Menga, L. Afferrante, G. Carbone, Effect of thickness and boundary conditions on the behavior of viscoelastic layers in sliding contact with wavy profiles, Journal of the Mechanics and Physics of Solids 95 (2016) 517–529.

[57] R. Christensen, Theory of Viscoelasticity, Courier Corporation, 2013.

[58] J. B. P. W. J. A. Greenwood, Contact of nominally flat surfaces, Proceedings of the Royal Society of London. Series A. Mathematical and Physical Sciences 295 (1966) 300–319.

[59] P. R. Nayak, Random process model of rough surfaces, Journal of Lubrication Technology 93 (1971) 398–407.

[60] J. Archard, Surface topography and tribology, Tribology 7 (1974) 213–220.

[61] K. Fuller, D. Tabor, The effect of surface roughness on the adhesion of elastic solids, Proceedings of the Royal Society of London. A. Mathematical and Physical Sciences 345 (1975) 327–342.

[62] J. Greenwood, A simplified elliptic model of rough surface contact, Wear 261 (2006) 191–200.

[63] A. Bush, R. Gibson, T. Thomas, The elastic contact of a rough surface, Wear 35 (1975) 87–111.

[64] B. N. Persson, Theory of rubber friction and contact mechanics, The Journal of Chemical Physics 115 (2001) 3840–3861.

[65] G. Carbone, F. Bottiglione, Asperity contact theories: Do they predict linearity between contact area and load?, Journal of the Mechanics and Physics of Solids 56 (2008) 2555–2572.

[66] G. Carbone, A slightly corrected greenwood and williamson model predicts asymptotic linearity between contact area and load, Journal of the Mechanics and Physics of Solids 57 (2009) 1093–1102.

[67] G. Carbone, M. Scaraggi, U. Tartaglino, Adhesive contact of rough surfaces: Comparison between numerical calculations and analytical theories, The European Physical Journal E 30 (Sep. 2009).

[68] L. Afferrante, G. Carbone, G. Demelio, Interacting and coalescing hertzian asperities: A new multiasperity contact model, Wear 278–279 (2012) 28–33.

[69] M. Ciavarella, V. Delfine, G. Demelio, A "re-vitalized" greenwood and williamson model of elastic contact between fractal surfaces, Journal of the Mechanics and Physics of Solids 54 (2006) 2569–2591.

[70] J.-P. Roberge, W. Ruotolo, V. Duchaine, M. Cutkosky, Improving industrial grippers with adhesion-controlled friction, IEEE Robotics and Automation Letters 3 (2018) 1041–1048.

[71] Q. Hu, E. Dong, D. Sun, Soft gripper design based on the integration of flat dry adhesive, soft actuator, and microspine, IEEE Transactions on Robotics 37 (2021) 1065–1080.

[72] H. Y. Yuen, H. P. Bei, X. Zhao, Underwater and wet adhesion strategies for hydrogels in biomedical applications, Chemical Engineering Journal 431 (2022) 133372.

[73] G. Bovone, O. Y. Dudaryeva, B. Marco-Dufort, M. W. Tibbitt, Engineering hydrogel adhesion for biomedical applications via chemical design of the junction, ACS Biomaterials Science and Engineering 7 (2021) 4048–4076.

[74] M. Ceglie, N. Menga, G. Carbone, Modelling the non-steady peeling of viscoelastic tapes, International Journal of Mechanical Sciences 267 (2024) 108982.

[75] X. Zhang, C. Luo, N. Menga, H. Zhang, Y. Li, S.-P. Zhu, Pressure and polymer selections for solid-state batteries investigated with high-throughput simulations, Cell Reports Physical Science 4 (2023) 101328.

[76] A. Cheng, L. Sun, N. Menga, W. Yang, X. Zhang, Interfacial performance evolution of ceramics-in-polymer composite electrolyte in solid-state lithium metal batteries, International Journal of Engineering Science 204 (2024) 104137.

[77] M. Barquins, D. Maugis, J. Blouet, R. Courtel, Contact area of a ball rolling on an adhesive viscoelastic material, Wear 51 (1978) 375–384.

[78] J.-C. Charmet, M. Barquins, Adhesive contact and rolling of a rigid cylinder under the pull of gravity on the underside of a smooth-surfaced sheet of rubber, International Journal of Adhesion and Adhesives 16 (1996) 249–254.

[79] A. Roberts, A. Thomas, The adhesion and friction of smooth rubber surfaces, Wear 33 (1975) 45–64.

[80] M. Ayyildiz, M. Scaraggi, O. Sirin, C. Basdogan, B. N. J. Persson, Contact mechanics between the human finger and a touchscreen under electroadhesion, Proceedings of the National Academy of Sciences 115 (2018) 12668–12673.

[81] K. N. G. Fuller, A. D. Roberts, Rubber rolling on rough surfaces, Journal of Physics D: Applied Physics 14 (1981) 221–239.

[82] K. Kendall, Rolling friction and adhesion between smooth solids, Wear 33 (1975) 351–358.

[83] B. K. Hoyer, R. Long, M. E. Rentschler, A tribometric device for the rolling contact of soft elastomers, Tribology Letters 70 (Mar. 2022).

[84] A. D. Roberts, Looking at rubber adhesion, Rubber Chemistry and Technology 52 (1979) 23–42.

[85] K. Johnson, The adhesion of two elastic bodies with slightly wavy surfaces, International Journal of Solids and Structures 32 (1995) 423–430.

[86] N. Menga, L. Afferrante, G. Carbone, Adhesive and adhesiveless contact mechanics of elastic layers on slightly wavy rigid substrates, International Journal of Solids and Structures 88 (2016) 101–109.

[87] N. Menga, C. Putignano, L. Afferrante, G. Carbone, The contact mechanics of coated elastic solids: Effect of coating thickness and stiffness, Tribology Letters 67 (Jan. 2019).

[88] M. H. Müser, Single-asperity contact mechanics with positive and negative work of adhesion: Influence of finite-range interactions and a continuum description for the squeeze-out of wetting fluids, Beilstein Journal of Nanotechnology 5 (2014) 419–437.

[89] M. H. Müser, B. N. J. Persson, Crack and pull-off dynamics of adhesive, viscoelastic solids, Europhysics Letters 137 (2022) 36004.

[90] Q. Wang, A. Papangelo, M. Ciavarella, H. Gao, Q. Li, Rapid detachment of a rigid sphere adhered to a viscoelastic substrate: An upper bound model incorporating maugis parameter and preload effects, Journal of the Mechanics and Physics of Solids 196 (2025) 106028.

[91] F. Pérez-Ràfols, J. S. Van Dokkum, L. Nicola, On the interplay between roughness and viscoelasticity in adhesive hysteresis, Journal of the Mechanics and Physics of Solids 170 (2023) 105079.

[92] S. C. Hunter, The rolling contact of a rigid cylinder with a viscoelastic half space, Journal of Applied Mechanics 28 (1961) 611–617.

[93] N. Menga, C. Putignano, G. Carbone, G. P. Demelio, The sliding contact of a rigid wavy surface with a viscoelastic half-space, Proceedings of the Royal Society A: Mathematical, Physical and Engineering Sciences 470 (2014) 20140392.

[94] M. Scaraggi, B. N. J. Persson, Friction and universal contact area law for randomly rough viscoelastic contacts, Journal of Physics: Condensed Matter 27 (2015) 105102.

[95] M. Scaraggi, B. N. J. Persson, General contact mechanics theory for randomly rough surfaces with application to rubber friction, The Journal of Chemical Physics 143 (Dec. 2015).

[96] C. Putignano, N. Menga, L. Afferrante, G. Carbone, Viscoelasticity induces anisotropy in contacts of rough solids, Journal of the Mechanics and Physics of Solids 129 (2019) 147–159.

[97] L. Afferrante, C. Putignano, N. Menga, G. Carbone, Friction in rough contacts of linear viscoelastic surfaces with anisotropic statistical properties, The European Physical Journal E 42 (Jun. 2019).

[98] M. Scaraggi, B. Persson, The effect of finite roughness size and bulk thickness on the prediction of rubber friction and contact mechanics, Proceedings of the Institution of Mechanical Engineers, Part C: Journal of Mechanical Engineering Science 230 (2016) 1398–1409.

[99] B. N. J. Persson, Contact mechanics for layered materials with randomly rough surfaces, Journal of Physics: Condensed Matter 24 (2012) 095008.

[100] N. Menga, L. Afferrante, G. Demelio, G. Carbone, Rough contact of sliding viscoelastic layers: numerical calculations and theoretical predictions, Tribology International 122 (2018) 67–75.

[101] N. Menga, Rough frictional contact of elastic thin layers: The effect of geometrical coupling, International Journal of Solids and Structures 164 (2019) 212–220.

[102] N. Menga, G. Carbone, D. Dini, Exploring the effect of geometric coupling on friction and energy dissipation in rough contacts of elastic and viscoelastic coatings, Journal of the Mechanics and Physics of Solids 148 (2021) 104273.

[103] C. Müller, M. H. Müser, G. Carbone, N. Menga, Significance of elastic coupling for stresses and leakage in frictional contacts, Physical Review Letters 131 (2023) 156201.

[104] B. Persson, E. Tosatti, The effect of surface roughness on the adhesion of elastic solids, The Journal of Chemical Physics 115 (2001) 5597–5610.

[105] B. N. J. Persson, O. Albohr, U. Tartaglino, A. I. Volokitin, E. Tosatti, On the nature of surface roughness with application to contact mechanics, sealing, rubber friction and adhesion, Journal of Physics: Condensed Matter 17 (2004) R1–R62.

[106] S. Medina, D. Dini, A numerical model for the deterministic analysis of adhesive rough contacts down to the nano-scale, International Journal of Solids and Structures 51 (2014) 2620–2632.

[107] B. N. J. Persson, M. Scaraggi, Theory of adhesion: Role of surface roughness, The Journal of Chemical Physics 141 (Sep. 2014).

[108] B. A. Krick, J. R. Vail, B. N. J. Persson, W. G. Sawyer, Optical in situ micro tribometer for analysis of real contact area for contact mechanics, adhesion, and sliding experiments, Tribology Letters 45 (2011) 185–194.

[109] G. Carbone, C. Putignano, Rough viscoelastic sliding contact: Theory and experiments, Physical Review E 89 (Mar. 2014).

[110] M. Santeramo, G. Carbone, G. Vorlaufer, S. Krenn, C. Putignano, Viscohydrodynamic lubrication in conformal contacts: A numerical approach, International Journal of Solids and Structures 311 (2025) 113236.

[111] C. G. Broyden, A class of methods for solving nonlinear simultaneous equations, Mathematics of Computation 19 (1965) 577–593.

[112] C. Frétigny, A. Chateauminois, Contact of a spherical probe with a stretched rubber substrate, Physical Review E 96 (Jul. 2017).

[113] B. N. J. Persson, On the fractal dimension of rough surfaces, Tribology Letters 54 (2014) 99–106.

[114] M. H. Müser, W. B. Dapp, R. Bugnicourt, P. Sainsot, N. Lesaffre, T. A. Lubrecht, B. N. J. Persson, K. Harris, A. Bennett, K. Schulze, S. Rohde, P. Ifju, W. G. Sawyer, T. Angelini, H. Ashtari Esfahani, M. Kadkhodaei, S. Akbarzadeh, J.-J. Wu, G. Vorlaufer, A. Vernes, S. Solhjoo, A. I. Vakis, R. L. Jackson, Y. Xu, J. Streator, A. Rostami, D. Dini, S. Medina, G. Carbone, F. Bottiglione, L. Afferrante, J. Monti, L. Pastewka, M. O. Robbins, J. A. Greenwood, Meeting the contact-mechanics challenge, Tribology Letters 65 (Aug. 2017).

[115] B. Lorenz, Y. R. Oh, S. K. Nam, S. H. Jeon, B. N. J. Persson, Rubber friction on road surfaces: Experiment and theory for low sliding speeds, The Journal of Chemical Physics 142 (May 2015).

[116] G. Carbone, E. Pierro, G. Recchia, Loading-unloading hysteresis loop of randomly rough adhesive contacts, Physical Review E 92 (Dec. 2015).

[117] Q. Li, M. Popov, A. Dimaki, A. E. Filippov, S. Kürschner, V. L. Popov, Friction between a viscoelastic body and a rigid surface with random self-affine roughness, Physical Review Letters 111 (Jul. 2013).

[118] D. Maksuta, S. Dalvi, A. Gujrati, L. Pastewka, T. D. B. Jacobs, A. Dhinojwala, Dependence of adhesive friction on surface roughness and elastic modulus, Soft Matter 18 (2022) 5843–5849.

[119] B. N. J. Persson, U. Tartaglino, O. Albohr, E. Tosatti, Rubber friction on wet and dry road surfaces: The sealing effect, Physical Review B 71 (Jan. 2005).

[120] M. Santeramo, G. Carbone, S. Krenn, C. Putignano, A novel energy-based numerical approach for adhesive contact mechanics of rough surfaces, Journal of the Mechanics and Physics of Solids 203 (2025) 106217.

Publications

Some contents of this thesis have been published in the following journal article, of which I am a co-author. In particular, the article presents the extension of the energy formulation to rough contact and includes part of the results concerning rough steady-state conditions, which are discussed in Chapter 4:

- Mastropasqua, M., Ronchi, A., Serra, A., Menga, N., & Carbone, G. (2026). Adhesion and friction in viscoelastic rough contacts. Tribology International, 213, 111000.
  https://doi.org/10.1016/j.triboint.2025.111000

Acknowledgements

The author gratefully acknowledges the financial and technical support of Pirelli Tyre S.p.A. within the framework of the National Recovery and Resilience Plan (PNRR) - NextGenerationEU for innovative industrial PhD projects.